ACCOUNTING FOR SOIL VARIABILITY IN NOVEL GPR APPLICATIONS OF ROOT PHENOTYPING AND SOIL ORGANIC CARBON QUANTIFICATION

A Thesis

by

CATHERINE ANN KOBYLINSKI

Submitted to the Office of Graduate and Professional Studies of
Texas A&M University
in partial fulfillment of the requirements for the degree of

MASTER OF SCIENCE

Chair of Committee,	Haly Neely
Committee Members,	Mark Everett
	Dirk Hays
	Katie Lewis
	Ben Wu
Head of Department,	David Baltensperger

August 2019

Major Subject: Soil Science

ABSTRACT

The ability to phenotype roots in situ would provide information for carbon sequestration potential through increased root mass, possible water-seeking strategies by plants, and data generation for plant breeders. However, current phenotyping techniques are often labor intensive and destructive to the observed plant. One potential phenotyping technique that is both rapid and nondestructive is ground penetrating radar (GPR). This technology has been proposed due to its ability to detect fine-scale differences in dielectric permittivity, which is strongly influenced by soil moisture content. To detect small differences in soil moisture caused by root growth, we will need to account for the soil signature in the GPR signal. The objective of this study was to test the feasibility of GPR data to be linked with soil electromagnetic data as a means to detect and visualize a rooting system in different soil textural classes. Additionally, GPR's potential as a device for quantifying soil organic carbon (SOC) was explored. Similar to current root phenotyping techniques, the agricultural field lacks a tool that can rapidly and non-destructively measure SOC in the field. Like root phenotyping, GPR may be a potential solution due to its ability to detect small scale changes in soil moisture in response to changes in SOC. The root phenotyping portion of this study focused on multiple field locations across Texas and one controlled experiment to simulate in situ and ideal conditions. GPR measurements were taken within each plot, along with multiple measurements of soil moisture to account for soil variability. Measurements were collected throughout the growing season and unique post processing

techniques were explored to aide in root detection/visualization. GPR's ability to distinguish root types across different soils conditions were assessed. The SOC portion of this study focused on three sites across the United States to capture the largest range of SOC levels as possible. GPR data was collected on multiple plots at each location, as well as ancillary soil data. Statistics were developed from these measurements and compared with pre-recorded SOC levels to determine GPR's ability to detect differences in SOC.

DEDICATION

To my Dad

ACKNOWLEDGEMENTS

I would like to thank my committee chair, Dr. Haly Neely, for providing me with this opportunity and for giving me the freedom to make this project my own. I would also like to thank my committee members, Dr. Everett, Dr. Hays, Dr. Lewis and Dr. Hays for their guidance and support. A special thank you to Dr. Everett for graciously letting me use his equipment and allowing me to be a part of his research group. I would also like to thank Dr. Cristine Morgan, without her my interest in soil science would never have sparked and none of this would have been possible.

Thanks goes out to the faculty and staff of the Soil and Crop Sciences Department, especially the students in the soil physics and hydropedology group. For spending countless hours in the Texas summer sun I have to thank Candice Medina, Nick Frisbee, Kenny Le, Perry Bekewe, Lauren Tomlin and Gregory Rouze. I wouldn't have survived without their help.

Finally, I have to thank my Mom and Dad. I might have driven us all a little insane along the way but their constant support and encouragement made the hard days a little easier and I wouldn't have made it through this in one piece without them.

CONTRIBUTORS AND FUNDING SOURCES

This work is supervised by a thesis committee consisting of Professor Haly Neely of the Department of Soil and Crop Sciences, Professor Dirk Hays of the Department of Soil and Crop Sciences, Professor Mark Everett of the Department of Geology and Geophysics, Professor Katie Lewis of the Texas A&M Agrilife Research and Extension Center, and Professor Ben Wu of the Department of Ecosystem Science and Management. The MATLAB and gprMax code in Chapter II, III, IV and V was written in collaboration with Richard Kobylinski. All other work conducted for the thesis was completed by the student independently. Graduate study was supported by Department of Energy ARPA•e grant "Developing ground penetrating radar (GPR) for enhanced root and soil carbon imaging: Optimizing bioenergy crop adaptation and agro-ecosystem services."

NOMENCLATURE

AEA	Average Envelope Amplitude
EM	Electromagnetic
EMI	Electromagnetic Induction
EPT	Energy Per Trace
EPTSM	Energy Per Trace Spatial Mean
ETS	Early Time Signal
FFT	Fast Fourier Transform
GPR	Ground Penetrating Radar
IPM	Integrated Pixel Magnitude
MEPTSM	Mean Energy Per Trace Spatial Mean
MIPM	Mean Integrated Pixel Magnitude
NMM	Neutron Moisture Meter
RMSD	Root Mean Square Difference
RWC	Root Water Content
Rx	Receiver
SBW	Spatial Bandwidth
SFW	Spatial Filter Width
SOC	Soil Organic Carbon
Tx	Transmitter

TABLE OF CONTENTS

Page

LIST OF FIGURES

Page

LIST OF TABLES

Page

CHAPTER I

INTRODUCTION

One of the primary methods to determine what lies below Earth's surface is to excavate which permits a direct visualization. However, such invasive methods are labor intensive and often lead to an irreversible disruption of the natural subsurface environment. During the 20th century, a variety of non-invasive geophysical tools were developed to aid in subsurface exploration including: 1) electrical resistivity (e.g. Arjwech et al., 2013; Udphuay et al., 2011) and; 2) electromagnetic induction (e.g. Paine et al., 2003). For agricultural purposes, these geophysical techniques to investigate subsurface physical properties routinely focus on monitoring soil attributes such as electrical conductivity (a property directly related to salinity) and moisture content. Using these techniques, farmers can optimize agricultural practices to best suit the characteristics of the soil. However, an under-developed aspect of subsurface monitoring is the ability to phenotype roots in situ, i.e. in the field. Such an ability would provide more information, in conjunction with soil characteristics, which could improve plant productivity (Comas et al., 2013; Lynch, 1995 & 2011). The information gained from accurately phenotyping roots can lead to improved crop growth by matching desired root characteristics to specific site attributes and production goals. Information such as root mass assessment can aid in determining carbon sequestration potential, which can have positive environmental, economic and social impacts. Novel geophysical techniques and devices are being explored to accurately and nondestructively phenotype roots in the field. Ground penetrating radar, or GPR, is an established geophysical mapping tool that has the potential to accurately characterize root physiognomies nondestructively in the field. (Barton et al., 2004; Butnor et al., 2001 & 2003;

Hruska et al., 1999). However, in typical GPR applications the soil is treated as a homogenous media. Unfortunately, this method does not capture the variations in soil electromagnetic properties that naturally exist throughout a soil profile. These variations in soil characteristics have the potential to impact GPR's ability to phenotype roots if not taken into account. The aim of this thesis is to assess the ability of GPR to differentiate root phenotypes at fine spatial scales based on the detection of contrasts in dielectric permittivity by linking GPR measurements with soil electromagnetic data.

1.1 Background

Root phenotyping is a vital tool in agricultural production because control of intrinsic root characteristics and features, through crop and site-specific selection, can help maximize growth and improve rooting system interactions with the surrounding soil environment. The ability to quickly and accurately phenotype root architecture can enable plant breeders to increase plant productivity, enhance potential for carbon sequestration, optimize fertilizer application and improve water use strategies (Iyer-Pascuzzi et al., 2011; Richards et al., 2010). The most prevalent techniques for root phenotyping are deployed in laboratories or greenhouses. Typically, crops are grown in soil pots or gel media and monitored throughout the life of the plant (Zhu et al., 2011). Additionally, newer technologies, such as x-ray computed tomography and magnetic resonance imaging, are being explored to enhance three-dimensional visualization of root systems (Clark et al., 2011). However, these artificial systems limit or completely remove the natural interaction of soil and roots in an undisturbed environment, which is vital to understanding root functionality.

The primary tool for field classification of root phenotypes is the mini-rhizotron. The mini-rhizotron is a portable version of a rhizotron structure, which is a large, below-ground enclosure that contains transparent panels which enable users to noninvasively view rooting systems (Huck et al., 1982; Johnson et al., 2011). A mini-rhizotron is a portable, hand-held device also used for root visualization. A mini-rhizotron can provide valuable information on rooting systems, however, it has several limitations. Though the zone of soil disturbance is smaller than conventional excavation techniques, a mini-rhizotron installation nevertheless changes the soil environment, and artifacts generated by the installation process can affect the data. Furthermore, there is an extended time delay between tube installations and the time at which a root system can be viewed at pre-disturbance levels. Moreover, only a single plant can be monitored at a given time. With these limitations on current root phenotyping technologies there is a definite need for a near-surface, or proximal sensor to nondestructively and rapidly phenotype roots in the field. Specifically, in this thesis, ground penetrating radar is explored as a possible technique and how the natural variations in soil conditions can impact the GPR signal and influence its ability to potentially detect fine roots. In addition to investigating the feasibility of GPR as a root phenotyping tool, its ability to detect spatial variations in soil-surface levels (0-15cm) of soil organic carbon (SOC). Like root phenotyping, monitoring SOC in the field is limited by the availability of devices which have the capacity to detect small-scale variability. SOC data provides valuable information to farmers on overall soil health to help increase productivity and maximize carbon sequestration. In most field applications the primary technique used to determine SOC is soil coring. The cores are analyzed in a lab after collection. There is a lack of tools that can rapidly, nondestructively and inexpensively determine SOC in the field.

Herein the ability of GPR to detect differences in SOC levels in a number of field situations is tested.

1.2 Ground Penetrating Radar

Ground penetrating radar is a near-surface geophysical technique that can be used for geological mapping amongst many other applications. GPR employs the emission and reflection of short, high-frequency (10 – 2000 MHz) pulses of electromagnetic energy within the ground to map subsurface dielectric contrasts, which may be regarded as "anomalies" (Davis et al., 1989). The technique began to garner considerable attention in the 1970s particularly in the field of civil engineering. As GPR became more refined its uses began to expand and it started being used as a tool to locate underground targets such as containers, tunnels, cables, contamination plumes, and voids (Annan, 2002). Figure 1 shows two examples of GPR units. Figure 1B is a Sensor & Software's PulseEKKO unit (Sensors & Software, Mississauga, Ontario, Canada), which was used in the root phenotyping experiments, while Figure 1A is an IDS GeoRadar RIS-Hi-Mod unit (IDS Georadar, Pisa, Italy) which was used in the SOC experiments.

Over the last few decades the uses of GPR have steadily expanded with applications in archaeology, hydrogeology, forensics, bedrock detection and locating landmines and unexploded ordnances (Daniels, 1988; Doolittle et al., 1995; Hammon III et al., 2000; Schultz, 2007). In agricultural science, GPR attracted attention with its ability to map soil variability (Johnson et al., 1982). From there, the agricultural applications of GPR began to expand with the mapping of more specific soil parameters (Adamchuk et al., 2004; Hubbard et al., 2002), the detection and characterization of underground hydrological conditions that influence plant productivity (Freeland et al., 1998), and finally the detection of coarse tree roots (Butnor et al., 2001; Hruska

et al., 1999). It is GPR's proven ability to detect large roots that will be intend to expounded upon to test its feasibility at smaller scales to detect the fine roots of crop plants while taking into consideration changes in soil electromagnetic parameters.

A  B 

Figure 1: Types of GPR units. (A) IDS RIS Hi-Mod. (B) Sensors & Software PulseEKKO Pro

As a plant matures, the rooting system expands to compensate for the increased amount of water the plant requires for growth. The growing rhizosphere, or area around a growing rooting system, extracts water from the surrounding soil to replenish its water stores. This exchange creates small scale variations in soil moisture surrounding a plant root. These small-scale changes in water content could serve as reflectors for a GPR signal. The nature of the signal reflection may contain information about root structure and biomass. Ground penetrating radar works by emitting an electromagnetic pulse from a transmitter at a given center frequency. The pulse propagates through the subsurface media until a boundary of contrasting electrical

characteristics is encountered, e.g. an interface between roots and the surrounding soil. The signal is then reflected and returned to a receiver. A Tx antenna is used to propagate the transmit pulse, while a Rx antenna is used to capture the reflected signal. Figure 2 shows the basic functionality of GPR to detect subsurface anomalies. The depiction of the GPR unit in Figure 2 assumes that the Tx antenna is spatially separated and distinct from the Rx antenna, which is the case for the two units shown in Figure 1. However, there is nothing to preclude a GPR unit from using the same antenna for transmit and receive.

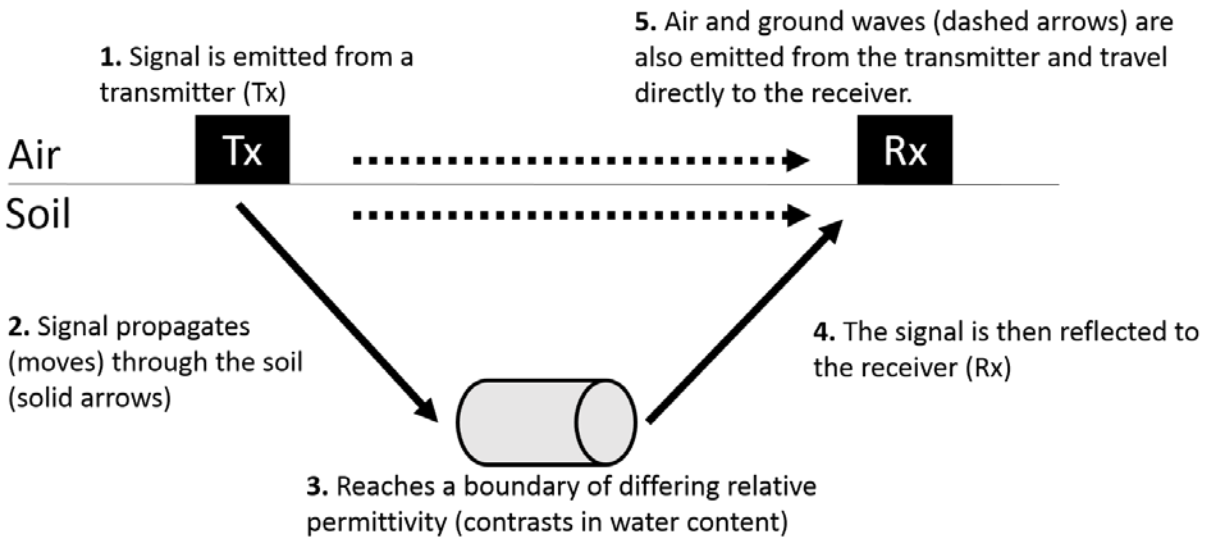

Figure 2: Basic functionality of a GPR unit.

The propagation of an electromagnetic wave is described by Maxwell's equations, which comprise Ampere's Law and Faraday's Law, along with laws governing conservation of electric charges and magnetic dipoles. These equations may be combined into a single vector wave

equation that governs how an electric or magnetic field propagates, interacts and is influenced by objects (Maxwell, 1865; Annan, 2005). Equations 1-4, shown below, represent Maxwell's four distinct equations in differential form, where D is the electric flux density in C/m^2, ρ is the volume charge density in C/m^3, B is the magnetic flux density in Wb/m^2 (or Tesla), E is the electric field intensity in V/m, H is the magnetic field intensity in A/m, and J is the current density in A/m^2. Note that all of the above quantities, except for the charge density, are vectors, and that D = εE, where ε is the permittivity of the medium in C/V-m, and that B = μH, where μ is the permeability of the medium in V-s/A-m. From these four equations and several vector operator identities, the wave equation can be derived, which describes how the electric field propagates in space and time from one location to another. It is the electric field detected by the receiver antenna that is the measured quantity in GPR applications.

$$\nabla \cdot D = \rho \qquad \text{Gauss' Law} \tag{1}$$

$$\nabla \cdot B = 0 \qquad \text{Gauss' Law for Magnetism} \tag{2}$$

$$\nabla \times E = -\frac{\partial B}{\partial t} \qquad \text{Faraday's Law} \tag{3}$$

$$\nabla \times H = -\frac{\partial D}{\partial t} + J \qquad \text{Ampère-Maxwell Law} \tag{4}$$

The pulse emitted by a GPR transmitter is influenced by contrasts in soil electromagnetic properties, specifically permittivity, ε, permeability, μ, and conductivity, σ (Benedetto et al.,

2017). All three characteristics impact the propagation of an electromagnetic wave; however, it is most importantly at the boundaries of contrasting permittivity that a signal will be reflected and returned to the receiver (Daniels, 2004). The relative permittivity, also referred to as the dielectric constant is given by $\varepsilon_r=\varepsilon/\varepsilon_0$, where ε_0 is the permittivity of free space. For a given material, the ε_r is a measure of how much the internal electrical field generated by the dipole moments of the constituent molecules opposes an idealized applied electrical field, for example, one that is generated between two oppositely charged plates in a vacuum (Hayt et al., 2012; Robinson et al., 1999). Polar molecules, such as water, generate large internal electrical fields and therefore have a high relative permittivity, $\varepsilon_r = 80$, whereas substances such as dry sand or limestone have significantly lower values, with ε_r in the range of 3 to 8 (Everett, 2013; Wang et al. 1980). Since water has such a high relative permittivity, the volumetric water content, θ_w, is the most influential parameter determining the relative permittivity of subsurface bulk material, such as soil. The relationship between relative permittivity and volumetric water content of soil may be described by Topp's equation (Topp et al., 1980).

$$\theta_w = -5.3 \times 10^{-2} + 2.92 \times 10^{-2}\varepsilon_r - 5.5 \times 10^{-4}\varepsilon_r^2 + 4.3 \times 10^{-6}\varepsilon_r^3 \quad (5)$$

Soil volumetric water content can change spatially both horizontally across a field and vertically throughout a soil profile. Changes in topography, soil texture, organic matter content, and compaction can influence the amount and movement of water within and through a soil system. These variations in soil moisture drive changes in relative permittivity which cause part of a transmitted electromagnetic signal to be reflected back to a receiver. For a medium with given ε_r, the velocity of a signal propagating within that medium can be calculated using the

formula derived by Davis and Annan (1989), where c is the velocity of an EM wave in a vacuum:

$$v = \frac{c}{\sqrt{\varepsilon_r}} \tag{6}$$

This relationship, in turn, can be used along with the signal travel time to calculate the approximate depth to a given reflector using the simple law that distance is the product of velocity and travel time. Note that the above equation is indicative of the wave velocity at the depth or soil layer with that value of ε_r. Typically, the soil medium is not homogeneous since changes in volumetric water content with depth will in turn effect the relative permittivity via Topp's equation. Thus, in typical cases the soil medium is multi-layered with varying values of relative permittivity and wave velocity, which would need to be taken into account in any signal processing to arrive at a more accurate estimation of reflector depth.

As stated above, a GPR system consists of a transmitter (Tx) and a receiver (Rx). The transmitter comprises a signal generator that emits an electromagnetic pulse at a given voltage and center frequency, and a transmit antenna, which converts this voltage to an electric field which is radiated outwards. The receiver consists of a receive antenna and associated electronics, where the former converts the received electric field to a voltage, and the latter conditions the signal for further processing. Note herein that the resultant signal, prior to any additional processing, is referred to as the "raw" or recorded GPR signal. By changing the center frequency of the emitted pulse, the depth of signal penetration can be altered. At higher frequencies the electromagnetic pulse does not penetrate as deep but provides higher spatial resolution due its smaller wavelength. At lower frequencies, a pulse can propagate to greater depths but at the cost

of decreased spatial resolution (Jol, 1993). Depth of penetration is also influenced by the electromagnetic properties of the medium through which the pulse is travelling. A GPR signal is strongest in media that are less conductive such as dry, sandy soils. Whereas, a signal will be more attenuated, and consequently more difficult to detect, in a wet clayey soil characterized by high conductivity (Daniels, 2004). Clay soils have high rates of attenuation because of the ability of clay to absorb water, as evidenced by higher cation exchange capacities compared to sandier soils (Saarenketo, 1998), and certain types of clays (smectite and vermiculite) have higher rates of attenuation than others (kaolinite, mica). Additionally, the type and amount of salts present, in soils of any texture, can lead to high rates of attenuation due to the interaction of ions with the electromagnetic pulse (Tosti et al., 2013). All of these characteristics influence the conductivity of the soil which is the main driver of signal attenuation (Doolittle et al., 1982 & 2007). However, for the conductivities of interest in this application, e.g. 0.01 to 0.02 S/m, the relative permittivity also have an effect on signal attenuation with lower values experiencing more attenuation than higher values. With the appropriate center frequency selected for the specific field conditions and project objectives, the pulse will propagate through the soil until it reaches an interface of contrasting dielectric properties. The reflected, or in the case of co-located Tx-Rx antennas, the back-scattered signal is then detected by the receive antenna. In addition to the reflected signal, a GPR receiver antenna also senses the direct ground and air waves. Direct ground and air waves are the portion of the electromagnetic pulse that travels directly from the transmitter to the receiver, respectively through the ground and through the air. Ground waves travel in the top portion of the subsurface material and air waves propagate above ground. The characteristics of data obtained from both reflected signals and direct waves provide information on subsurface properties and aid in the detection of buried objects. Note that effects of the direct

waves are often suppressed from the received signal in order to produce a more accurate version of the signal scattered by the subsurface anomalies.

In GPR data collection there are three basic scan types: A, B, and C. An A-scan consists of a single radar trace or waveform collected from a single GPR location. A B-scan is a sequence of A-scans acquired by moving the GPR unit in a given direction. Thus, B-scans, after suitable processing, e.g. removal of hyperbolic diffracted energy, provide a 2D visualization of the subsurface in a vertical plane below the GPR unit (Özdemir et al., 2004). For the discussion herein a conventional three axis rectangular coordinate system is assumed, where the GPR unit is assumed to be moved along the surface in the "x" direction. The "z" direction defines the vertical dimension where positive values represent depths below the surface. The above convention implies that an x-y plane defines the surface of the earth when z = 0. A C-scan is a collection of B-scans, where a given B-scan is offset in the y direction from other B-scans by a specified line spacing. Thus, a C-scan after suitable processing can provide a 3D image, or sequence of 2D image slices. Examples of the GPR signals collected in A-scan and B-scan formats are shown in Figure 3. Figure 4 shows the results of a processed C-scan from a controlled experiment wherein a metal pipe was buried at a 45^0 angle in the x-y plane at a depth of ~0.67 m. Each image within Figure 4 shows the recovered image in the x-y plane at the specified depth below the surface.

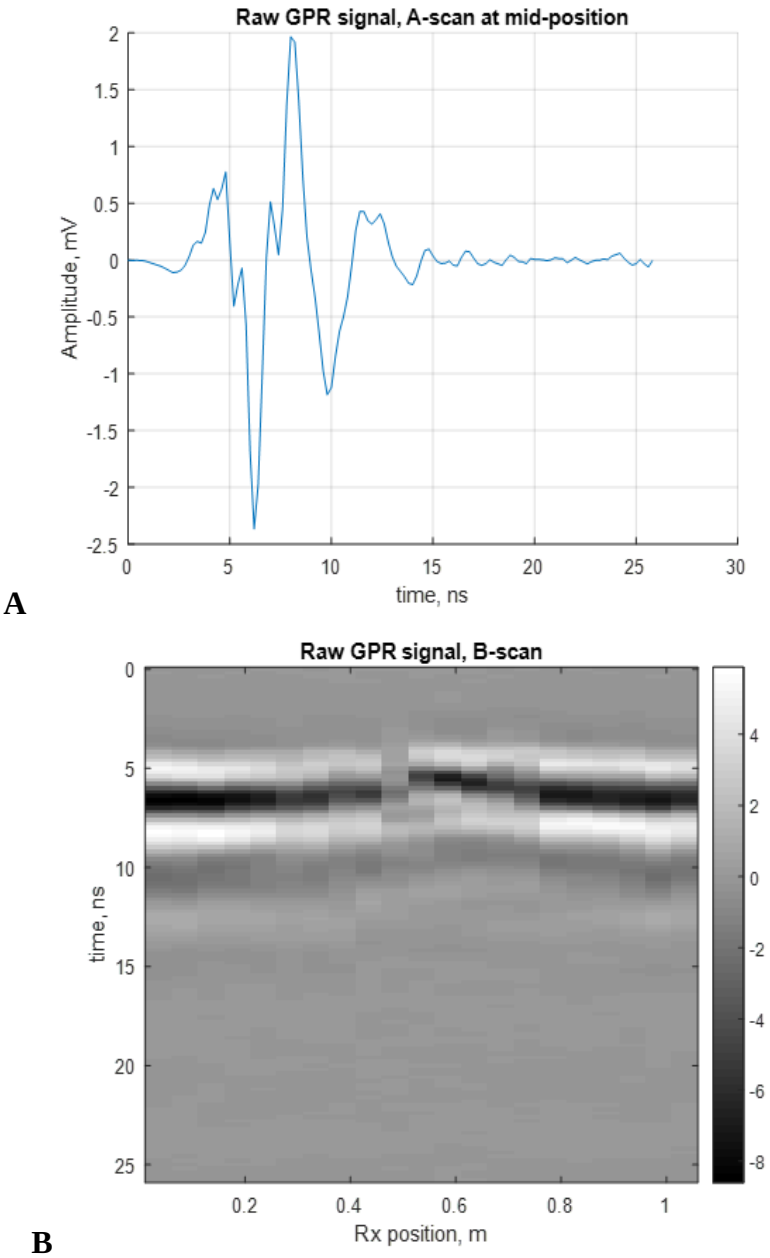

Figure 3: GPR data visualization (A) A-scan or trace. (B) B-scan.

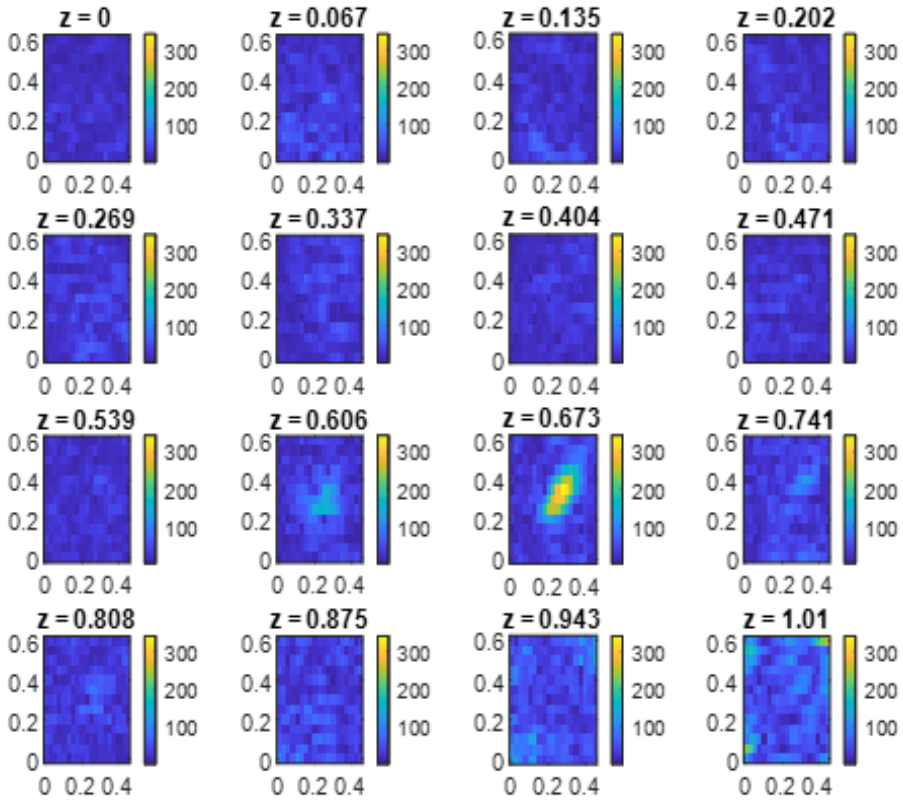

Figure 4: GPR data visualization. C-Scan.

1.3 GPR Data Processing

Once the raw GPR signal data is obtained, post processing must first be performed to aide in signal interpretation. A great number of post processing techniques exist and different GPR analysis platforms utilize different sets. The type and amount of processing used depends on the goals of each project and finding the appropriate combination of processing steps can prove challenging. A flow chart of the possible processing steps applied to GPR data collected as part of this project is shown in Figure 5.

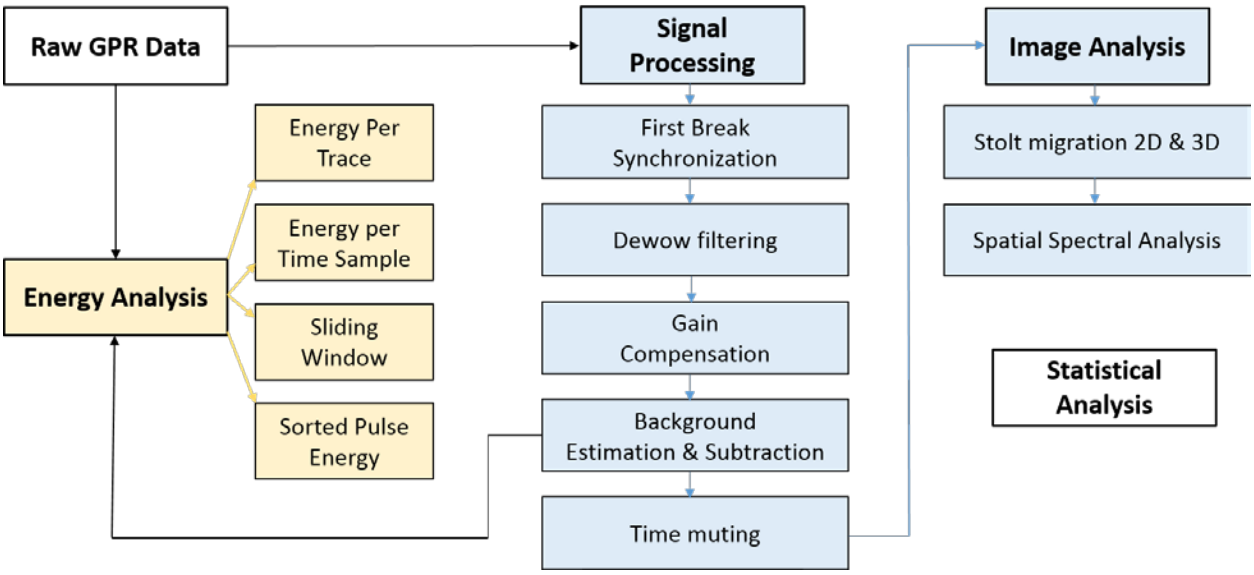

Figure 5: Flow chart of the different analysis techniques and signal processing procedures.

There are three main types of processing/analysis: (1) Signal processing, (2) Image analysis and (3) Energy analysis. In addition, various statistical analyses were performed on various measures to see how well they correlated with other measures. Note that all of the processing shown was written or was available open source in MATLAB, except for some of the statistical analysis, where certain R packages were used. Before describing each of the three main types of processing in some detail it is important to note that the raw GPR signal data provided by the GPR unit used in the root phenotyping experiments includes "stacking" of each of the signal traces (A-scans). In stacking, multiple traces, e.g. 64 was used in this project, are collected at each location, added and then averaged to form a new composite signal. If the signal is "coherent" over the summation period, then the Signal to Noise Ratio (SNR) is improved by the square root of the number of traces collected. The end result is a very "clean" signal.

1.3.1 Signal Processing

Referring to Figure 5, the steps within the signal processing heading are typically used universally to recover an estimate of the signal due to just the sub-surface anomalies, or what is referred to as the scattered signal. These processing steps include: first break synchronization, dewow, gain compensation, background estimation and subtraction, and time muting. First break synchronization is used to align in time the first occurrence or starting point of all GPR traces. This synchronization allows for more accurate comparisons of traces at different locations along the transect and leads to better performance in the processing that follows. Dewow is often applied to traces to remove the unwanted decaying low frequency, or 'wow' portion of the signal that follows the transmitted pulse. The 'wow' portion of the signal can interfere with the desired high frequency reflections. This low frequency decay is due to a number of factors including the location of the transmitting and receiving antenna in relation to one another and the electrical properties of the soil (Annan, 2009; Cassidy, 2009; Neal, 2004). Note that low pass filtering was applied to the raw input signal before dewow to remove any high frequency noise, and that Wavelet de-noising was tried to further improve signal quality. Wavelet denoising works by localizing certain features in the data to different scales, and by doing so portions of the signal can be maintained while the unwanted portion can be attenuated or removed completely. However, the latter did not provide any significant improvement since the signal was already quite clean due to the signal stacking within the GPR unit.

Next, gain functions can be applied to help boost weaker signals at later times corresponding to greater depths. As an electromagnetic wave propagates through the soil the signal is attenuated, the extent of which depends on the electromagnetic properties of the soil. To

compensate for that loss, different types and amounts of gain can be applied to ensure that deeper subsurface anomalies are represented appropriately (Robinson et al., 2013). In the gain compensation code four different types of gain functions were developed: (1) constant, (2) alpha, (3) alpha plus spreading, and (4) user specified alpha. As the name implies, the constant setting corresponds to a constant value used for all times/depths. The gain value used for this setting was a value of one and hence this corresponds to a "no gain" condition. This setting was useful for processing of the signal returns that were compared with the percent soil organic carbon (SOC) measurements. Since the percent SOC was typically measured in the first 15 cm of depth, it made sense to select the no gain option since there is little signal attenuation over the depth of interest. The second type of gain is referred to as the alpha setting, which means that the gain applied was based on developing estimates of the attenuation coefficient, α. This coefficient is based on estimates of the relative permittivity, ε_r, and the conductivity, σ, and is given by Equation 7.

$$\alpha = \omega\sqrt{0.5\mu\varepsilon'}\left(\sqrt{1+\left(\frac{\varepsilon''}{\epsilon'}\right)^2}-1\right)^{1/2} \tag{7}$$

In Equation 7, w is the radian frequency = $2\pi f$, where f is the center frequency of the transmit pulse, μ is the permeability given by $\mu = \mu_0\mu_r$, ε' is the real part of the complex permittivity given by $\varepsilon_0\varepsilon_r$, ε" is the imaginary part of the complex permittivity given by σ/w, and α is in units of Nepers/m. Estimates of the conductivity were obtained either directly from EM38-MK2 measurements, or indirectly through empirical equations using θ_w measurements from a neutron moisture meter or a theta probe, see section 3.2 for details. For this application the relative

permeability, μ_r is always set to 1 since the soil was assumed not to have any magnetic properties of note. In the code implementation, the wave propagation path from the Tx to the reflector at a certain depth and then from that reflector to the Rx is split into a number of equal, near-vertical segments of length ΔL. The parameter α is then calculated for each segment with the resulting signal loss over that segment given by Equation 8, and total loss over the path then given by Equation 9

$$e^{(-\alpha \Delta L)} \tag{8}$$

$$e^{\left(-\Delta L \sum_{i=1}^{N} \alpha_i\right)} \tag{9}$$

In Equation 9 α_i is the α value for the i^{th} segment, and N is the total number of segments. The gain determined compensates for the total loss with values calculated over the depth of interest. The alpha gain setting was used for almost all of the analysis (except for the processing of the SOC related data) since it was able to provide some reasonable gains at depths of interest, but not an overwhelming amount of gain. It must be commented that gain setting in GPR processing is very much ad-hoc in nature. The third gain type is referred to as alpha plus spreading and as the name implies it consists of the alpha loss term just described plus a spherical beam spreading loss. The wave that propagates from the Tx antenna can be modeled as a spherical wave and as such it will lose energy with propagation distance. The loss incurred is approximated by $(1/L)^s$, where, L is the propagation length, and s is typically set to a value of 1 or 2. This gain setting was found to produce quite a bit of gain at the greater depths, and as such was only used in the controlled experiment which attempted to locate two metal pipes buried at known “moderate”

depths, see Chapter III. The final gain type implemented is a “user specified alpha” option, which allows one to manually set the attenuation coefficient expressed in dB/m. The code then converts this value to the attenuation coefficient, α in Nepers/m by dividing it by 8.69. This value of α would then be used for each ΔL segment of path length as described previously for the alpha gain setting. This option was included in case an estimate of the soil attenuation was known in advance and to understand the effect of differing values of conductivity on overall performance.

The next processing step is referred to as background subtraction or removal, which is typically used to enhance dipping effects and is often applied to remove the influence of direct air and ground waves. As such, it is a critical step for forming an estimate of the scattered signal. One of the more common types of background subtraction schemes is referred to as “average” background subtraction. In this technique an “average” trace is calculated across all traces, which is then subtracted from each trace. Another type of background subtraction is referred to as “localized” background subtraction. In this technique, a “localized average” is calculated across traces within a spatial window, which is then subtracted from the total signal level of the trace centered within that specified spatial window. The spatial window is also referred to as the spatial filter width (SFW). Either technique generates an estimate of the background portion of the signal which is referred to as E_b. This estimate of the background is then subtracted from the total signal after gain compensation, E, to form an estimate of the received signal due to scattering from the sub-surface anomalies of interest, E_s. This resultant signal is also referred to as the scattered signal and is given by Equation 10 below.

$$E_s = E - E_b \tag{10}$$

Figure 6 shows example B-scans for E, E_b and E_s and how they differ. E_s takes the form of $E_s(x,t)$ for B-scans and $E_s(x,y,t)$ for C-scans, where x and y define the GPR unit Rx location along the transect, and t is the time variable. The variable name E_s was selected to indicate that this signal is proportional to the received electric field even though it has been converted to a voltage in the Rx. Finally, time-muting is applied to remove portions of the scattered signal that are not relevant to the depths of interest. The specific amount of time muting implemented followed the guidelines set forth in Persico (2014), which recommended that the signal prior to the first peak of the raw signal be muted.

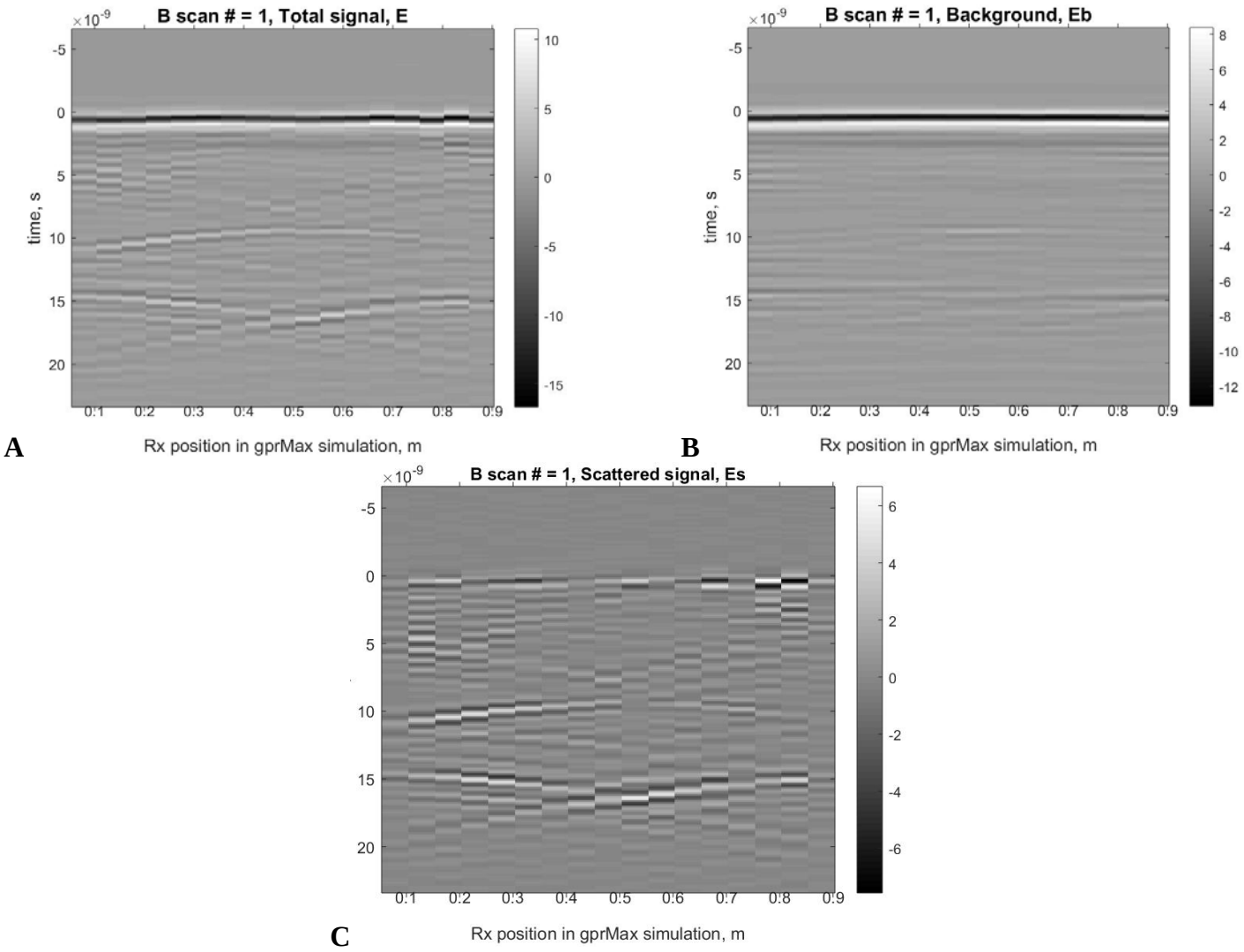

Figure 6: B-scans of the different returned signals. (A) Total Signal E. (B) Background Signal E_b. (C) Scattered Signal E_s.

1.3.2 Image Analysis

The estimate of the time-muted, scattered signal developed under the signal processing heading is then input to the image analysis section of the processing flowchart (Figure 5) where the final images are developed and analyzed. A number of GPR imaging techniques exist to transform a GPR signal into a 2D or 3D image. These techniques process the data collected from either a single B-scan to produce a 2D image, or from a C-scan to produce a 3D image or a collection of 2D image slices. Multiple techniques were explored but the Stolt w-k (frequency-wavenumber) migration algorithm (Stolt, 1978) was preferred due to its computational efficiency and capacity to process multiple soil layers of differing electrical properties. Phase shift migration (Skjelvareid, 2012) was also explored as a possible algorithm; however, the results were very similar to Stolt, and since phase shift migration does not utilize an FFT in the depth (z) dimension it is less computationally efficient than Stolt. In addition, a diffraction tomography-based approach developed by Persico 2014 was also investigated but was found to be computationally demanding since FFTs could not be exploited, and further, was not readily adaptable to multiple soil layer processing.

Migration is a commonly used technique in GPR processing that collapses the energy that is spread over GPR diffraction hyperbolae back to their apices whence the diffracted energy originated. This determines more precise spatial location, size, and electromagnetic properties of the buried objects that produce diffractions (Formel, 2003; Özdemir et al., 2004). The Stolt algorithm is also attractive since open-source 2D versions are available in MATLAB and within the Sensors and Software processing suite. In addition, a 3D version was available, but only in open-source MATLAB code. The 2D and 3D open-source code is preferable since it includes

code which support the processing of multiple soil layers, which is more representative of the soil structure encountered in the field as opposed to a single homogeneous layer. This ability to process multiple soil layers is facilitated within the open source code by a soil layer thickness profile input and an associated wave velocity profile input. The Stolt algorithm is computationally efficient as it is based upon the Fast Fourier Transform (FFT). In the 2D algorithm, the received scattered field from a B-scan is converted from its original space-time representation, $E_s(x,t)$ to a wavenumber-frequency representation $E_s(k_x,w)$ via use of a 2D-FFT. The variable k_x is the spatial frequency or wavenumber in radians/m, and w is the angular frequency in radians/s. The representation $E_s(k_x,w)$ is then converted to a full wavenumber representation, $E_s(k_x,k_z)$ by use of a procedure which maps w to k_z (whence the algorithm is named). After suitable interpolation to ensure a uniform grid, a 2D inverse FFT is applied to retrieve a "focused" image of the scattered field, $E_s(x,z)$. A similar procedure is used to develop a 3D image from the received scattered signal based upon a C-scan by using 3D FFTs.

In this project, images generated by Stolt migration of GPR B-scans were run through an additional 2D FFT to obtain their spatial spectral content, which is quantified with a measure refered to as the spatial bandwidth (SBW) of the image. In the case of a processed C-scan the results were run through a 3D FFT. This processing step is captured in the block labeled spatial spectral analysis in Figure 5. Two measures of SBW were determined corresponding to the bandwidth that encompassed 90% and 95% of the total spectral power. These percentages were selected since the intent was to have a bandwidth criterion that captured most of the power but not quite all of it. These measures were used to detect whether differences in bandwidth existed between GPR data acquired in the presence of plants with different rooting structures (e.g. tap vs. fibrous).

1.3.3 Energy Analysis

A number of energy measures were developed based upon GPR traces or A-scans. The specific measures included: energy per time sample; energy per trace or total energy; sliding window energy; and sorted pulse energy. As shown in Figure 5, these energy measures are calculated for the raw data signal and/or the scattered signal that results after background removal. To begin, Figure 7 shows a subset of traces collected from a B scan for one of the field experiments over a shortened time window. For clarity, only M = 4 traces are shown with only N = 16 time samples per trace with each sample represented by an 'o'. Note, the actual B scan consisted of 200 traces based upon a 10 m transect length, L_x with 5 cm antennae step size, Δx, where $M = L_x/\Delta x$. The actual number of time samples was 130 based upon a time window T_w = 26 ns and a sampling time Δt = 200 ps, where $N = T_w/\Delta t$. The energy per time sample, $E_{ts}(m,n)$ in Joules (J) at the m-th trace location x_m and n-th time sample t_n is given by Equation 11 below, where V(m,n) is the signal level in volts at the m-th trace and n-th time sample, Δt is in s, and a hypothetical one-ohm resistor has been assumed to represent the conversion factor between voltage and energy. Note that the use of the "E" variable to describe these energy measures is not to be confused with the received raw signal, E or the scattered signal, E_s, both of which are in volts. In essence, V(m,n) is the sampled version of either E(x,t) or $E_s(x,t)$.

$$E_{ts}(m,n) = V^2(m,n)\Delta t \tag{11}$$

The energy per trace in the m-th trace, $E_{tr}(m)$ is just the total energy in that trace and is given by Equation 12 below as

$$E_{tr}(m) = \sum_{i=1}^{N} V^2(m,i)\Delta t \tag{12}$$

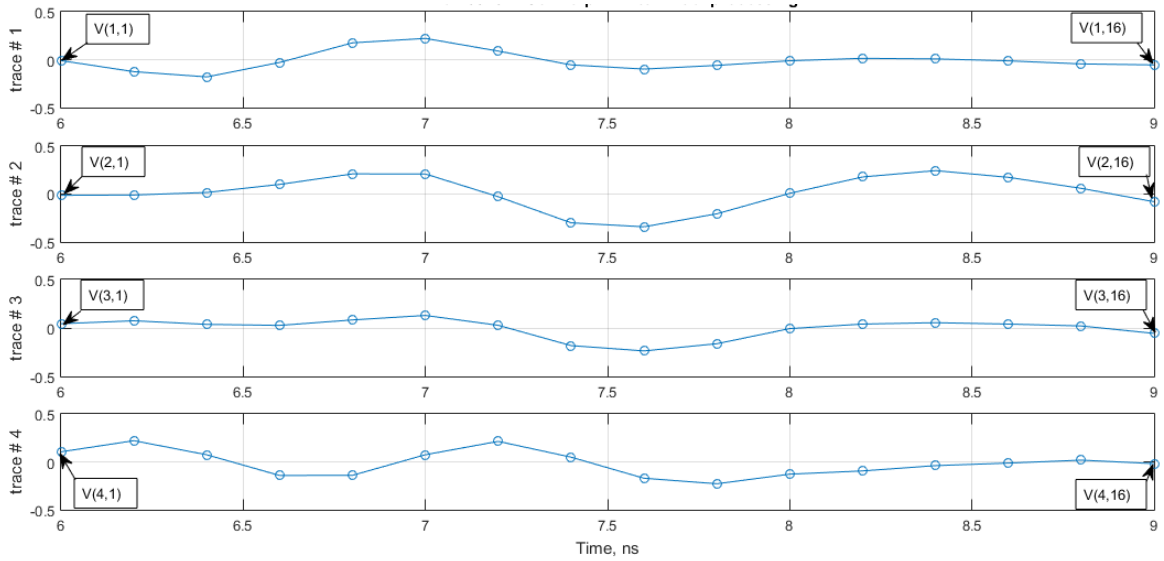

Figure 7: Subset of traces over a shortened time window collected in a typical B-scan.

The sliding window energy measure determines the total energy within a specified time sample window. When the window width is set to one the result is identical to the above energy per time sample (Equation 11) and when set to N it is equal to the energy per trace (Equation 12). Finally, the sorted pulse energy measure sorts the individual excursions above and below the zero level of each trace by the energy that is contained in the excursions. In this project, the energy per trace (EPT) measure was found to be the most useful of the four measures. Specifically, it was used to differentiate locations associated with a plant, expected to have a higher EPT, from locations associated with no plant or just bare soil, expected to have a lower

EPT. In addition, the mean value of the EPT calculated over a given transect was used as a measure to compare with the percent SOC in that location, see chapter V.

1.4 Objectives

The overall objective of this study was to test the feasibility of GPR data to be linked with soil electromagnetic data as a means to detect and differentiate between rooting systems in different soil conditions. In addition, the potential for GPR to act as a tool for quantifying changes in the amount of soil organic carbon present in the surface layer of the soil profile was explored. These goals were accomplished using the following objectives:

1. Model the potential for GPR to detect and differentiate between different types of rooting structures.
2. Assess the potential for GPR to detect root biomass and structure by incorporating soil electromagnetic properties in controlled experiments.
3. Assess the potential for GPR to detect root biomass and structure by incorporating soil electromagnetic properties in field experiments.
4. Quantify the impact of soil organic C on the GPR signal.

CHAPTER II

GPR MODELLING

2.1 Introduction

In contrast to typical GPR applications where the goal is to determine the location of targets such as concrete reinforcing bars at considerable distance below the surface, root phenotyping has some distinctive aspects that should be taken into account and could potentially be exploited. These aspects include: (1) the objects to be detected, i.e. the roots and root structure, are near the surface, and; (2) the plant locations are known. To determine the processing functions that might be best to apply for this application, an electromagnetic (EM) wave propagation simulator was utilized, in which system setup and all of the operating variables could be carefully controlled. To this end, the open-source program gprMax developed and maintained at University of Edinburgh was selected. gprMax solves the 3D Maxwell's equation using a finite-difference time-domain method. Electric and magnetic fields are determined as a function of time as they propagate from a transmitter to a receiver (Warren et al., 2016). gprMax can model different antenna types, absorbing boundary conditions, materials that are anisotropic and dispersive and, importantly, different soil properties and topography. The capacity to modify the soil environment to reflect field conditions enables gprMax to simulate realistic changes in soil dielectric permittivity as related to plant root size, root volumetric water content, and root depth (Guo et al., 2013). Two sets of simulations were run using gprMax to develop synthetic data. The first set was run to test GPR's ability to detect the presence of roots in ideal situations and to determine the influence of changing root characteristics and soil parameters on that ability. The second set was run to verify the suitability of Stolt w-k migration for processing

GPR data collected with a common offset perpendicular configuration. In addition to these simulations, analysis was conducted to determine if there was a significant difference in the spatial spectral content of idealized images of fibrous and tap root plants. The objective for this chapter was to model the potential for GPR to detect and differentiate between different types of rooting structures.

2.2 Simulation 1: Impact of Changing Root Characteristics on GPR Signal

The first gprMax simulation was designed to test two basic hypothesis; (1) That a trace, or A-scan, collected from a location that coincides with a plant will have higher signal returns as compared to a 'no-plant' location, where the latter is typically referred to as the background signal, and (2) to verify that as a root increases in size (diameter) and root water content (RWC) relative to the surrounding soil media, that the GPR signal returns will be higher with each incremental increase in diameter and RWC. The first step was to develop estimated signal returns using a gprMax program script, which emulates the potential field measurement setup shown in Figure 8 of the common offset perpendicular. Per Figure 8, the measurement procedure is to locate the Tx and Rx transducers on either side of a row of plants, and then to record signal traces as the Tx and Rx are moved along in the direction as indicated by the green arrow. Note the green arrow also indicates the row along which the plants are located.

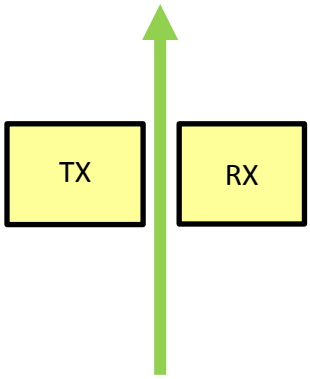

Figure 8: Diagram of perpendicular common offset configuration for GPR antennas.

The gprMax command script was loosely based upon a Sensor's and Software pulseEKKO GPR unit, which was used in all of the controlled and field experiments. Certain parameter values were known for this unit, e.g. the Tx center frequency = 500 MHz (or 1000 MHz) and were set accordingly. However, since certain aspects of this unit are proprietary and unknown, we had to make some assumptions in the simulation modeling with regards to the Tx waveform and the Tx and Rx antennas. For example, for the Tx and Rx antennas the only readily available choice at 500 MHz within the gprMax command set was an ideal Hertzian dipole. Note that the gprMax library does include files for bow-tie antennas (typically used in commercial GPR equipment). However, these files are designed to emulate a GPR unit operating at 1.2 and 1.5 GHz, and as such would not give an as accurate representation of GPR data collected at 500 MHz. Another assumption was that the Tx waveform was a Ricker pulse, which is an option available in gprMax, and is a pulse shape that is commonly used in GPR equipment.

For the purpose of the first simulation a hypothetical plant model based on an immature sorghum plant was constructed. The actual geometry that was modeled with gprMax is shown in

Figure 9, where we have elected to model a slice of the total geometry, where the slice contains just one plant. The intent is to record a single signal trace (A-scan) for different plant models, including the 'no-plant' case.

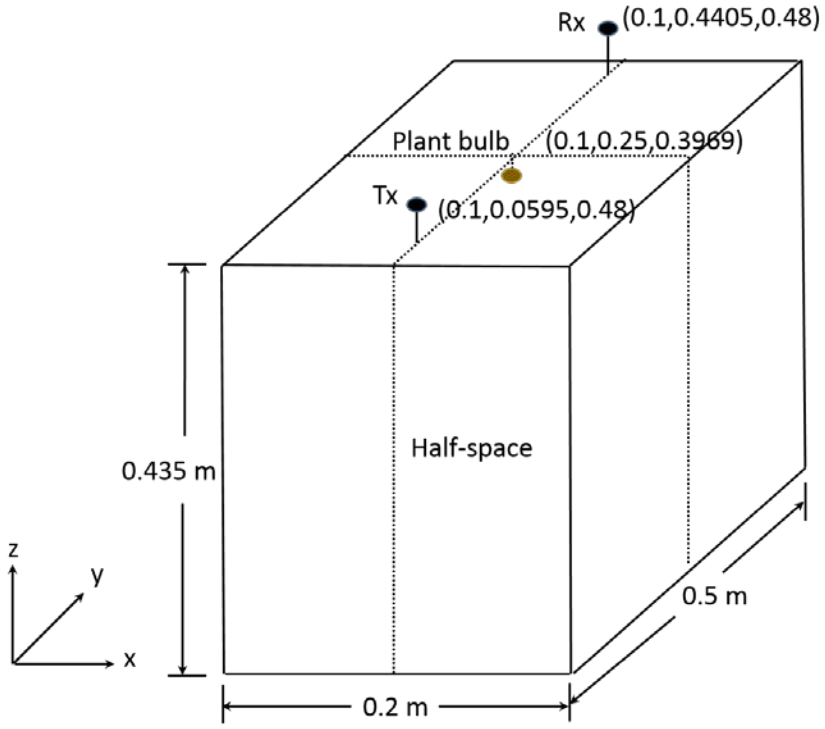

Figure 9: Geometry of gprMax setup.

Ten different scenarios with different plant conditions, classified from 'worst' to 'best-plus' were used to represent different root conditions. The hypothesized model is in an ideal environment and several of the plant characteristic classifications are not feasible in the field but are still used to help demonstrate the overall potential influence of root structure size and water content on GPR signal returns. The plant parts modeled include a bulb section, nodal roots, and a primary root. Note that only the plant bulb location is shown in Figure 9. The bulb was modeled using the gprMax "sphere" command, which specifies the sphere center in x-y-z, the sphere radius, and a material identifier. The roots where modeled using the "cylinder" command, which specifies the x-y-z location of the cylinder faces, the cylinder radius and a material identifier.

The key plant characteristics that were quantified for each model include: bulb diameter, primary and nodal root diameters, primary root length, nodal mean and standard deviation root length, number of nodal roots, and vertical angular spread of the nodal roots. A different RWC was assigned to each model, where RWC is defined as the ratio between the mass of total water to the total root biomass (i.e., root dry weight). The various root relative permittivities, ε_r, and overall root conductivity, σ were determined for each model based upon the RWC value and the respective root diameters per the equations defined in Guo et al. (2013).

The resulting key physical and electrical characteristics of the plant models developed are summarized in Table 1. In addition, the half-space that contains each modeled root needs to be defined. Within gprMax, the half-space is defined by four parameters; relative permittivity, ε_r, conductivity, σ, in Siemens/meter (S/m), relative permeability, μ_r, and the magnetic loss σ_* in Ohms/meter. In real world applications the relative permittivity of a subsurface anomaly and the surrounding media are the key drivers in influencing the effectiveness of GPR since the latter

works by detecting boundaries of differing relative permittivity. In the soil, changes in relative permittivity are driven mainly by changes in soil moisture content per Topp's equation (Equation 5). Therefore, it is important to measure the volumetric water content of the soil. In the simulations the half-space was kept constant throughout all models with a relative permittivity of 4, representative of a dry sand. Additionally, the soil conductivity was kept constant at 0.01 S/m to also represent a dry sandy soil. To determine the signal generated from the half-space/soil media only a 'no-plant', or 'ExRef', model which contained no subsurface anomaly (i.e. plant root) but had the same half-space parameters was also created.

Table 1: Different plant physical and electrical characteristics of the various plant models.

		Worst	Worst-Plus	Average-Minus	Average	Average-Plus-Minus	Average-Plus	Average-Plus-Plus	Best-Minus	Best	Best-Plus
Physical Characteristics	Root water content, %	30	50	70	90	100	110	120	130	150	170
	Bulb diameter, mm	23.3	26.3	30	35	37.9	40.8	43.8	46.7	52.5	58.3
	Primary root diameter, mm	3.3	3.75	4.3	5	5.4	5.8	6.3	6.7	7.5	8.3
	Nodal root diameter, mm	2	2.25	2.6	3	3.2	3.5	3.7	4	4.5	5
	Primary root length, mm	100	133.4	167	200	233	267	300	333	400	467
	Nodal root length, mm	50	66.7	83.3	100	116.7	133	150	166.7	200	233.3
	Nodal root length, standard deviation, mm	25	33.4	41.7	50	58.3	66.7	75	83.4	100	116.7
	# of nodal roots	15	20	24	30	35	39	46	50	60	69
	Vertical angular spread of nodal roots, degrees	20	26.67	33.3	40	43.3	46.7	50	53.3	60	66.7
Electrical Characteristics	Bulb and nodal roots relative permittivity	3.98	8.74	13.92	19.51	22.51	25.74	29.27	33.13	42.11	53.36
	Primary root relative permittivity	3.44	7.35	11.64	16.35	18.91	21.66	24.65	27.91	35.41	44.63
	Root conductivity, S/m	1.00E-05	1.85E-05	3.41E-05	6.31E-05	8.58E-05	1.17E-04	1.58E-04	2.15E-04	3.98E-04	7.36E-04
	Reflection coefficient, bulb and nodal roots	1.25E-03	-0.193	-0.302	-0.377	-0.407	-0.435	-0.460	-0.484	-0.529	-0.570
	Reflection coefficient, primary root	3.77E-02	-0.151	-0.261	-0.338	-0.370	-0.399	-0.426	-0.451	-0.497	-0.539

Figure 10A shows the resulting A-scans, with time in nanoseconds on the x-axis and the received electrical field x component, Ex, in V/m on the y-axis for six of the ten different root models as well as the ExRef trace. Note that all of these results are based upon an Rx dipole with polarization x, which is matched to the Tx dipole also of polarization x. In Figure 10A it is difficult to differentiate between the different models, which is due to the signal being dominated by the direct air and ground waves. In the controlled environment of the simulation, the direct air and ground waves are the only components of the background signal since no other anomalies or variations exist within the half-space. In order to visualize the portion of the signal associated solely with the plant roots, or the scattered signal (E_s), the background needs to be removed. To do this the GPR signal associated with ExRef/no-plant was subtracted from all of the root models leaving only the scattered signal reflected off the root. Figure 10B shows the A-scans for six of the scenarios but with the ExRef removed so only the scattered signal, E_s, remains. From Figure 10B there is a difference in signal levels between the different root scenarios. Figure 10B also confirms that the plant model with the smallest root diameter and lowest water content ('worst') has the weakest signal as opposed to the 'best-plus' model with the largest root diameter and highest root content which had the largest signal. Specifically, for these set of simulation assumptions, the worst model had a maximum negative peak of about -0.0025 V/m, while the best model had a value greater than 20 times that of about -0.055 V/m.

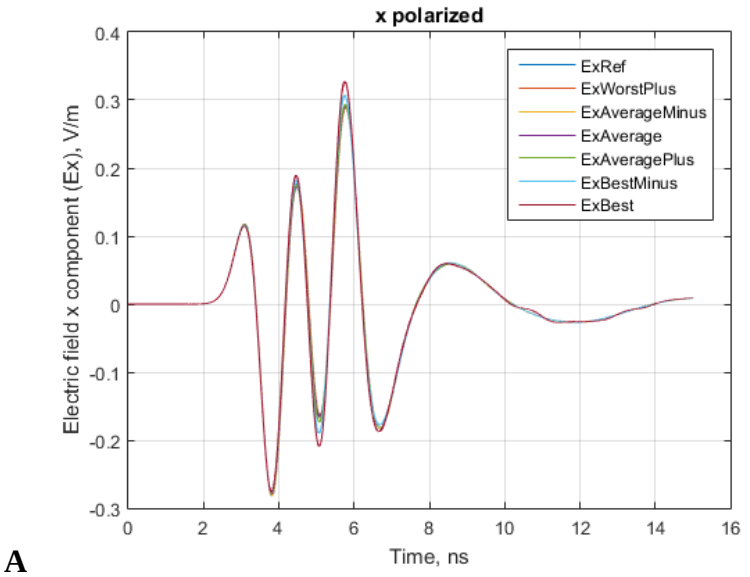

A

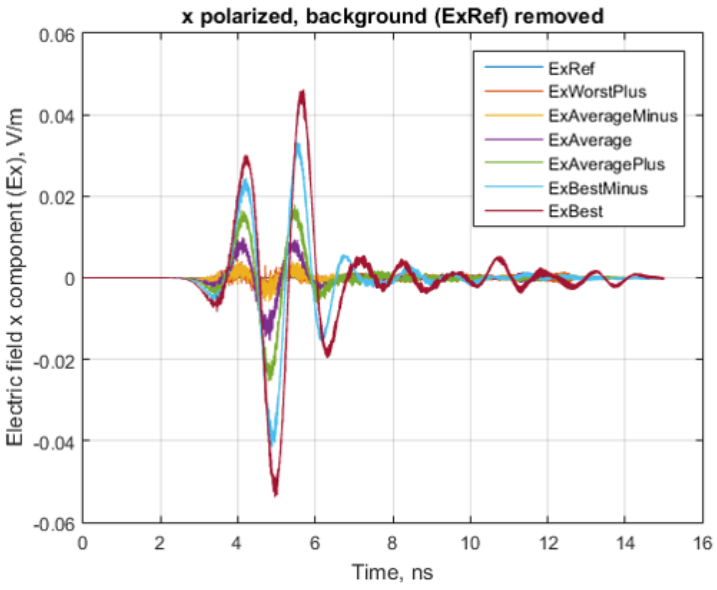

B

Figure 10: Signal comparison between the different gprMax modelled scenarios. (A) Original traces. (B) Traces with ExRef removed (subtracted).

2.3 Simulation 2: Verification of Stolt Migration Algorithm

The second set of gprMax simulations was used to verify the viability of the Stolt migration algorithm to process B-scans and C-scans for purposes of developing 2D and 3D images, respectively. By creating known targets, e.g. a slab with electrical properties different from that of the surrounding soil and locating the slab at a known depth, synthetic GPR signal returns were developed by gprMax. These synthetic signals were then processed to develop an estimate of the scattered signal, which was then input to the Stolt migration algorithm to verify its ability to detect the target. Stolt migration was described earlier in section 1.3.2 along with its main advantages of computational efficiency by virtue of its use of FFTs, and its ability to process multiple soil layers.

To verify 2D Stolt migration processing, grpMax was used to generate a 'slab' of known dimensions and electrical characteristics. The designed slab was 400 mm x 200 mm x 50 mm (x-y-z), and was centered in the x-y plane of the simulation domain at a depth (z-axis) of 500 mm. The GPR data collection configuration was a common offset perpendicular where the Tx and Rx are moved in the x direction but offset in the y dimension as opposed to the x dimension as in conventional common offset. This configuration was used in the controlled and field experiments described in Chapter III and IV to avoid damaging the plants. The y-axis center of the slab was located midway between the Tx and Rx y locations. The slab was assigned a relative permittivity of 2.6 while the surrounding soil media was assigned a relative permittivity of 2.5 as shown in the x-z profile of Figure 11A. The slab and soil conductivity were both set to 0.001 S/m, representative of a relatively lossless medium. Synthetic GPR data was collected over this model using gprMax with the resulting B scan of the raw data envelope as seen in Figure 11B

with time, t, in microseconds on the y-axis and location along the transect in mm on the x-axis. In Figure 11B the characteristic hyperbolic distortion often seen in GPR data is apparent making it somewhat difficult to identify the location of the slab edges.

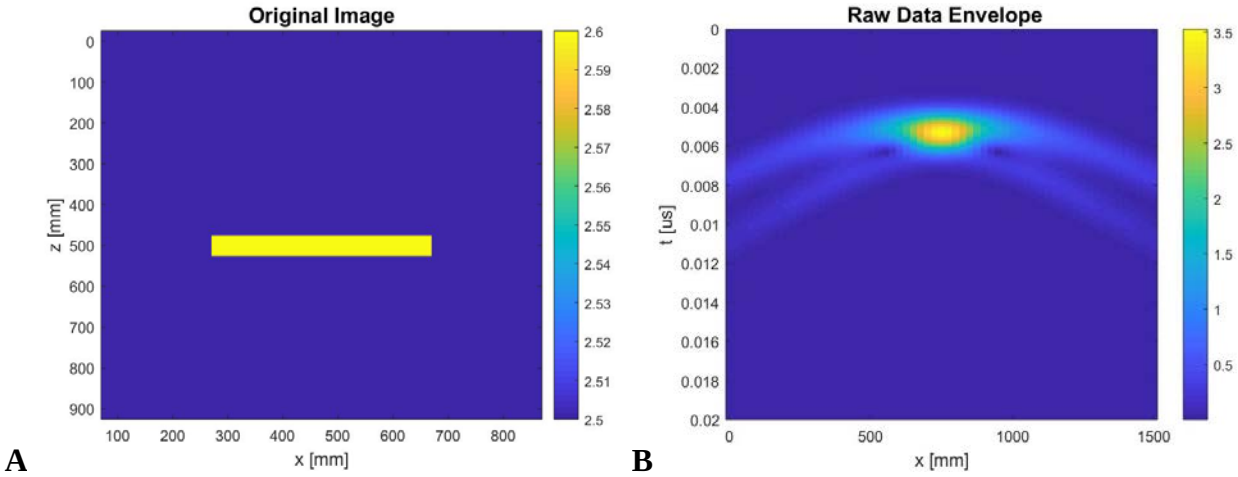

Figure 11: Stolt Migration Algorithm. (A) Original image. (B) Raw data envelope from synthetic GPR data.

The next step is to run the estimate of the scattered signal through the Stolt w-k migration to generate an estimate of the scalar electric wavefield in the x-z plane, $E_s(x,z)$. For this example, we used the 2D version of the algorithm even though the data was collected via the common offset perpendicular configuration with Tx and Rx offset in the y dimension. This appears to be a novel way to process data from such a configuration since we have not seen it described in the literature to date. The 2D version of the Stolt migration algorithm starts by taking a 2D FFT of the scattered electric field $E_s(x,t)$, which converts the scattered signal from a spatial-time domain representation to a wavenumber-frequency domain representation, $E_s(k_x,w)$.

The resulting 2D image of the magnitude of $E_s(k_x,w)$ is shown in Figure 12A. The next step is to write the scattered signal as a function of k_x and k_z, $E_s(k_x,k_z)$ as opposed to k_x and w. This is achieved by mapping every w value to a corresponding k_z value per the following equation

$$k_z = \sqrt{\left(\frac{w}{v_s/2}\right)^2 - {k_x}^2} \tag{13}$$

In Equation 13 v_s is the wave velocity in the surrounding soil given by the expression $c/\sqrt{\varepsilon_r}$ where c is the speed of light in a vacuum. The factor of 2 in Equation 13 converts the velocity to what is referred to as the effective wave velocity for the exploding reflector model (Skjelvareid, 2012). The resulting values for k_z will not typically lie on a uniform grid and thus, interpolation (resampling) is required to achieve this thereby enabling the use of the FFT in the final processing step. The 2D image after suitable interpolation/resampling is shown in Figure 12B. The final step of Stolt migration is to recover an estimate of the scalar wavefield by taking an inverse 2D FFT of $E_s(k_x, k_z)$ to generate $E_s(x,z)$. Figure 12C shows the recovered image to confirm that Stolt migration was successful in recovering an estimate of the original image from the raw synthetic GPR data, albeit with some noise in adjacent pixels and a slight offset from the correct depth.

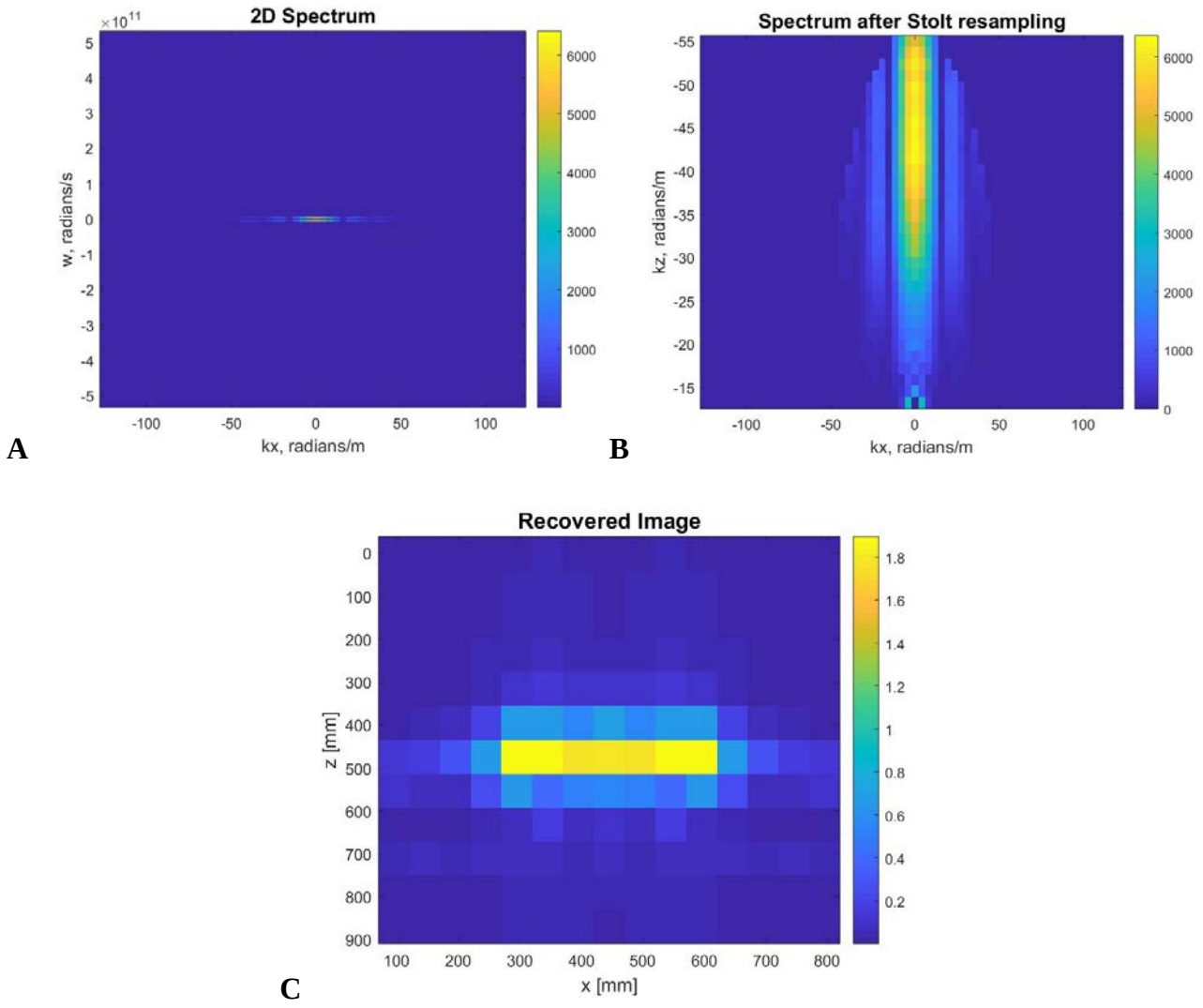

Figure 12: Stolt Migration Algorithm. (A) 2D spectrum. (B) Spectrum after Stolt resampling. (C) Image of slab recovered using Stolt migration.

The next step was to verify 3D Stolt migration processing. To this end, gprMax was used to develop synthetic data corresponding to a C scan over an area in which two metal pipes arranged in a cross shape were buried at known depths in a homogeneous soil layer. This scenario is similar to one of the controlled experiments described in Chapter III where two metal pipes were buried in a uniform sand soil and in a uniform Yahola soil. In the simulation, one pipe was about 17" in length and about 2" in diameter (50 mm), while the other pipe was about 4" in length and of the same diameter. The long pipe was laid on top of the short pipe with both centered in the x-y plane to form a cross shape, where the axis of the longer pipe was located at 45 degrees with respect to the x-axis. The z dimension center of the long pipe was located at a depth of 0.735 m, while the depth of the short pipe was 0.785 m. Both pipes were assumed to be perfect electrical conductors (infinite conductivity) and were hollow with a pipe thickness of 5 mm. The surrounding soil had a relative permittivity of 2.5 and a conductivity of 0.001 S/m. The image slices recovered by the 3D Stolt migration processing at various depths for a 500 MHz Tx are shown in Figure 13. As shown, the processing is able to locate the longer pipe at nearly the correct depth. The shorter, bottom pipe is not as clearly visible since it only extends 1" on either side of the longer, top pipe. However, there is increased signal (brightness) near the center of the image, which is likely due to the intersection of the two pipes at the center. Note that 2D Stolt migration processing is readily extended to 3D processing by replacing the 2D FFT operations described previously with 3D FFT operations, and modifying Equation 13 to include the wavenumber in the y dimension, k_y as follows

$$k_z = \sqrt{\left(\frac{w}{v_s/2}\right)^2 - {k_x}^2 - {k_y}^2}$$

(14)

The above exercises verify that Stolt migration can be used to process field data to develop subsurface images once prior post processing has developed an estimate of the scattered signal.

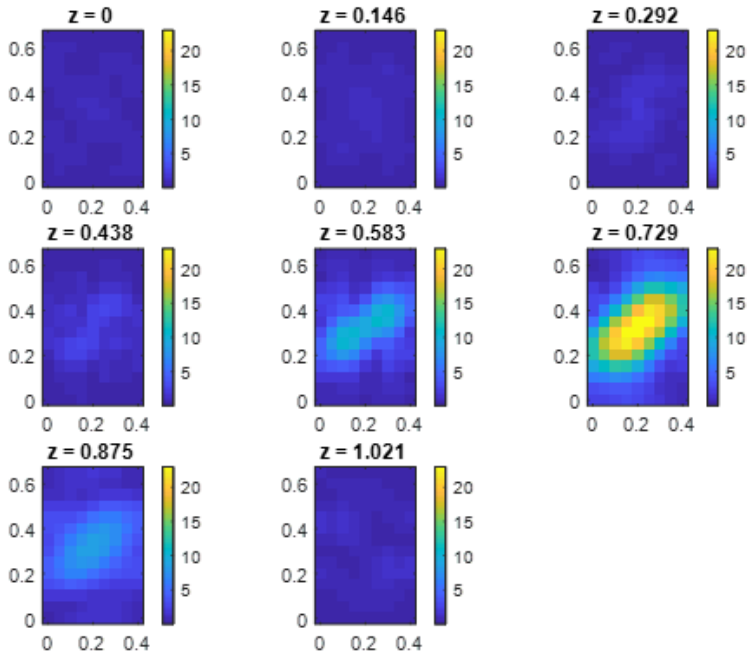

Figure 13: 3D image recovery of slab using 3D version of Stolt migration algorithm.

2.4 Analysis: Spatial Spectral Content (Spatial Bandwidth)

Finally, an analysis was conducted to determine if the spatial spectral content of a GPR image could be used to differentiate plants with fibrous roots from plants with tap roots. Note herein that the spatial spectral content of an image was quantified by determining what we refer to as the spatial bandwidth (SBW). As mentioned in section 1.2.4, two measures of SBW are determined corresponding to the bandwidth that encompasses 90% and 95% of the total spectral power. In this analysis, two images were generated to represent highly idealized tap and fibrous roots. Figure 14A shows the idealized tap root as a vertical rectangle extending downward from the surface. Figure 14C shows the idealized fibrous root represented as a sphere. Note, in an actual field trial, these two images would be the result of running the GPR data collected in a B-scan through the basic post processing schemes and the Stolt migration algorithm. The next step was to generate the spectral content of the two images, which is accomplished by applying a 2D FFT to both images to generate Figures 14B and 14D, respectively. It is apparent by looking at the spectral content plots, that the spectrum of the circle appears to be much more concentrated about the zero-center point ($k_x = k_z = 0$), whereas the vertical rectangle is more spread out especially along the $k_z = 0$ line. However, the images that will be developed from data collected from the field and processed through the Stolt migration algorithm will typically not be this distinctly different. That is why a technique which quantifies the spectral content of a given image is needed. To that end, code was developed which calculates the fraction of total spectral power within $+-k_x$ and $+-k_z$ of the zero-center point. The power is calculated in ever increasing squares about the zero point and then a curve is drawn based upon these points. Note that the power of a given spectral component is normalized and is equal to its magnitude squared divided by the total spectral power.

In this example, each of the original images are 32 x 32 (N_z x N_x) pixels with total image spatial widths, L_x and L_z both set to 1 m. The resulting step size in x and z = delx and delz = 1/32 = 0.0313 m. This implies that the spatial sampling frequencies, k_{xs}, k_{zs} = 32 cycles/m since k_{xs} = 1/delx and k_{zs} = 1/delz. The Nyquist frequencies, equal to half of the sampling frequencies are thus, both = 16. The resulting centered spectrum for k_x and k_z ranges from -16 to +15 with a spacing $delk_x$ = 1/Lx = 1 and $delk_y$ = 1/L_z = 1. This range is what is shown in each of the spectral content figures below for the circle and vertical rectangle. It is worth noting that k_x and k_z in the prior Stolt migration discussion were in units of radians/m (wavenumber), whereas k_x and k_z in this discussion are in units of cycles/m (spatial frequency). The conversion from spatial frequency in cycles/m to wavenumber in radians/m is achieved by multiplying by 2π radians/cycle.

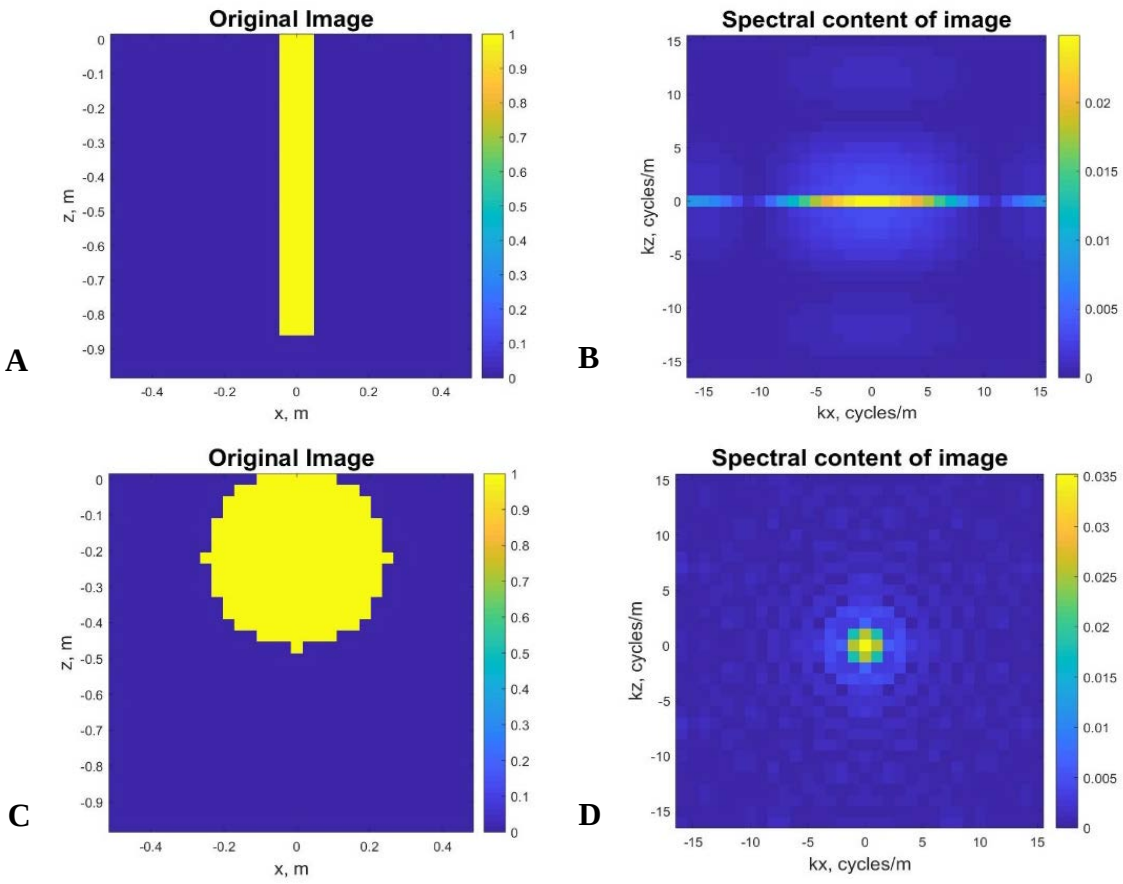

Figure 14: Development of quantitative comparison of spatial bandwidths. (A) Original image of ideal tap root. (B) Spectral content of idealized tap root. (C) Original image of ideal fibrous root. (D) Spectral content of idealized fibrous root.

Figure 15 shows the fraction of spectral power as a function of k_x, k_z where k_x and k_z are varied from 1 to 15 in steps of 1 for both images. For example, the first data point for each spectral image is determined by calculating the sum of the power of the spectral components within the square bounded by +-1 in k_x and +-1 in k_z, which amounts to the center 3x3 pixels since the zero point is included. The next data point corresponds to the sum of the power of the spectral components bounded by +-2 in k_x and +-2 in k_z, which corresponds to the center 5x5 pixels and so on up to +-15 in k_x, +-15 in k_z. To normalize the comparison two points of interest were

selected: (1) the spatial frequency at which 90% of the power is captured and (2) the spatial frequency at which 95% of the power is captured. The 90% points are shown in the figure below where the circle is shown to reach this value at 3.1 cycles/m, while the rectangle does so at 6.9 cycles/m. This clearly shows that the rectangle extends over a much wider bandwidth than the circle as was expected. Thus, in this ideal situation, there is a significant quantitative difference between the spectral content of an idealized tap root versus that of an idealized fibrous root. The 95% points were determined via interpolation to be 6.8 and 12.7 cycles/m, respectively for the circle and rectangle.

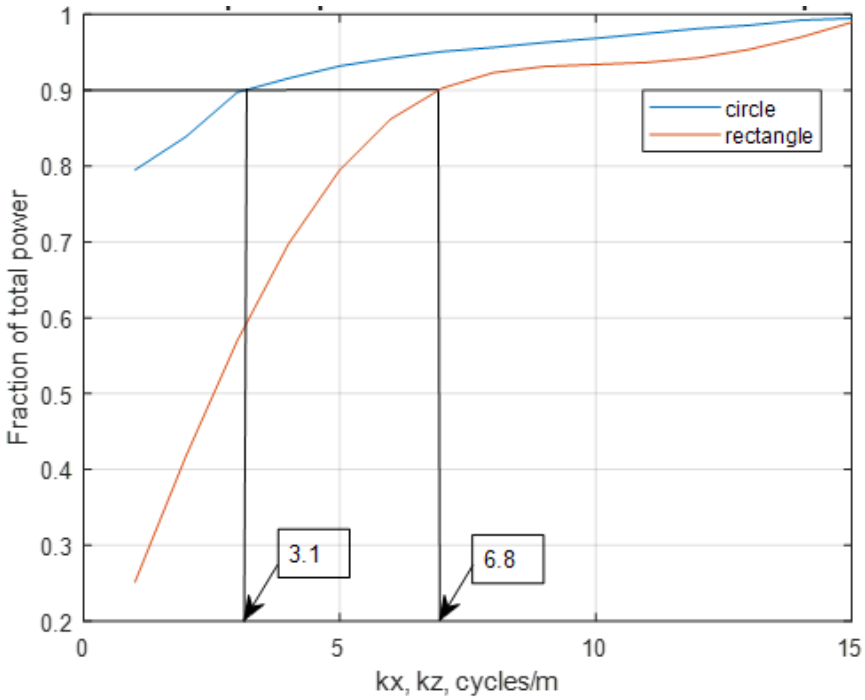

Figure 15: Comparison of fraction of spectral power within $\pm k_x$ & $\pm k_z$ from the zero point of idealized tap (rectangle) and fibrous root (circle).

The SBW analysis was extended to 3D by comparing the bandwidth of 3D models of a sphere and a parallelepiped. A 3D representation of the sub-surface would provide more accurate results by capturing data associated with the growth of the different root types in multiple directions. Similar to the comparison of the circle and rectangle, a sphere and parallelepiped, representing fibrous roots and a tap root respectively, were constructed in a MATLAB script. The same type of calculations were implemented to calculate the fraction of the total power. However, instead of calculating the power in ever increasing squares as in the 2D example, the power is calculated in cubes of increasing size expanding around the zero point in $+-k_x$, $+-k_z$ and now including $+-k_y$. Figure 16 shows the fraction of spectral power as a function of k_x, k_y, and k_z, where the latter are varied from 1 to 15 in steps of 1 for both objects. As shown the SBW of the idealized tap root (parallelepiped) is much greater than that of the idealized fibrous root (sphere), where at the 90% fractional power point the former is 12.49 cycles/m, while the latter is 4.61 cycles/m. The respective values for the 95% points are 14.25 and 8.69.

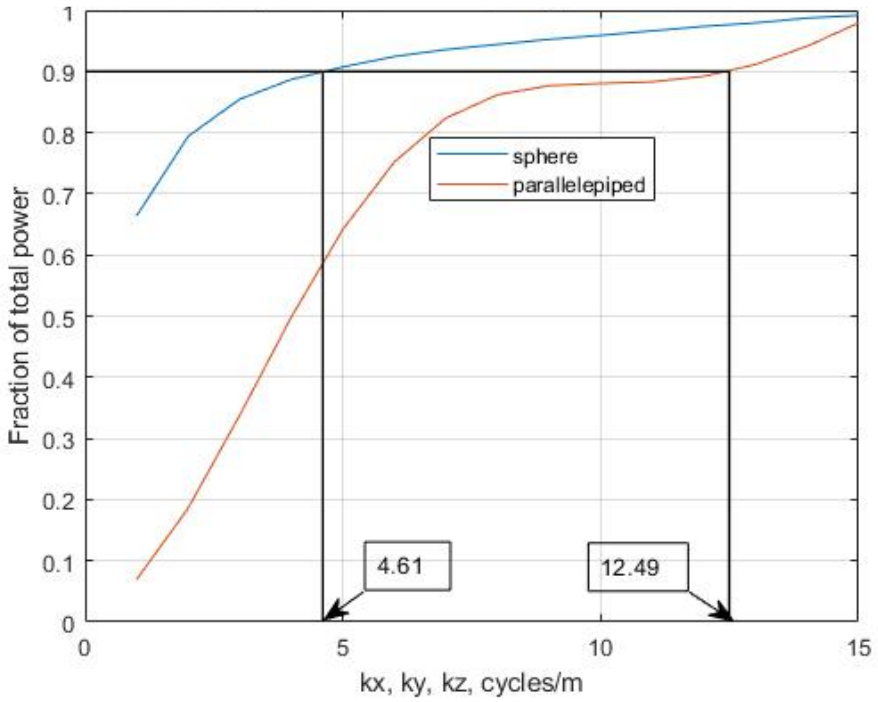

Figure 16: Comparison of fraction of spectral power within $\pm k_x$, $\pm k_y$ & $\pm k_z$ from the zero point of 3D idealized tap (parallelepiped) and fibrous root (sphere).

2.5 Summary

In this chapter three different computer models were run using an electromagnetic wave simulator, gprMax, along with MATLAB code to test the validity of using GPR in field root phenotyping applications. The three analyses conducted were: (1) an energy analysis comparing plant and non-plant locations using gprMax synthetic data, (2) the verification of the Stolt migration algorithm also using synthetic gprMax data, and (3) a spatial spectral content analysis comparing the SBW of plants with tap and fibrous roots in both 2D and 3D utilizing MATLAB code. In the first simulation multiple models were constructed to represent a root with varying characteristics along with a background model, called ExRef, to represent a homogenous soil

surrounding the root. In this simulation it was found that in ideal conditions, it is possible to differentiate between plant and non-plant locations based on the comparison of energy calculations associated with a GPR trace. Additionally, it was found that as the root parameters increased, most notably root diameter and RWC, the energy of the signal increased as well. The second analysis dealt with testing the applicability of using the Stolt migration algorithm. In conjunction with the simulations, multiple controlled and field experiments were conducted using a unique GPR configuration termed perpendicular common offset. This type of configuration is not typically used in GPR applications and needed to be tested in a simulated setting to assess if it was a viable signal processing tool to aide in root detection and differentiation. An image of a slab with differing electrical characteristics than the surrounding half space was run through gprMax using the perpendicular common offset configuration to generate raw synthetic GPR data that was then run through an open source script of the Stolt migration algorithm. A recovered image was then generated and compared to the original image. The comparison proved the functionality of GPR in this application while using the different configuration technique. The final analysis dealt with comparing the SBW of an idealized tap root image to the SBW of a fibrous root image. The SBW that encapsulated 90% and 95% of the total SBW was calculated and this value was compared between the tap and fibrous root. This was done in both 2D and 3D. It was found that in both cases, 2D and 3D, the SBW of the tap root was larger than the SBW of the fibrous showing that this method could potentially be used a tool for differentiating between different rooting systems.

CHAPTER III

CONTROLLED EXPERIMENTS

3.1 Introduction

The most common techniques for root phenotyping take place in greenhouse or laboratory settings. In both cases plants are often grown in small pots or in gel media. Both of these scenarios limit or completely remove the influence of soil on a rooting system which makes field techniques desirable in order to capture the influence of the soil on a growing rooting structure. However, conventional field methods are often time consuming and labor intensive. Newer technologies, such as magnetic resonance imaging and the use of unmanned aerial vehicles, are still under development and have their own set of drawbacks. GPR has been proven to be a viable tool for root phenotyping particularly when investigating larger roots such as tree roots and is an attractive option due to its rapid data collection and non-destructive nature. In Chapter II it was seen that in the ideal conditions, of the simulations that GPR is a viable tool to detect the presence or absence of roots based on an energy analysis. Also, that GPR can distinguish between tap and fibrous roots by comparing the SBW between the two. The next step was to validate these results but in environments closer to field conditions and attempt to capture the influence of changing soil characteristics on the GPR signal. One of the most important characteristics that influences GPR's ability to detect subsurface anomalies is contrasts in relative permittivity which is a function of changing soil water content. To monitor this soil electrical data was collected alongside the GPR data. Measurements were taken on two types of plants: sorghum (fibrous) and cotton (tap). This was done across multiple small-scale controlled boxes in both a sand and a Yahola very fine sandy loam soil type. Multiple soil monitoring

devices were used to measure the soil's electrical characteristics in an attempt to integrate the influence of changing soil conditions on a GPR signal in both 2D and 3D analysis. The objective of this chapter was to assess the potential for GPR to detect root biomass and structure by incorporating soil electromagnetic properties in controlled experiments.

3.2 Methods

Fourteen PVC 1 m^3 boxes were constructed and lined with plastic bags and then placed approximately two meters apart in an unused field at the Texas A&M Farm. The boxes were placed away from any water sources or areas known to accumulate standing water during rain events. Additionally, the boxes were placed away from any large trees or plants whose roots or overhanging branches could interact with a GPR signal. Seven of these boxes were filled with the Yahola very fine sandy loam (coarse-loamy, mixed, superactive, calcareous, thermic Udic Ustifluvents) soil series collected from the Texas A&M Farm. All textural classification data was obtained with Web Soil Survey. The Yahola soil was selected to mimic conditions of the field data being collected in conjunction with the controlled experiment. Additionally, the Yahola, as opposed to other soils present throughout the farm, has a lower clay content and therefore lower attenuation rates and higher expected signal returns. The other seven boxes were filled with a washed sand material purchased from a local bulk soil store. The sand was selected to represent ideal conditions for GPR signal propagation with low clay content, high water infiltration, and low water retention rates. One box of sand and one box of Yahola contained two pieces of aluminum pipe stacked one on top of the other to form a cross shape in the x-y plane with the top of the top-most pipe at a depth of about 0.67 m in the box of sand and a depth of about 0.56 m in the box of Yahola. These boxes were used as a control to test the functionality of different signal processing and imaging techniques. The contents of each box are described in Figure 17C, while

Figure 17A and 17B shows a graphic representation of a single box and a picture of one of the boxes in the field.

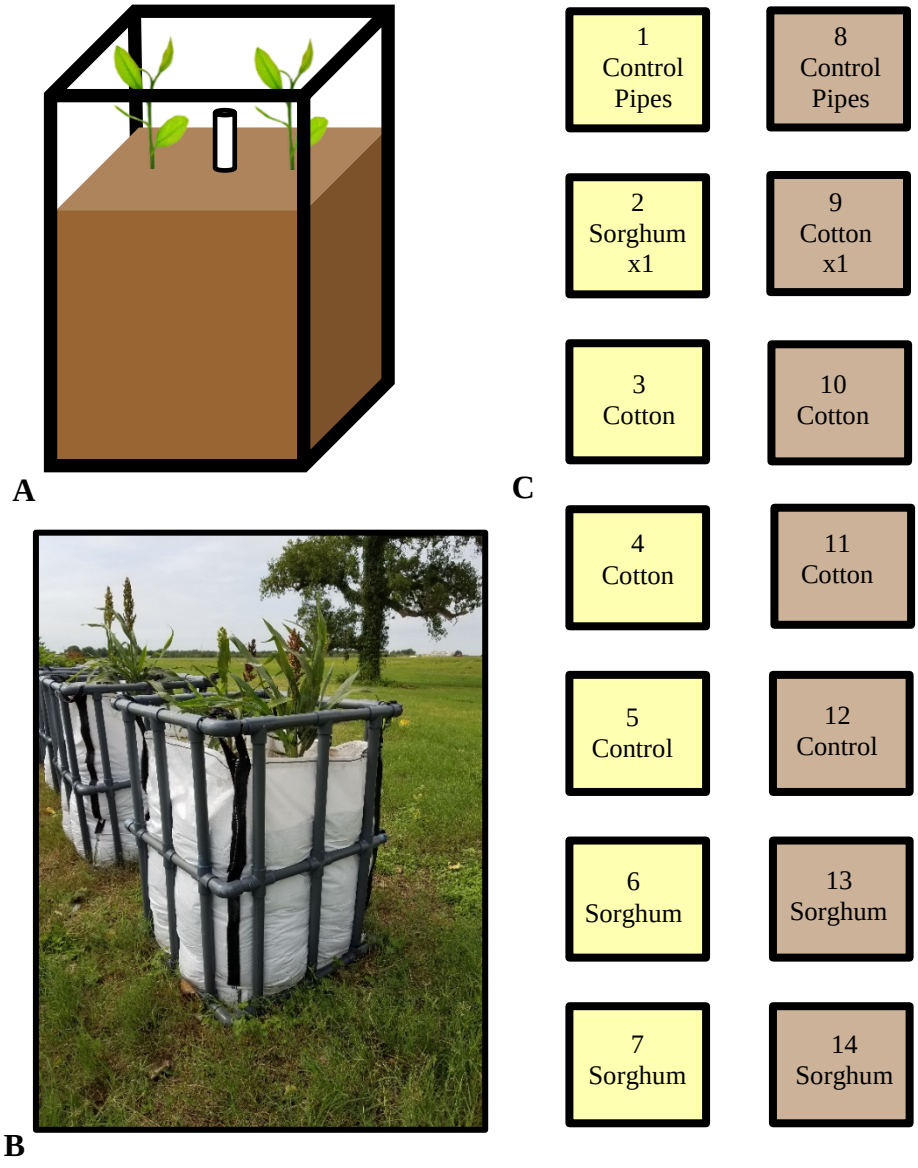

Figure 17: Box experiment design. (A) Contents of a single box. (B) Picture of box containing sorghum. (C) Contents of the 14 different boxes. Sand in yellow boxes and Yahola in brown.

Two of the boxes, 5 and 12, labeled control in Figure 18B only contained an access tube for NMM readings. The reason behind this was that the two boxes could potentially serve as an estimation of the background signal. GPR data collected from box 5 could be used to develop an estimate of the background signal for sand, while data collected from box 12 could be used to develop a background signal estimate for Yahola. These respective background signals could later be removed from the GPR data collected from the boxes with plants to help visualize the roots only, serving as a semi-perfect background removal, similar to the ExRef trace in the simulations. However, when this method was tested, it did not yield meaningful results due to the inability to properly synchronize the data and variability of the soil conditions between the control boxes and the boxes with plants. This variability could be due to a number of factors. First, a main issue with the boxes overall was keeping the soil within each box level across the entire area and over time. This was difficult since the bags which the soil was placed in, were not rigid and allowed for slight settling and movement of the soil over time. Also, the 2018 season was uncharacteristically wet with multiple heavy rain events. These rain events had a tendency to move the soil around in the boxes and pool in corners and along edges. This movement of soil resulted in small differences in terrain between boxes and over time. Another reason the box background subtraction did not work was due to the changes in gain compensation between boxes due to variations in water contents between the boxes. Even minor differences in conductivity between the boxes could alter the amount of gain applied and subtracting a uniform background from all the boxes failed to capture the differences in conductivity resulting in skewed results. Thus, for all of the processing conducted herein, background signal estimates were derived from the collected signal as described in section 1.3.1.

Originally, cotton and corn were selected to represent the two different root architectures: tap and fibrous. A tap root architecture consists of a primary central root that is larger in diameter than all other exploratory lateral roots. This type of root generally penetrates deeper into the soil but with minimal lateral spread of roots. On the other hand, a fibrous rooting system is made up of many thin roots that typically spread extensively through the topsoil but do not penetrate to lower depths (Atkinson et al., 2014). Both the corn and the cotton were transplanted from nearby fields as immature plants. The same fields were later used in the field experiments. Corn was initially selected to represent the fibrous root system, however, the corn did not survive the transplant process and had to be replaced after the second set of data collection. At that point in the season, the corn growing in the field was too large to be transplanted, and so instead a late season sorghum, which also has fibrous roots, was transplanted from a site within the farm on similar soil. The sorghum remained for the rest of the data collection time period. The transplanted cotton survived the entire season and did not need to be replaced at any point. The 2018 season was particularly wet and therefore the plants did not require a significant amount of supplemental water. At any point when the plants did require water, each box was hand watered approximately the same amount at the same time. No chemicals or fertilizers were added to boxes at any point during the experiment to limit the influence of any outside factors on the GPR signal. Although the sand was selected for its much lower attenuation of GPR signals, it is not an ideal soil type for plant growth. Thus, the crops in the sand boxes were stunted and did not grow to the extent that the boxes containing the Yahola soil. Figure 18 shows a comparison between a cotton and sorghum plant in Yahola soil boxes versus a cotton and sorghum plant in sand boxes.

A  B 

C  D 

Figure 18: Typical contents of different boxes. (A) Cotton Yahola. (B) Sorghum Yahola. (C) Cotton sand. (D) Sorghum sand.

It is clear that the plants in the Yahola soil boxes were consistently larger throughout the growing season, and therefore any comparisons made between boxes of different soil types must be done with caution because the size of the rooting systems could potentially be vastly different. The GPR selected for this objective was initially a 500 MHz and then later a 1000 MHz Sensors & Software bistatic unit (Sensors & Software, Mississauga, Ontario, Canada), where the term bistatic implies that the Tx transducer is separate and distinct from the Rx transducer. A typical GPR transect is run in what is called a common offset configuration with the transmitting and receiving antenna placed at a fixed distance apart and offset in the direction of travel. In many

cases, the distance between the two antennas is made as small as possible with the limit typically being the respective enclosure dimensions. However, for this controlled experiment (and the field experiment described in Chapter IV), a bistatic unit was chosen to allow for the transmitter and receiver to be on opposite sides of the growing plants in a modified common offset configuration with the offset being perpendicular to the direction of travel. This configuration, which we have termed perpendicular common offset, was chosen to increase the likelihood of root visualization. Figures 19A and19B illustrate the two different types of GPR data collection configurations, and Figure 19C is a picture of the common offset perpendicular orientation setup in one of the boxes.

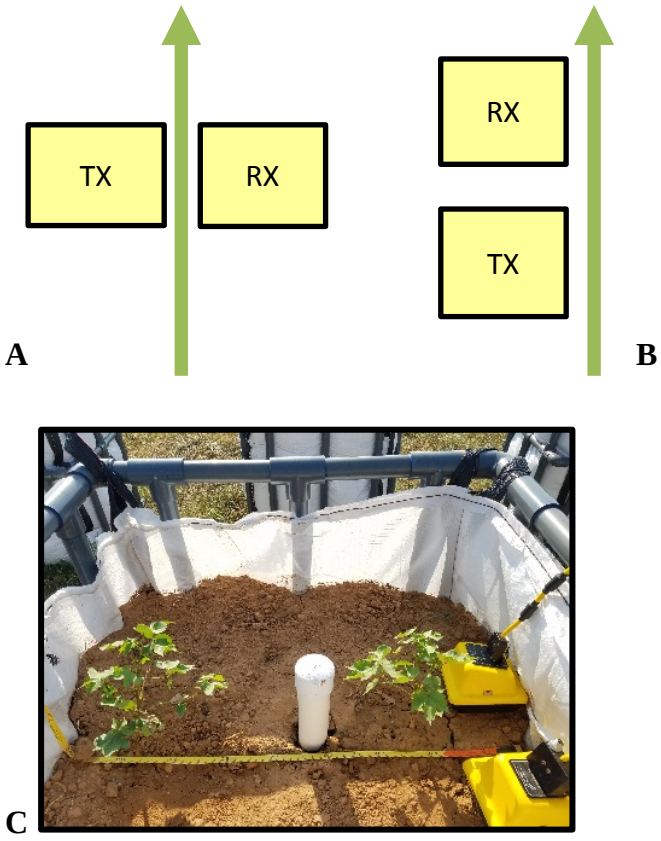

Figure 19: Different data collection configurations. (A) Perpendicular common offset. (B) Common offset. (C) Picture of perpendicular common offset configuration in box.

Note that the conventional common offset configuration was used in the SOC work described in Chapter V since the intent was to measure SOC content in the first 15 cm of soil and not root structures (and there were no intervening plants at the time of the measurements). The common offset configuration is much more efficient from a data collection perspective since mobile, wheeled assemblies, which carry the transducers are commercially available, while the common offset perpendicular configuration required manual movement of each transducer in lieu of a mobile, mechanical assembly which was not available.

The 500 and 1000 MHz center frequencies were selected because the rooting system of both plant types remain in the top portion of the soil profile, therefore the pulse does not need to penetrate as deeply as in other scenarios, but due to the small size of the roots, requires a better resolution. Resolution for GPR applications is typically defined as the minimum distance at which two electrically small scattering objects can be distinguished from one another. Per Persico (2014), the achievable horizontal and vertical resolution are both proportional to the wavelength of the EM wave in the soil, which is inversely proportional to the center frequency, and thus, the higher the frequency the better the resolution. A GPR transect was run parallel to the crop row with the Tx on one side of the plant and the Rx on the other. Additionally, prior to any planting or installation of monitoring devices, all boxes were scanned with both sets of transducers during dry and wet conditions to obtain an estimate of the background signal for each box. These background signal estimates were in addition to the estimates derived from the control boxes described earlier in this section. Using these pre-stored background signals from each of the boxes had some of the same problems as experienced in using background signals from the control boxes. In addition, changes in soil properties between when the actual data was collected and when the background signal was recorded result in additional distortion of the estimated scattered signal, thus, reinforcing the decision to use background signal estimates derived from the collected signal as described in section 1.3.1. Each box was scanned four times with four different antenna orientations. The first with both Tx and Rx antenna polarizations oriented perpendicular to the direction of travel, and the second with the antennas oriented parallel to the direction of travel. The third orientation consisted of the Tx antenna being perpendicular to the direction of travel and the Rx antenna being parallel. The final orientation was the opposite of the third with the Tx oriented parallel and the Rx perpendicular to the

direction of travel. Figure 20 shows the four antenna orientations, which we have labeled as perpendicular-perpendicular, parallel-parallel, perpendicular-parallel, and parallel-perpendicular.

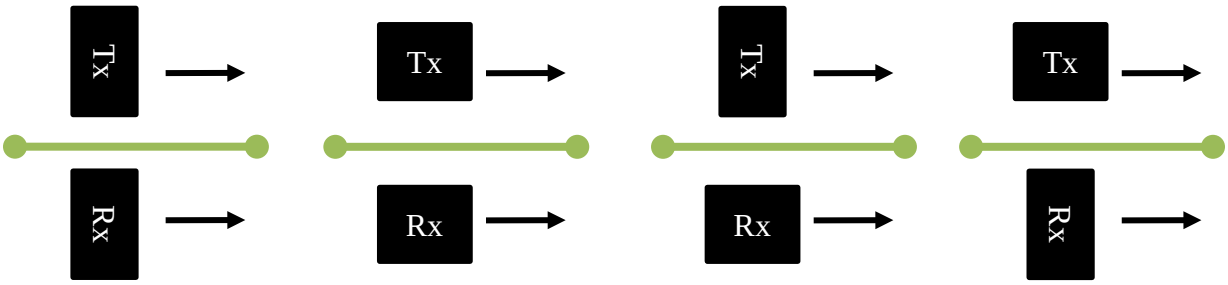

Figure 20: Four different antenna orientations. Perpendicular-perpendicular, parallel-parallel, perpendicular-parallel and parallel-perpendicular.

A trace was collected every 2.5 or 5 cm with the starting and ending positions of each transect noted for each box so as to maintain consistency in transect location and length between different survey dates. Additionally, in boxes 1, 2, 8, and 9 multiple B-scans at 5 cm increments were run in the typical common offset configugration, as shown in Figure 19B, to generate a C-scan of each of the four boxes. For boxes 1 and 8 which each contained the two buried metal pipes the distance between B-scans was uniform over each box. But for boxes 2 and 9, which each contained a plant, there was one step size between B-scans that was much greater than all of the other step sizes. This greater step size was required to avoid the intervening plant.

Since a GPR signal is strongly influenced by soil volumetric water content, θ_w, due to water's influence on dielectric properties, it is critical to monitor soil moisture readings in each box at the time GPR readings are collected. Three techniques based upon three separate devices

were selected to monitor soil moisture content in conjunction with the GPR measurements. The three devices selected were an electromagnetic induction (EMI) unit, a neutron probe for incremental point depth measurements, and a theta probe for point surface measurements as shown in Figure 21 A, B and C respectively.

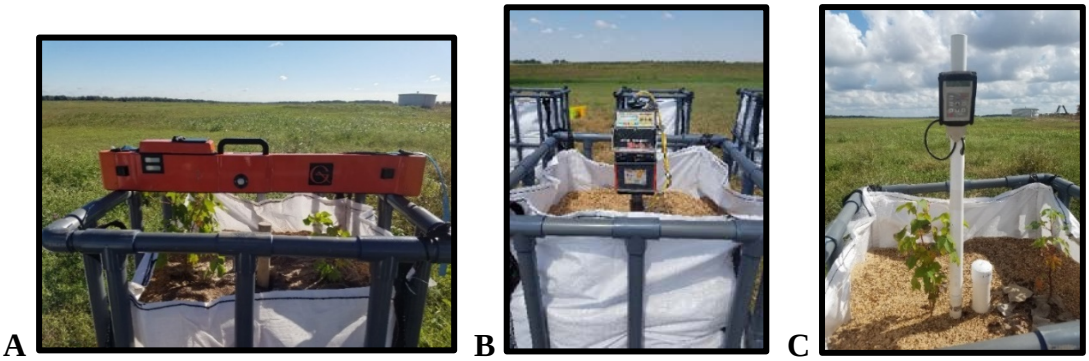

Figure 21: Devices used to measure ancillary soil electromagnetic properties. (A) EM-38MK2. (B) Neutron Moisture Meter. (C) Theta Probe.

The EMI meter selected was the EM-38MK2 (Geonics Limited, Mississauga, Ontario, Canada). Electromagnetic induction meters have been used extensively in agricultural settings as a tool to quickly and nondestructively map soil properties including clay content and soil moisture. EMI meters measure the bulk apparent electrical conductivity of a soil (EC_a) which is driven by the presence of electrolytic solutions in the moisture filled pores and passages in the soil (McNeill, 1980). EMI meters contain a transmitter coil that generates a primary magnetic field which travels through the soil via eddy currents. These eddy currents interact with the

moisture filled areas within the soil and generate a secondary magnetic field which is proportional to the EC_a of the soil (Doolittle et al., 2001 & 2014; McNeill, 1980,). The EM-38MK2 was used to collect bulk apparent electrical conductivity reading in each box. The EM-38MK2 provides two measurements based on readings from different coil spacings between the transmitter and receiver. The first reading corresponds to a spacing of 0.5m and the second to a spacing of 1.0m. Multiple readings allowed for a multilayered representation of the soil in later post processing. The EM-38MK2 was placed on top of each box as shown in Figure 21A and five measurements were manually taken and then averaged for a final value at each coil spacing. Prior to data collection the EM-38MK2 was calibrated in both the vertical and horizontal dipoles. The weather and temperature conditions were also noted to temperature calibrate the EC_a values after collecting the data. The EM-38MK2 measurements taken on 8/24/18 verified that sand has a lower expected attenuation than Yahola soil where the average ECa value for the 0.5 m spacing for the sand boxes was found to be 1.93 mS/m, while the average for the Yahola boxes was 3.20 mS/m. Given the near linear relationship between the conductivity and the attenuation coefficient alpha (see Equation 7), Yahola was expected to have an alpha that is about 1.66 times greater than that of sand. This translates into a signal that is about 3.5 times less over 1 m in Yahola soil compared to sand due to the negative exponential signal decay relationship with alpha, see Equation 8 and 9.

The neutron probe selected was a 503 Elite Hydroprobe (CPN, Concord, California, USA). Neutron moisture meters (NMM) are the gold standard of measuring soil moisture in the field (Schmugge et al., 1980; Stone et al., 1955). Field calibrated NMM are widely accepted as an indirect moisture monitoring device and are known to be the most accurate and reliable machine for soil moisture measurements in agricultural settings (Evett, 2008). A neutron

moisture meter consists of a radioactive source, in this case Americium-241, which emits fast, high energy neutrons. After the probe is lowered into the ground, neutrons are emitted and begin to collide with atoms in the surrounding environment and are then slowed, also known as becoming thermalized (Chanasyk et al., 1996). The neutron moisture detector is designed to count these slow neutrons while ignoring the fast neutrons (Grant, 1975). The typical atom that the fast neutrons collide with are hydrogen atoms, due to hydrogen's low atomic weight. In soil, since the main source of hydrogen is water, the proportion of slow neutrons counted by the device is equivalent to volumetric water content (Schmugge et al., 1980).

After initial GPR scanning, an aluminum access tube was installed and NMM moisture readings were taken at a depth of 10, 20 and 40 cm in 10 of the boxes (boxes 3, 4, 5, 6, 7, containing sand and boxes 10, 11, 12, 13, 14 containing Yahola. Prior to each use of the NMM a standard count had to be performed to check the accuracy and calibration of the machine. In addition, a calibration curve had to be developed for each soil type under observation by comparing NMM measurements to lab tested soil volumetric water contents. Three calibration curves were used to account for the different soil types, Weswood (found in the field experiments see Chapter III), Yahola and the sand mixture with a RMSD, or root mean square difference, for each linear relationship being 0.0232, 0.0114, and 0.016 respectively. The ideal condition for a NMM to take the most accurate readings is with an aluminum access tube, however, the presence of a metal pipe had the potential to greatly disrupt the GPR signal and block out the portion of the signal representing roots. Therefore, during each GPR scanning the tube was removed and replaced with a dry wooden dowel to minimize the impact. Additionally, the NMM access tube needed to be placed in the center of the box to obtain a more accurate reading of the soil within the box. This was done to reduce outside influences and for safety

reasons to minimize neutron exposure to the operator. Similar to the multi-layered approach of the conductivity readings, the NMM readings were used in the GPR post processing of the signal. The different depth readings of soil volumetric water allowed for more accurate calculations of relative permittivity and signal velocity throughout the soil profile within each box. These more accurate representations allowed for more precise post processing schemes to be used. Table 2 lists some of the NMM data collected on survey date 7/26/18 and shows how the water content varied not only between soil types but with depth. Two sets of boxes (1, 2, 8, and 9) did not have access tubes installed and NMM measurements were not taken. Access tubes were not installed in 1 and 8 because they contained the buried pipes and were used as a control. Box 2 contained a single sorghum plant, while box 9 contained a single cotton plant. All of these four boxes were intended to be used to in the construction of C-scans.

Table 2: List of volumetric water contents collected using neutron moisture meter on 7/26/18.

Volumetric Water Content m^3 m^{-3} of Boxes			
Box	10 cm	20 cm	40 cm
3 Sand	.07	.05	.06
4 Sand	.08	.07	.08
5 Sand	.07	.05	.07
6 Sand	.09	.07	.09
7 Sand	.07	.06	.07
10 Yahola	.11	.19	.19
11 Yahola	.10	.19	.21
12 Yahola	.10	.22	.23
13 Yahola	.13	.23	.23
14 Yahola	.14	.24	.25

The final device used to monitor soil moisture was a TH20 Theta Probe (Dynamax, Houston, Texas, USA) which analyzes the impedance of a soil. The Theta Probe is a hand-held device with approximately 10 cm long pins that are inserted into the ground and generate a 100 MHz sinusoidal signal (Gaskin et al., 2006). The signal impedance is measured as a voltage output which is primarily controlled by the relative permittivity and conductivity of the soil (Robinson et al., 1999). As stated earlier, the relative dielectric permittivity is primarily controlled by the soil volumetric water content, therefore the voltage output of the Theta Probe can be related back to soil volumetric water content. Similar to the NMM, the theta probe must be calibrated to the specific soil type. To do this, 5 readings were taken at a single location and then a soil sample of known volume was collected from the measurement location. A wet and dry weight were taken of the sample and gravimetric water content and bulk density were determined to calculate volumetric water content. This was done 5 times in each soil to create a calibration for the theta probe. At the time of each survey four Theta Probe measurements were taken at four different positions within the box and then averaged for a final surface volumetric soil measurement. The surface soil measurements taken with the Theta Probe were combined with the multiple measurements taken with the NMM to create a more representative picture of the electrical properties of the soil profile within each box and help account for how they change with depth.

In the MATLAB code implementation of the GPR signal processing the user can select from several options for calculating the soil conductivity. These options include (1) EM-38, (2) McCutcheon, (3) Noborio, (4) manual. The EM-38 option uses the two EM-38 readings directly, σ = soil EC_a, where the reading corresponding to 0.5 m spacing is used for depths < 0.75 m, while interpolated values based upon both readings are used for depths > 0.75 m. For the

McCutcheon and Noborio options, the θ_w values measured by either the NMM or theta probe are used in Equation 15 or 16 below to determine soil conductivity. Equation 15 was derived by McCutcheon et al. 2006 and is representative of conductivity in sandier soils. Equation 16 was derived by Noborio et al. in 1994 and is representative of loamy soils. Finally, the manual option allows the user to set the soil conductivity value directly.

$$\sigma = 4.504e^{8.2635\theta_w} \qquad \text{(McCutcheon)} \tag{15}$$

$$\sigma = \sigma_w\theta_w(a\theta_w + b) + \sigma_s \qquad \text{(Noborio)} \tag{16}$$

Note that in Equation 16, σ_w is the conductivity of soil solution = 0.3 S/m, σ_s is the conductivity of dry soil = 0.002 S/m, a = 2.635, and b = 0.09184, where the values are representative of a sandy loam soil as would be found in College Station, TX.

The estimated conductivity values were applied in the gain compensation step within the GPR signal processing, see section 1.3.1. The gain calculations are related to the attenuation rate of the soil media, which is strongly influenced by soil electrical properties, primarily conductivity and relative permittivity. Collecting multiple readings of EC_a, along with soil θ_w, allowed for the construction of a multi-layered gain function, which compensates for the exponential loss of signal due to attenuation throughout the entire soil profile.

In addition, the multiple θ_w measurements collected by the NMM at depths of either 10, 20, and 40 cm for the controlled experiment, or at depths of 20, 40, and 60 cm for the field experiment (see Chapter IV), supports the development of a multi-layer relative permittivity

profile per Topp's equation. This in turn allows for a multi-layer soil wave velocity profile using the relation $v_s = \frac{c}{\sqrt{\varepsilon_r}}$. The processing code implementation for the soil wave velocity profile supports three options. Option 1 assumes one layer and is the default option if only one value of θ_w is available. Option 2 assumes three layers and can be used when the three NMM values are available. If the NMM measured depths are 10, 20, and 40 cm, the three layers are defined from 0 to 15 cm, 15 to 30 cm and 30 cm to the soil depth. If the measured depths are 20, 40, and 60 cm, the three layers are defined from 0 to 30 cm, 30 to 50 cm and 50 cm to the soil depth. Option 3 supports interpolation of the NMM values with an interpolation step size of 5 cm. Thus, there are 10 layers when the maximum measurement depth is 40 cm, and 14 layers when the maximum measurement depth is 60 cm, where the extra layer comes from extending the interpolation one step size past the maximum measurement depth. When NMM measurements were available, the three-layer option was typically used since there were recommendations in the Stolt migration software documentation to limit the number of layers when possible (Skjelvareid, 2012).

The analysis on the box data were performed in the same manner as in the simulations. For the energy analysis, to determine if our hypothesis that plant locations will have higher energy readings than non-plant locations, could be backed by statistically significant data, we conducted similar analysis for the GPR data collected in all of the boxes across multiple measurement dates (8/9/18, 8/24/18 and 9/19/18). The average or mean energy per trace (MEPT) was computed across plants of the same type and across all four antenna orientations for both plant and non-plant locations. In addition, for boxes with two plants, the non-plant EPT was calculated based upon the traces midway between the plants, whereas for boxes with one plant, it was the average of the two traces that are midway between the plant location and the ends of the

boxes. This approach for the non-plant EPT was used to minimize the interference due to reflections from the plants and is different from the way it was calculated in Figure 22 where all non-plant locations were averaged.

The second analysis compared the SBW of the images generated from the different crop soil combinations. The SBW was calculated by taking the average measurement of the representative boxes. For example, in the case of Yahola cotton, three boxes contained the combination, and thus, the reported SBW was the average of the SBW across all three boxes. For the case of Yahola sorghum there were only two boxes, and thus, the reported SBW was the average across the two boxes. In the sand scenario it was the opposite, with the results from three boxes of sorghum being averaged, while for cotton the results from two boxes were averaged. Comparisons were made between the SBW of sorghum and cotton across both soil types combined, within one soil type only, at single dates and over time.

3.3 Results

In this section, we discuss the results of the three analyses conducted on the GPR data collected in the controlled experiments. The three analyses include: (1) an energy analysis comparing plant and non-plant locations, (2) a spatial spectral content analysis comparing the SBW of plants with tap and fibrous roots, and (3) a 3D analysis based upon C scan data collected from selected boxes.

3.3.1 Energy Analysis

This analysis was used to verify the model simulations that plant locations have larger signal return than that of non-plant locations. As opposed to the simulations, where there was also a comparison between plant roots of various water content and diameter, the box and field

data focused on the more basic hypothesis that there are higher signal returns from traces associated with a plant location as opposed to those at a non-plant location.

Figure 22 is a representative result, which shows the energy per trace (EPT), in femto-Joules (fJ) for the scattered signal after background removal at each location along the entire transect across a box filled with sand and containing two cotton plants. Two traces were selected around each plant to better represent the spread of the roots beneath the surface and to account for the fact that not all plants were located exactly at a 5 cm interval. In this example, it is seen that the plant locations individually have higher energy levels than the surrounding non-plant locations in all but one non-plant location. The average energy per trace for the traces associated with plant locations was about 35 fJ, while the average energy per trace for the non-plant locations was about 16.5 fJ.

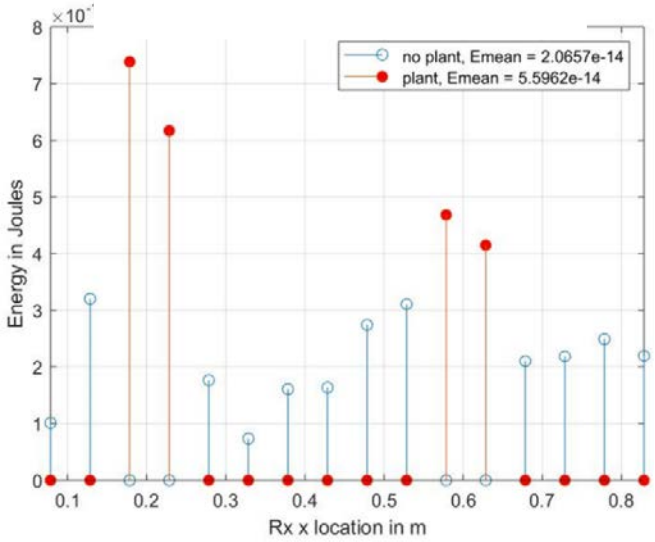

Figure 22: Representative energy comparison in box containing sand and cotton between non-plant (blue lines) and plant locations (red lines).

Figures 23A and 23B demonstrates the difference in MEPT between plant and non-plant locations across multiple dates for sorghum and cotton, respectively in the sand boxes. In all cases the mean at plant locations is above the mean at non-plant locations. The sorghum MEPT increases over time as one would expect, but the cotton does not. A possible reason for the latter is that the tap root structure of cotton is harder to detect than is the fibrous root structure of sorghum. The associated p-values for sorghum and cotton individually, and then sorghum and cotton taken together are shown in Table 3. The sorghum p-values meet the 0.05 confidence level for all dates, while cotton p-values met it for two of the three dates. The p-values were further reduced when the sorghum and cotton data was merged by virtue of the increased number of total sample points (56 total compared to 24 and 32 for sorghum and cotton, respectively).

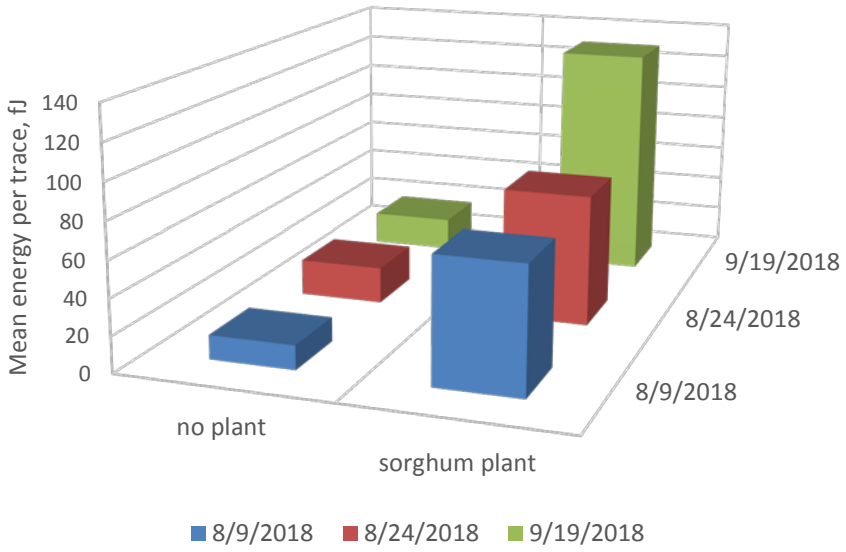

A

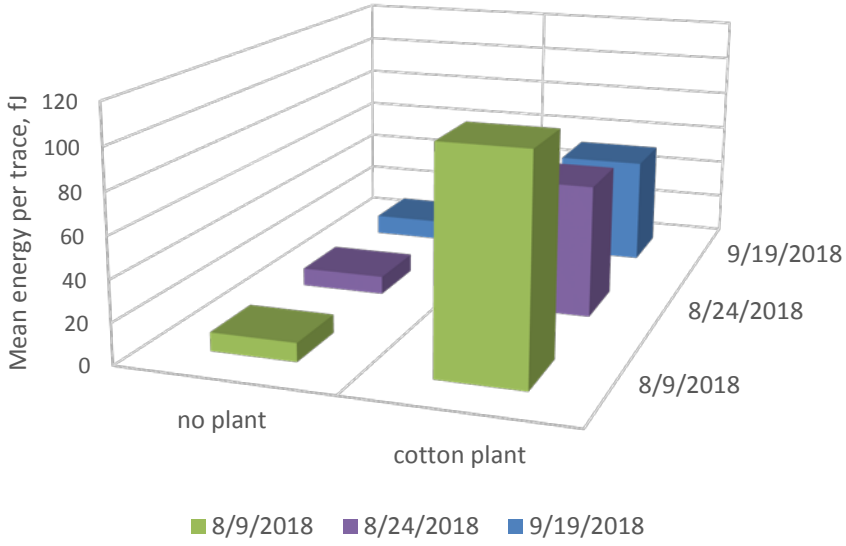

B

Figure 23: Energy analysis in box data. (A) Mean energy per trace for sorghum plants in sand boxes. (B) Mean energy per trace for cotton plants in sand boxes.

Table 3: P-values of comparison between plant and non-plant locations in sand box data.

P-values Sand Boxes			
	Sorghum	**Cotton**	**Combined**
8/9/2018	0.019	0.038	0.005
8/24/2018	0.045	0.035	0.006
9/19/2018	0.011	0.068	0.003

The above results for sand are based upon the application of a constant gain value of one, or that is to say no gain. This was a reasonable starting assumption due to the lower signal attenuation associated with EM wave propagation in sand. There is always concern when gain is applied that the gain estimates are inaccurate to that extent that the results might be worse than without gain applied. That turned out to be the case for sand, but for Yahola, gain was required to overcome its higher signal attenuation characteristics. The resulting MEPT values for Yahola soil with gain applied based upon an estimate of the attenuation coefficient, alpha are shown in Figures 24A & B, where we see that the MEPT of the plant locations did exceed the MEPT of the non-plant locations for all dates, although just barely for cotton on 8/24/18. The corresponding p-values are shown in Table 4, where we see the sorghum results when taken individually were significant on two of the three dates, while for cotton taken individually none of the results were significant, although the result for 8/9/18 was quite close. These results for the boxes show that as expected GPR tends to perform better in a lower attenuation medium such as sand as opposed to a higher attenuation medium such as Yahola soil. In addition, better results were obtained for sorghum as opposed to cotton, which may be due to the difference in root structure.

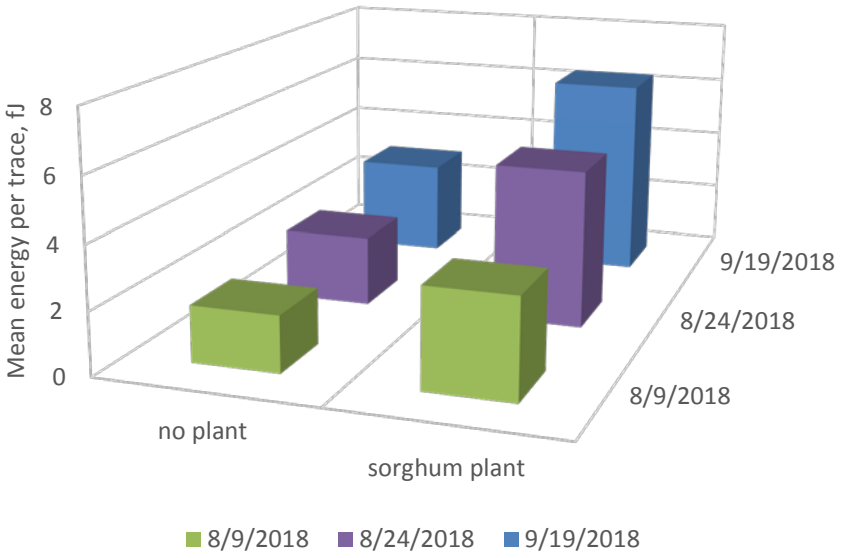

A

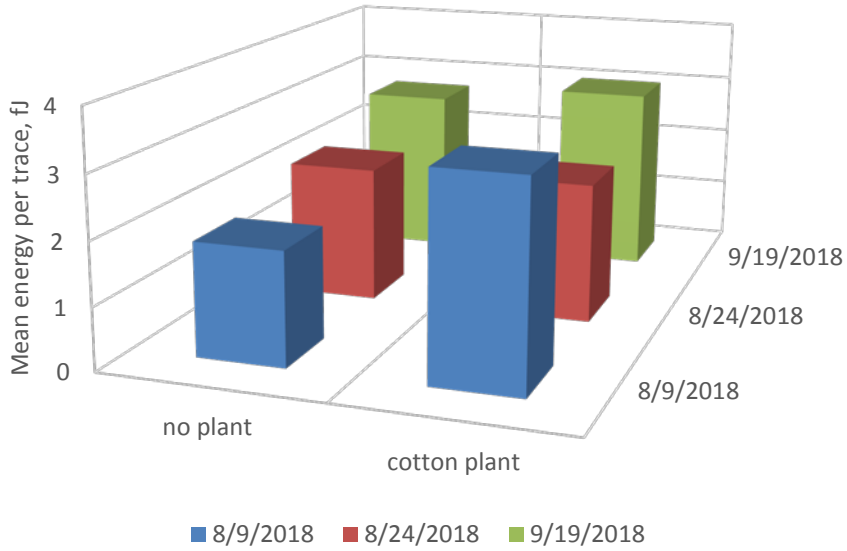

B

Figure 24: Energy analysis for box data. (A) Mean energy per trace for sorghum plants in Yahola boxes. (B) Mean energy per trace for cotton plants in Yahola boxes.

Table 4: P-values of comparison between plant and non-plant locations in Yahola box data**.**

P-values Yahola Boxes			
	Sorghum	**Cotton**	**Combined**
8/19/2018	0.04706	0.1276	0.01943
8/24/2018	0.03685	0.5676	0.109
9/19/2018	0.131	0.432	0.1311

3.3.2 Spatial Spectral Content Analysis (Spatial Bandwidth)

The spatial spectral content analysis was used to determine if the SBW of tap roots was greater than the SBW of fibrous roots based upon data collected in a number of controlled experiments. This analysis, which determines the SBW at the 90% and 95% power points, was initially discussed in sections 1.3.2 and 2.4. In the simulated scenario discussed in section 2.4, the SBW of the circle, representing the fibrous rooting mass, had a smaller SBW when compared to the SBW of the rectangle representing the tap root system. If the simulations findings hold true, then the SBW of the boxes containing cotton (tap root) will have a larger SBW as opposed to the boxes containing sorghum (fibrous root). Figures 25 A, B, C, and D are example spectral content plots for cotton and sorghum in sand and in Yahola. All of these spectral plots are based upon measurements taken on 8/24/18 with the Tx frequency = 1000 MHz, the Tx and Rx y polarized, and the transect along the x direction.

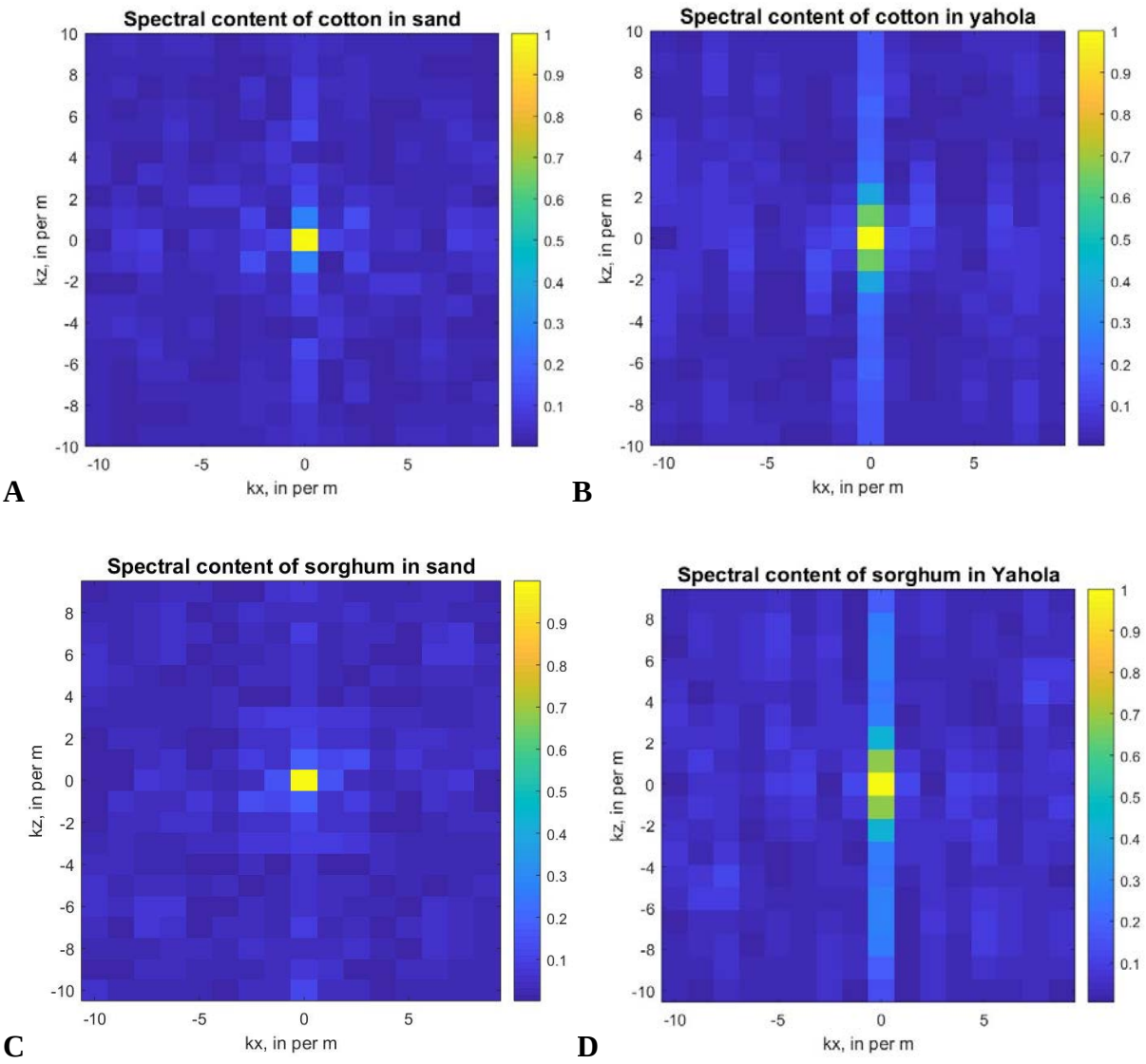

Figure 25: Spectral content images (A) Cotton in sand. (B) Cotton in Yahola. (C) Sorghum in sand. (D) Sorghum in Yahola.

As opposed to the simulation results where the difference in SBW was visually apparent, it is typically not possible to visually determine which image has a larger or smaller SBW. To quantify the comparison, we calculated the SBWs out to the 90% and 95% power points as described in section 2.4. Unlike the simulations, where the B-scan generated from the synthetic

gprMax data contained a single idealized root system and a homogenous soil media, the scanned boxes contained one or two plants (and in some cases a wooden dowel place holder for the NMM access tube) with variations in relative permittivity due to changes in soil volumetric water content present throughout the soil profile.

The first set of results are shown in Figure 26A, which compare the SBW at the 90% and 95% points between cotton and sorghum at each of the three survey dates with data from both soil types combined. The signal processing parameters used to generate Figure 26A were set as follows: gain type = alpha; conductivity/sigma type = EM38; background type = localized with a spatial filter width = 0.35 m; and Stolt migration employed three soil layers. In Figure 26A we see that at both the 90% and 95% power points that cotton does have a larger SBW at two of the three dates. At the final survey date on 9/18/18, the SBWs converge to nearly the same value. In the case of the 90% power point, the SBW of the sorghum actually becomes larger than that of the cotton at the final date. It is not known why this occurred other than to state that this method may not always yield the expected result. It could be that at this point in the growing season the sorghum had developed new roots which emanated from the original root mass and thus, induced a larger SBW signature compared to the previous survey date. As shown in Table 3 under the Sand & Yahola heading there was only one combination of measurement dates that yielded a significant p-value.

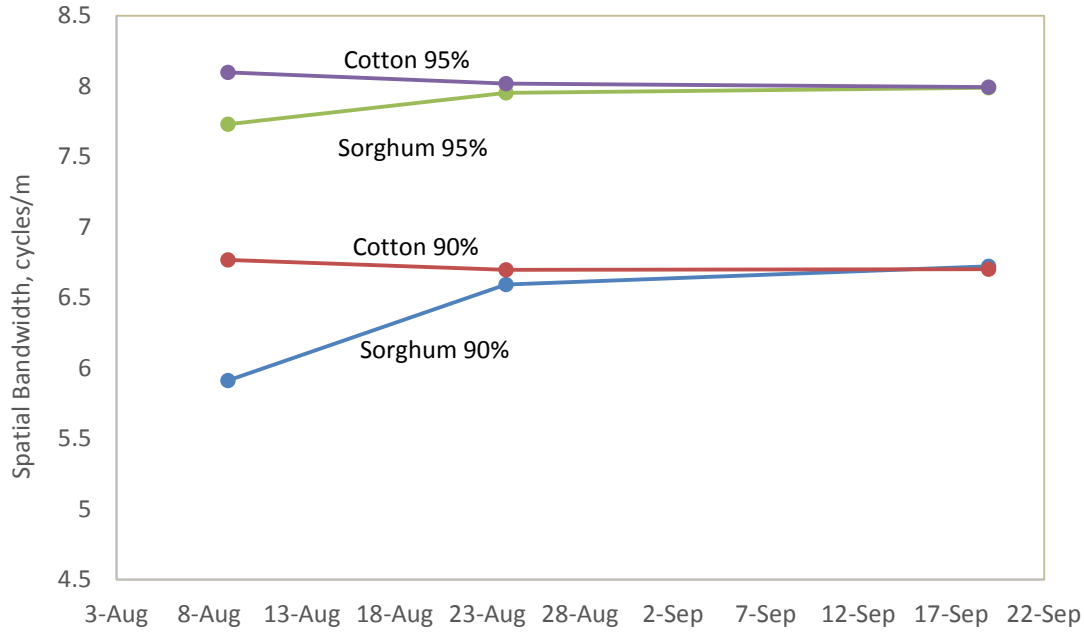

A

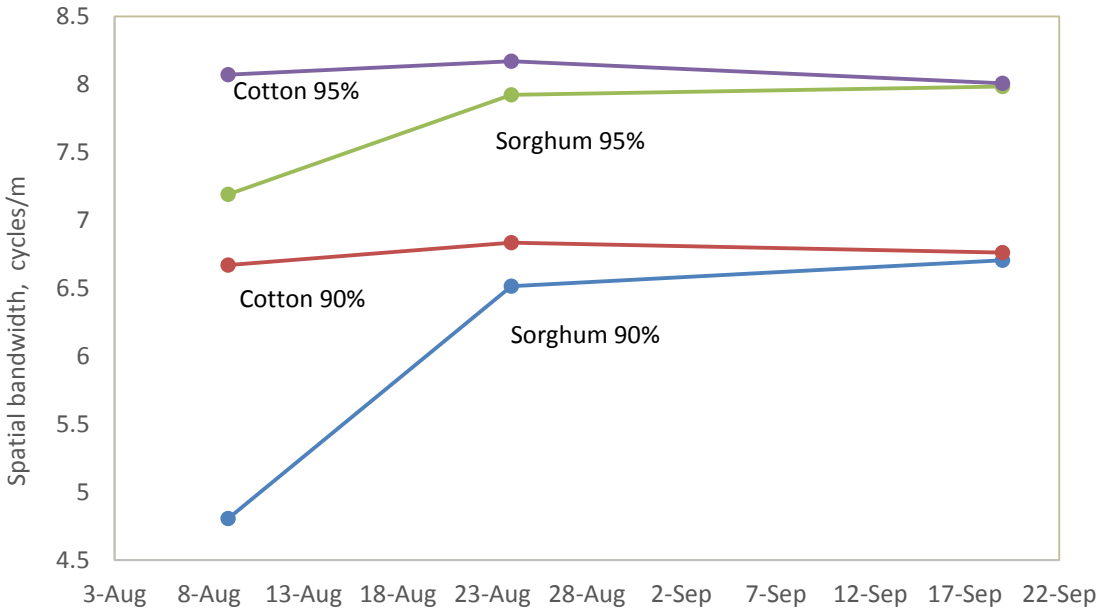

B

Figure 26: Spatial bandwidth comparison of sorghum and cotton in boxes. (A) Sand and Yahola combined. (B) Sand only. (C) Yahola only. (D) Yahola only with Noborio conductivity.

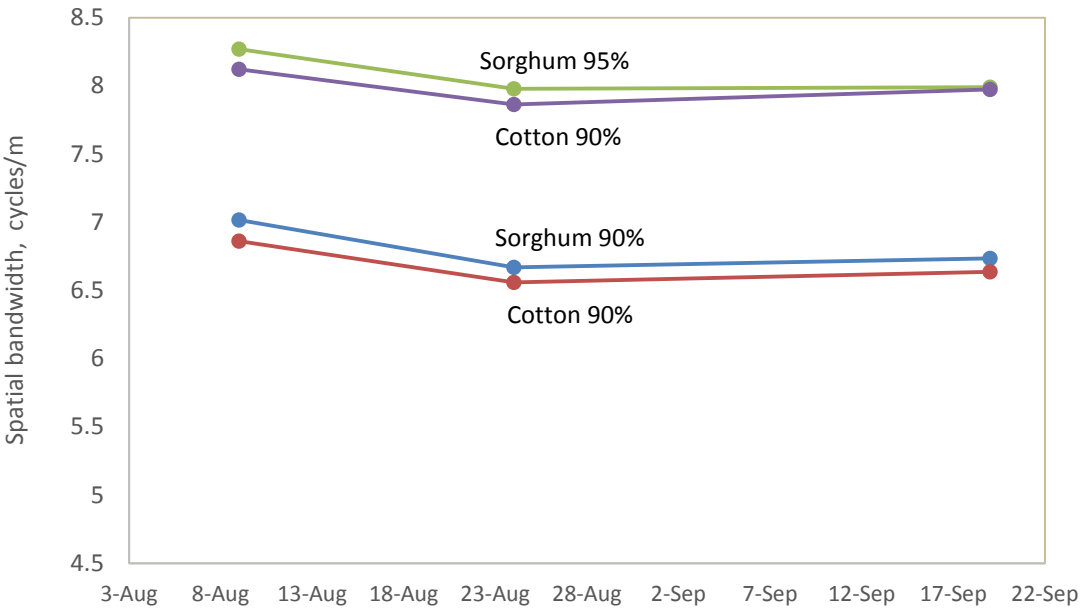

C

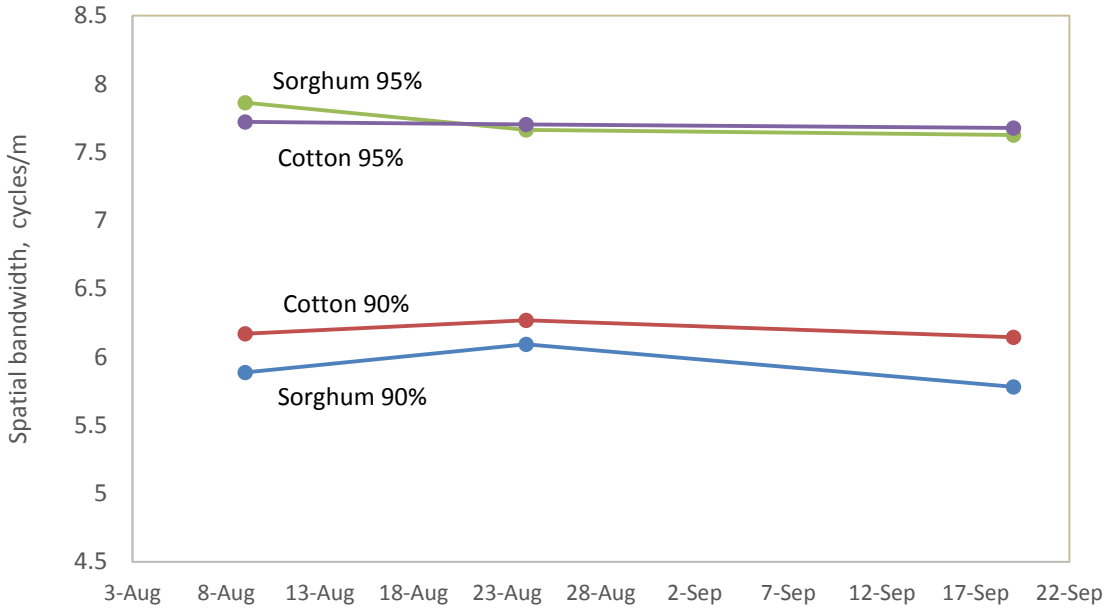

D

Figure 26: Continued

The results for the combined data for the two soil types were motivation to look at the data for the soil types taken separately. Figure 26B shows the results for just the sand boxes, while Figure 26C shows the results for just the Yahola soil boxes, where the same processing parameter values used for the combined data were used. The results in sand indicate that the mean SBW at the 90% and 95% points for cotton was indeed greater than that for sorghum at all three measurement dates, but that the visual separation was better for the 90% SBW values. The resulting p-values shown in Table 5 under the "sand only" heading were significant for all combinations including the first measurement date for the 90% value, but were only significant for two of the combinations involving the first date for the 95% value, thus verifying the better visual separation observed in Figure 26B. All other comparisons yielded results that were not significant. Note that in the following tables a highlighted value indicates a statistically significant value.

The results in Yahola shown in Figure 26C indicate the opposite of what was predicted in that the SBW at the 90% and 95% points was greater for sorghum that for cotton. This led us to investigate the use of the Noborio conductivity model to estimate the gain applied as opposed to conductivity values based upon the EM38-MK2 measurements. The results for the Noborio model do support the predicted trend (cotton > sorghum) for the 90% SBW values as shown in Figure 26D. However, the trend for the 95% SBW values was not reversed. This leads us to conclude that the 90% SBW measure is preferred to the 95% SBW measure, at least for this scenario. The resulting p-values shown in Table 5 under the "Yahola only with Noborio conductivity" heading were significant for three measurement date combinations for the 90% SBW value. A possible reason the Noborio calculation yielded a significant result and the EM38 measurements did not, was likely due to the fact that the former was based upon a sandy loam

profile near College Station, TX, and thus, was more appropriate in the Yahola and Weswood soils. A number of reasons exists that could explain why the SBW did not work as expected in the boxes. The over-arching issue was the complexity of the problem. Recall that the overall intent was to estimate the electrical properties of the roots based upon reflections captured by the GPR Rx located at or above the surface. The estimation of such below ground properties from scattered signal returns is commonly referred to as an inverse scattering problem, which is typically ill-posed (Persico, 2014). As such, any error in the signal processing, e.g. in the background signal removal, is magnified such that the resultant estimate of the scattered signal may be degraded. The resultant Stolt migration cannot correct for these errors and thus, produces an image that may have significant error. A more specific reason that the data from the boxes did not produce the expected results may be due to the uncharacteristically wet summer in 2018. The heavy, frequent amounts of rain caused issues with the distribution of water in the soil and surface soil level. These issues combined may have interfered with the GPR's ability to detect and differentiate between the types of root structures.

Table 5: P-values for box data comparisons between mean SBW of corn/sorghum and cotton.

Sand and Yahola			
Corn/Sorghum Survey Date(s)	**Cotton Survey Date(s)**	**p-value 90%**	**p-value 95%**
9-Aug	9-Aug	0.056	0.095
9-Aug	24-Aug	0.079	0.169
9-Aug	19-Sep	0.093	0.205
24-Aug	9-Aug	0.179	0.067
24-Aug	24-Aug	0.351	0.343
24-Aug	19-Sep	0.382	0.420
19-Sep	9-Aug	0.429	0.258
19-Sep	24-Aug	0.529	0.445
19-Sep	19-Sep	0.521	0.494
9-Aug, 24-Aug	9-Aug, 24-Aug	0.050	0.079
9-Aug, 24-Aug	24-Aug, 9-Sept	0.083	0.171
9-Aug, 24-Aug	9-Aug, 9-Sept	0.060	0.105
24-Aug, 9-Sept	9-Aug, 24-Aug	0.338	0.216
24-Aug, 9-Sept	24-Aug, 9-Sept	0.427	0.401
24-Aug, 9-Sept	9-Aug, 9-Sept	0.358	0.274
9-Aug, 9-Sept	9-Aug, 24-Aug	0.088	0.118
9-Aug, 9-Sept	24-Aug, 9-Sept	0.128	0.215
9-Aug, 9-Sept	9-Aug, 9-Sept	0.099	0.145
9-Aug, 24-Aug, 9-Sept	9-Aug, 24-Aug, 9-Sept	0.087	0.124

Table 5: Continued

Sand Only			
Corn/Sorghum Survey Date(s)	**Cotton Survey Date(s)**	**p-value 90%**	**p-value 95%**
9-Aug	9-Aug	0.0045	0.022
9-Aug	24-Aug	0.007	0.017
9-Aug	19-Sep	0.030	0.073
24-Aug	9-Aug	0.328	0.192
24-Aug	24-Aug	0.270	0.176
24-Aug	19-Sep	0.375	0.423
19-Sep	9-Aug	0.540	0.300
19-Sep	24-Aug	0.403	0.236
19-Sep	19-Sep	0.471	0.479

Yahola Only			
9-Aug	9-Aug	0.793	0.828
9-Aug	24-Aug	0.913	0.935
9-Aug	19-Sep	0.949	0.958
24-Aug	9-Aug	0.188	0.134
24-Aug	24-Aug	0.635	0.695
24-Aug	19-Sep	0.556	0.516
19-Sep	9-Aug	0.386	0.350
19-Sep	24-Aug	0.639	0.632
19-Sep	19-Sep	0.587	0.519

Yahola Only with Noborio Conductivity			
9-Aug	9-Aug	0.143	0.747
9-Aug	24-Aug	0.107	0.735
9-Aug	19-Sep	0.166	0.825
24-Aug	9-Aug	0.388	0.356
24-Aug	24-Aug	0.285	0.427
24-Aug	19-Sep	0.424	0.457
19-Sep	9-Aug	0.049	0.286
19-Sep	24-Aug	0.048	0.370
19-Sep	19-Sep	0.061	0.362
9-Aug, 24-Aug, 9-Sept	9-Aug, 24-Aug, 9-Sept	0.028	0.562

3.3.3 3D Analysis

Another area that was explored was generating 3D images from C-scans from data collected in the boxes containing the pipes (boxes 1 and 8). In addition, a 3D SBW analysis was conducted on C-scans collected in the boxes containing only a single plant (boxes 2 and 9). As mentioned previously, C-scans are a collection of B-scans, where a given B-scan is offset in the y direction from other B-scans by a specified amount. Thus, C-scans after suitable processing, provide a 3D image, or a sequence of 2D image slices. The 3D SBW can then be determined from the 3D image.Figures 27A and B show the results of the processed C-scans from box 1 corresponding to a sand soil and box 8 corresponding to a Yahola soil. In each box, two, hollow metal pipes of differing lengths were laid one on top of the other in the x-y plane to form a cross shape. The longer pipe was approximately 43 cm long with a 5 cm diameter and was oriented at a 45° angle with respect to the x-axis. The shorter pipe was 10 cm long with a 5 cm diameter and was oriented perpendicular to the longer pipe. In box 1, the top of the longer pipe was located at a depth of ~0.67 m, while the bottom of the shorter pipe was located at a depth of ~0.77 m. In box 8, the top of the longer pipe was located at a depth of ~0.56 m, while the bottom of the shorter pipe was located at a depth of ~0.66 m. The data captured by the C-scan was processed per the signal processing steps shown in Figure 5 followed by 3D Stolt migration. The key parameter settings were as follows: “alphaPlusSpreading” gain compensation; Noborio-based conductivity estimates; localized background estimate with spatial filter width = 0.35 m, and Stolt migration with three layers. Thus, at a top level this experiment is quite similar to the synthetic data experiment used to verify 3D Stolt migration described in section 1.3.2, although there are key differences as will be noted in the following discussion.

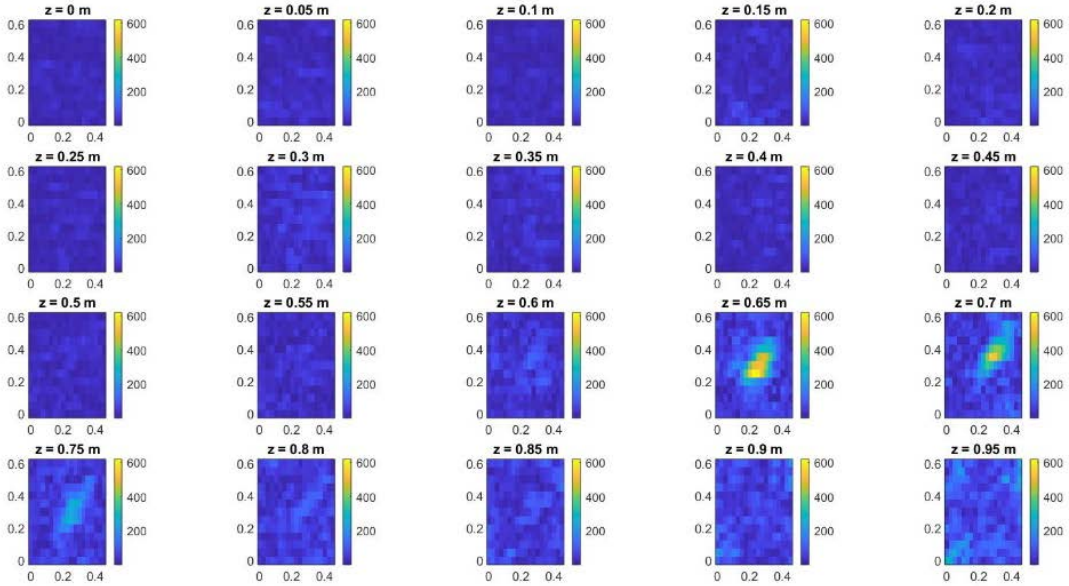

A

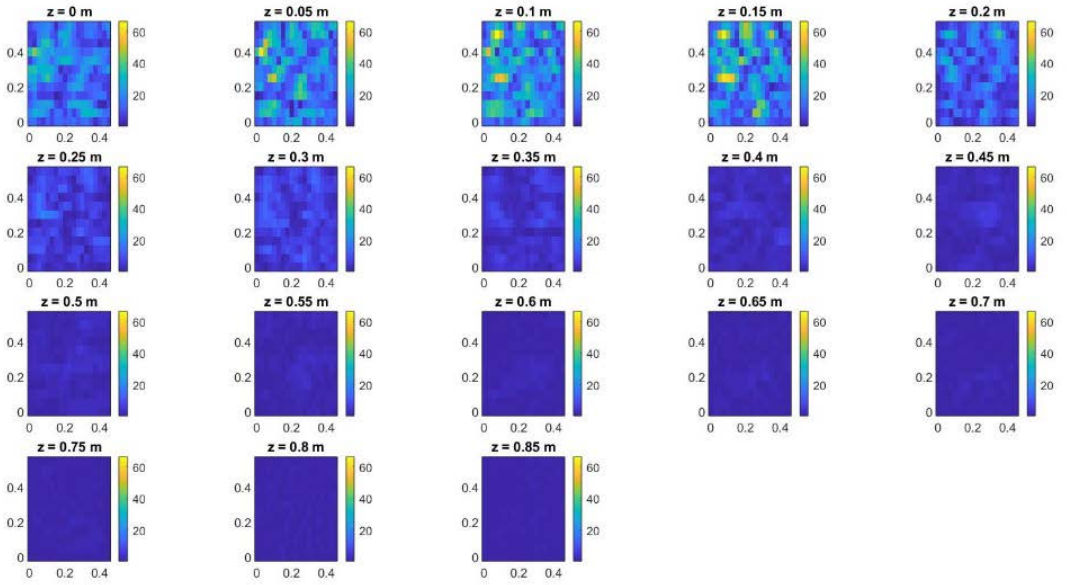

B

Figure 27: C-scan results. A) Box 1 containing sand. B) Box 8 containing Yahola.

Figure 27A shows that the pipes are detectable in the sand at approximately the correct depths, while Figure 27B shows that the pipes are essentially undetectable in the Yahola soil. This result was somewhat expected and was due primarily to the much greater signal attenuation in the Yahola soil as compared to sand. Although the pipes were detectable in the sand, the image slices of interest are not nearly as clear as that obtained with the synthetic data. One of the primary reasons for this was that in the processing of the synthetic data the background signal was exactly known since simulations were run without the pipes to precisely determine it. Thus, an ideal estimate of the scattered signal was formed by simply subtracting the known background signal from the signal received when the pipes were present. In the processing of the data from the boxes, the background signal was not known and had to be estimated from the signal, which was not an error-free process. In addition, the synthetic data was generated for a single soil layer with little loss (σ = 0.001 S/m), and thus, no gain compensation was required. In the boxes, the volumetric water content based upon NMM measurements varied with depth. Even in the box with sand, σ was estimated to be about 0.01 S/m at the depths of interest, and thus, gain compensation was required, which can also introduce error into the process. Finally, a 500 MHz Tx was used to generate the synthetic data, while the controlled experiments used a 1000 MHz Tx. The latter is a good choice from a resolution perspective, but perhaps not as good a choice as the former for detecting buried objects at medium depths. The results of this controlled experiment tend to indicate that using GPR to detect fine root structures in other than sand may be limited to shallower depths.

The next type of 3D analysis was similar to the SBW comparison of the tap and fibrous roots described in section 3.3.2 but extended from processing a 2D image to processing a 3D image or object. In this case, instead of processing a B-scan, the C-scans generated from box 2

and 9, each of which contained only one plant, were analyzed. The data obtained from the two boxes was first run through the signal processing steps shown in Figure 5, and then through a 3D Stolt Migration algorithm. Finally, an FFT was applied in all three dimensions of the resulting 3D image to produce a 3D image of the spectral content. Unlike the previous comparison between the tap and fibrous roots, the two boxes contained different soil types. Box 2 contained a single sorghum plant grown in sand, whereas box 9 contained a single cotton plant grown in the Yahola soil. Therefore, a direct comparison between the two could not be made. Instead, the SBW over time in a single box was examined to see if any change in SBW could be observed as the rooting system grew. Box 9 was selected for this type of analysis. This was done because after two surveys dates the original corn plants in box 2 had to be replaced with sorghum, whereas the cotton survived the entire growing season, and thus, more survey dates were available for analysis. Another reason box 9 with the Yahola cotton combination was selected was due to the stunted growth of the sorghum in the sand. As stated above, sand is not an ideal environment to grow a crop in, and therefore, it did not grow nearly as well as it would have in the field. However, the cotton plant grew at a more normal rate as opposed to the sorghum in the sand. Data for the cotton-Yahola combination was collected on four survey dates in 2018: 7/13, 7/27, 8/2 and 8/28. For each date the 90% and 95% 3D SBW points were calculated. Figure 28 shows the results over time, where two sets of results are shown for the 90% and 95% points. One set corresponds to processing all of the z axis “lines” produced by Stolt migration (NzRemove = 0), while the second set corresponds to processing all but the first z line, which extended from the surface to a depth of 5 cm (NzRemove = 1). The latter was investigated to see if near surface noise was corrupting the results, but as shown in Figure 27 there is not much difference whether the first line is removed or not. The expected result was that as the rooting

system expands, the SBW would decrease over time. This expected decrease did occur between the first and second dates, and between the third and fourth dates, but there was a positive inflection between the second and third dates. A possible reason for the positive inflection is that new root growth between the second and third dates could have emanated from the main root in such a way as to increase the spectral signature, but then with further growth there was a "filling in" effect such that the tap root appears wider and thus, a decrease in the spectral signature.

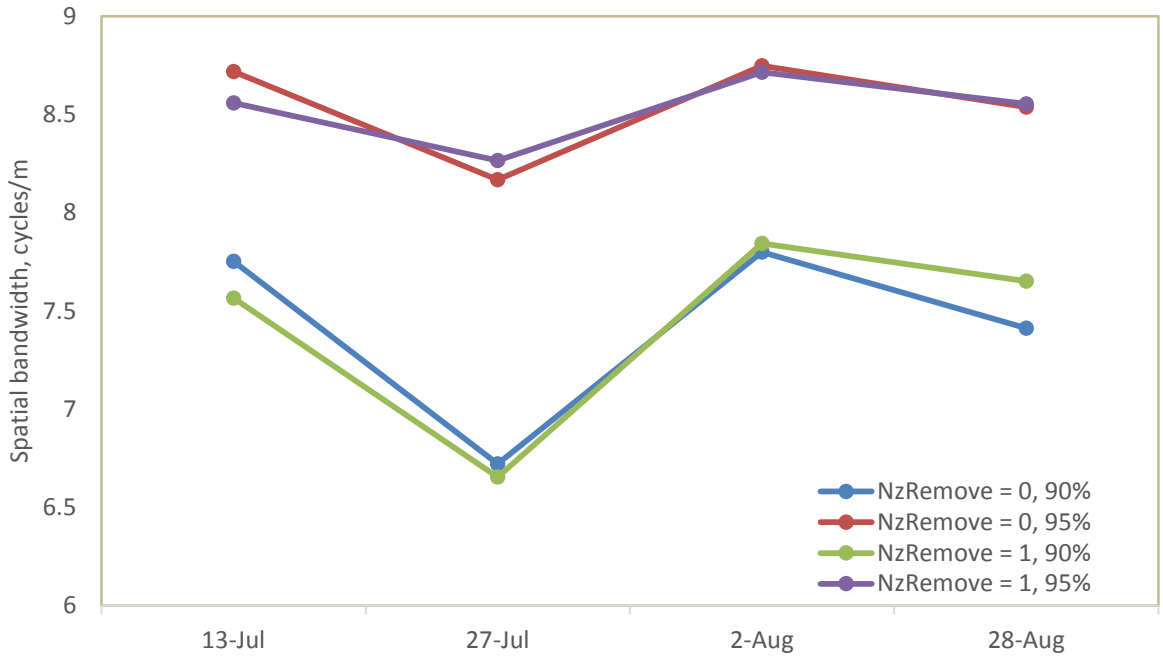

Figure 28: 3D Spatial bandwidth comparison over time with first z-slice removed and not removed.

3.4 Summary

In summary, this chapter described the set of controlled experiments that combined GPR measurements with measurements of soil water content and soil conductivity to: (1) estimate the energy per trace at plant and non-plant locations, (2) determine the SBW of recovered images for sorghum and cotton plants for purposes of differentiating between their respective root structures, and (3) verify use of 3D Stolt migration as a viable technique for detecting sub-surface objects. The energy analysis focused on developing the EPT and then comparing the corresponding average or mean value at non-plant and plant locations. The results indicated that for both sand and Yahola that the mean EPT at plant locations was greater than the mean EPT at non-plant locations for all three of the measurement dates examined. Indicating that these more controlled conditions GPR could detect the presence of roots. However, the results were much more conclusive in sand, where the associated p-values met the 0.05 confidence level for all three of the sorghum measurement dates, and two of the three cotton measurement dates. For Yahola, the p-values met the confidence level for two of the three sorghum measurement dates but did not meet it for any of the cotton dates although it was very close for one of the dates. The conclusions are that better results were obtained in sand by virtue of its lower signal attenuation, and that sorghum led to better results by virtue of its more spread out root structure.

The second analysis compared the SBW of plants with fibrous roots (sorghum) to plants with tap roots (cotton). The hypothesis was that the SBW of cotton should be greater than that of sorghum based upon the idealized analysis conducted in section 2.4. The results in sand did indicate that the mean SBW at the 90% and 95% points for cotton was indeed greater than that for sorghum at all three measurement dates, but that the separation was better for the 90% SBW

values. The resulting p-values were only significant at the first measurement date. The results in Yahola with the gain applied based upon the EM38 conductivity measurement indicate the opposite of what was predicted in that the SBW at the 90% and 95% points was greater for sorghum than for cotton. When the gain was switched such that it was based upon the Noborio conductivity model the proper trend (cotton > sorghum) was observed for the 90% SBW values, and in fact one of the measurement dates had a significant result. However, the trend for the 95% SBW values was not reversed. This leads us to conclude that the 90% SBW measure was preferred to the 95% SBW measure, at least for this scenario. Overall, the performance was "better" once again in sand as opposed to Yahola. In addition to the above 2D measures of SBW, the 3D SBW was determined for cotton in Yahola soil over time by processing C-scans collected at four separate measurement dates. The expectation was that the 3D SBW would decrease over time since the spatial signature would conversely be increasing in size. The expected trend was observed between the first and second dates, and then between the third and fourth dates, but not between the second and third dates. A possible reason for the 3D SBW increasing between the second and third dates was that new root growth could have emanated from the main root in such a way as to increase the spectral signature, but then with further growth between the third and fourth dates there was a "filling in" effect such that the tap root appears wider and thus, a subsequent decrease in the spectral signature.

Finally, the results of the 3D Stolt migration of C-scans of boxes with metal pipes buried at known depths indicate that the pipes are detectable in the sand at about the right depths, while the pipes are essentially undetectable in the Yahola soil. This result was somewhat expected and was due primarily to the much greater signal attenuation in the Yahola soil as compared to sand

and supports the notion that it should be increasingly difficult to detect the small-scale roots in the Yahola soil.

The mixed results seen in the box study could be a result of a number of factors. First, as stated above, was the overall complexity associated with an inverse-scattering problem. This issue can introduce sources of error early in the processing steps and that will only be magnified in later analysis. Additionally, utilizing GPR in fine root phenotyping, is a relatively novel application, and the appropriate types of post processing and analysis techniques have not been solidified. Finally, even though the boxes were designed to represent a controlled study, not all environmental factors could be controlled. For example, the heavy rain events throughout the season and shifting of the soil could influence GPR's ability to accurately detect and differentiate rooting structures.

CHAPTER IV

FIELD EXPERIMENTS

4.1 Introduction

After testing the feasibility of GPR to detect and differentiate rooting systems in a controlled environment, the next step was to take measurements in field situations where not all parameters could be as carefully controlled. The controlled experiments were designed to represent ideal conditions for GPR data collection, however this is not representative of the conditions encountered in the field. Field measurements are influenced by a variety of factors and it is important to test GPR's ability to overcome these changes and test if it can be used as a phenotyping tool in more realistic conditions. In an active field such things as tillage, weeds and changes in soil conditions can alter and affect GPR data collection. To test the capability of GPR for phenotyping root biomass in the field, several experiments were designed and conducted during the summers of 2017 and 2018. Plots with different crop types and soil textures were selected to test the feasibility of GPR for phenotyping in different field conditions. In addition to GPR measurements, the same soil monitoring devices used in the controlled experiment were used. These included the EM38-MK2 for bulk apparent conductivity readings, the neutron moisture meter and theta probe for multiple depths measurements of soil water content. Similar to the controlled experiments, these measurements were integrated into GPR signal processing in an attempt to capture the influence of changing soil characteristics. The same types of analysis, energy and image that were utilized in the simulations and controlled experiments were again implemented. First, energy analysis was used to test if GPR could detect the presence or absence of roots, and then image analysis, specifically SBW comparison, was used to test if a difference

existed in the GPR signal associated with a tap root versus a fibrous root. The objective of this chapter was to assess the potential for GPR to detect root biomass and structure by incorporating soil electromagnetic properties in field experiments.

4.2 Methods

In 2017 two sites were selected in Texas for field tests. The first site was at the Stiles Farm Foundation near Thrall, TX. The soil at this location was classified as a Burleson clay with 40 - 60% clay content (fine, smectitic, thermic, Udic Haplusterts). The second site was at the Texas A&M AgriLife Research & Extension Center at Lubbock, TX. The soil in Lubbock was an Olton clay loam (fine, mixed, superactive, thermic Aridic Paleustolls). Each location contained plots of sorghum (fibrous root structure), cowpea (tap root structure) and a nine-species cover crop mix which contained both types of rooting systems. All plots at both locations were under no-till management to minimize soil disturbance. The GPR used in the field campaigns was the same Sensors & Software pulseEKKO unit used in the controlled experiments. In 2017 the only transducers available had a central operating frequency of 500 MHz. GPR transects approximately 8 m long were run parallel to crop rows with transmitter on one side of the plant and receiver on the other, also known as the perpendicular common offset configuration as shown in Figure 8 that was utilized in the controlled box experiment. Again, this was chosen to maximize GPR's potential ability to detect root structure. In addition to the data collected from the transects that ran parallel to the crop rows, GPR transects were also run perpendicular or across crop rows. This was done to provide a clearer distinction between plants. As opposed to plants within the same row, which had the potential to be close to one another, making it difficult to differentiate individual root systems, the plants along the perpendicular transect were

separated by an entire row and within each transect there was only 2 to 5 plants, depending on the number of rows crossed. This was especially important in the mixed cover crop where the plants within the row were in very close proximity to one another, at times less than 5 cm apart. Each transect, whether parallel or perpendicular, was run twice with different antenna orientations, first with antennas oriented perpendicular to direction of travel and second with antennas oriented parallel to direction of travel. An A-scan was collected at 5 cm increments and the location of each plant was noted. Flags were placed at the beginning and end of each transect to maintain consistency in transect location across all survey dates.

Similar to the controlled box experiment, the EM-38MK2, neutron moisture meter and theta probe were used to monitor soil moisture. EMI readings were taken at approximately the same time as the GPR scans, along the same rows of crop in each plot. Access tubes were inserted along the GPR transect within the plant row and moisture measurements at 20, 40, 60, and 80 cm depths were taken at the time of GPR data collection. Theta probe measurements were taken at multiple locations along each transects.

Unfortunately, a majority of the results from the 2017 data set were inconclusive. This was most likely due to the soil type at each location. The soil in Thrall especially wasn't ideal for ground penetrating radar measurements due to the extremely high clay content (40-60%) which had the potential to cause major signal attenuation. The Olton clay loam at the Lubbock location didn't have as high of clay content, however, a severe weed infestation on the plots made data collection and processing difficult. The density of the weeds made it challenging to differentiate between what was the desired crop root and what was the unwanted weed root. Another potential issue was the influence of the aluminum NMM tubes on both the GPR data and the

EMI data collected with the EM-38MK2. The aluminum material is highly conductive and therefore the aluminum will dominate the signals of both the EM and GPR of surrounding measurements potentially masking all other information. Due to the variety of setbacks in the first field experiment, the 2017 field campaign served as a test for methodologies that were later improved upon in the 2018 season, which resulted in the collection of more conclusive data.

The second set of field experiments was conducted on a Yahola very fine sandy loam (coarse-loamy, mixed, superactive, calcareous, thermic Udic Ustifluvents) and on a Weswood silt loam (fine-silty, mixed, superactive, thermic Udifluventic Haplustepts) at the Texas A&M Farm located outside of College Station, TX in 2018. As with the box experiment, data was collected for a tap root crop, i.e. cotton, and for a fibrous root crop, in this case corn with a plot of each crop on each soil series for a total of four plots. Two transects were collected on each plot. Similar to the 2017 methodology, one GPR transect approximately 6 m long was run parallel to the crop rows, with the transmitting and receiving antenna on opposite sides of plant and moved in tandem in 5 cm increments taking note of each plant location. The second transect of similar length bisected the first transect at its midpoint and ran perpendicular to the crop rows, creating a ‘cross’ shape. Two individual neutron moisture meter access tubes, now made of PVC instead of aluminum to minimize its influence on the EM-38 and GPR, were placed at the end of each transect and one additional access tube placed at the center for a total of five NMM access tubes in each ‘cross’ transect formation. The NMM access tubes also served as starting and ending points for each transect to keep the length and location of the transect consistent throughout all survey dates. The antenna orientation used were the same as those used in 2017, parallel-parallel and perpendicular-perpendicular. At the time of each GPR survey the EM38-MK2, NMM, and Theta probe were used to collect the ancillary soil moisture data. The EM-

38MK2 was run directly over the transect for purposes of collecting bulk electrical conductivity data. The neutron moisture meter was used to take measurements at 20, 40, 60 and 80 cm, although the 80 cm measurement was not used in any of the processing. In the corn field, the theta probe measurements were taken at every plant location. However, the plants on the cotton field were too dense and measurements could not be taken at each individual plant. Instead, a measurement was taken at every meter along the transect including the starting location for a total of 7 measurements per transect. Multiple surveys were taken throughout the seasonal dry down from May to September.

The same two types of analysis, energy and image, were utilized with the field data. To determine if our hypothesis that the mean energy per trace at plant locations was greater than the mean energy per trace (MEPT) at non-plant locations could be backed by statistically significant data, statistical analysis for GPR data collected in the field across a number of measurement dates was conducted. The average or mean energy per trace was computed across plants of the same type and across the two antenna orientations for both plant and non-plant locations. The non-plant EPT corresponding to a given plant location was calculated based upon the traces midway between the plant of interest and the adjacent plants. This approach for the non-plant EPT was used to minimize the interference due to reflections from the plants. Specifically, data was collected for Weswood and Yahola soils for corn and cotton plants. The corn data was collected on 5/20, 5/30, 6/27, and 7/16, while the cotton data was collected on 6/27, 7/16, and 8/7. The methodology used to determine the SBW for the field experiments was similar to that of the box experiments, but with some differences noted as follows. First, in the parallel transect, or the transect that went along the crop rows, the SBW was calculated by dividing the 6-meter transect into six, 1-meter sections. Within each section the SBW was calculated, and then these

values were averaged for one final bandwidth value. On the perpendicular transect, or the transect running across the plant rows, a 1-meter section was centered on each plant along the transect (4 – 5 plants per transect). Each meter-long section was run through Stolt migration to form an image from which the SBW was determined. The resulting value was averaged with the other sections for a final single SBW value for the whole perpendicular transect. Recall that for the box experiments that only a single image was developed per box, although there was some averaging across boxes with the same plant type.

4.3 Results

As in the box experiments, the same two types of analysis were performed on the field data. First energy analysis was used to determine if there was a difference in signal energy level at plant and non-plant locations along the transect. Next, the SBW of the cotton and corn were compared to determine if a difference could be seen between fibrous and taps roots.

4.3.1 Energy Analysis

Figure 29 is a representative example of the energy data collected from a row of corn planted in Yahola soil. In the field, the data was much nosier even after post processing was applied. It is difficult to differentiate between plant and non-plant locations based on energy in this case. At some points the plant locations have low energy and non-plant locations have some of the highest energy values. However, for this example the average or mean energy per trace over all plant locations was as expected found to be higher than the average over the non-plant locations, with respective values of 2.62 fJ and 1.90 fJ.

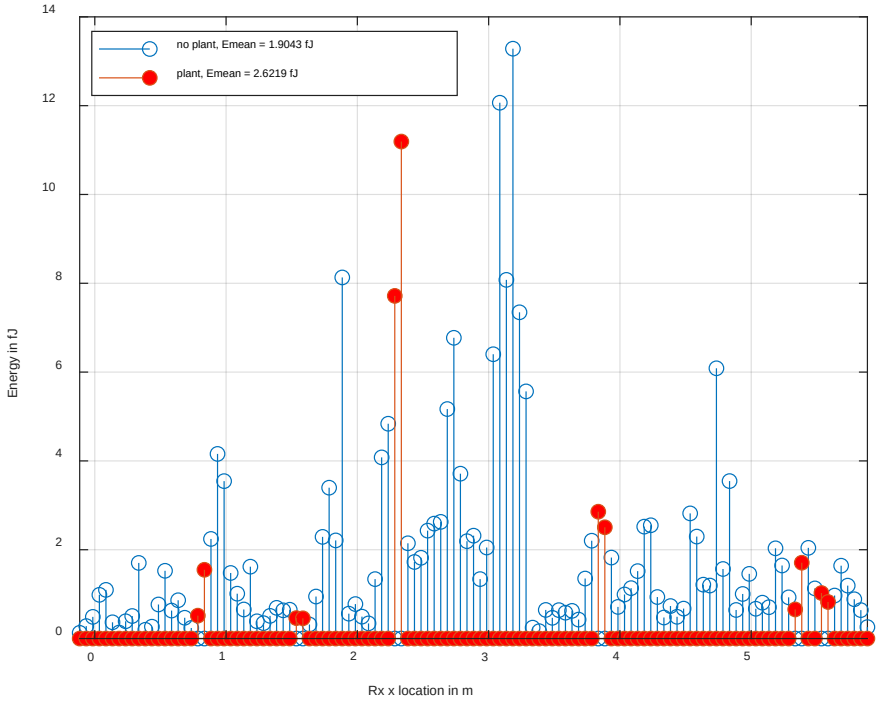

Figure 29: Representative energy comparison in field on Yahola with corn between non-plant (blue lines) and plant locations (red lines).

The next step was to compare the mean energy per trace (MEPT) in different crop, soil combinations across multiple dates. The MEPT for corn and cotton compared to the MEPT at non-plant locations in the Weswood soil is shown in Figures 30A and 30B, where we see that the corn MEPT was greater on 2 of the 3 dates, while the cotton MEPT was greater for all of the dates. The resulting p-values for corn and cotton taken individually and then corn and cotton taken together in the Weswood soil are shown in Table 6, where we see that none of the corn results were significant, while only one of the cotton results was significant. Three issues to note in these and succeeding figures related to the field data are (1) that the corn data collected on

5/20 and 5/30 is merged into one data set labeled 5/30, (2) a constant or no gain condition was found to provide better results than when gain was applied, and (3) the 500 MHz Pulse EKKO transducers were used for the 5/20, 5/30 and 6/27 measurements, while the 1000 MHz transducers were used for the 7/16 and 8/17 measurements. The reason for this latter shift was that we had just recently acquired the 1000 MHz transducers. A key point to note here is that the 500 and 1000 MHz data are not normalized with respect to one another, and thus, one cannot make accurate time-trend comparisons from the data.

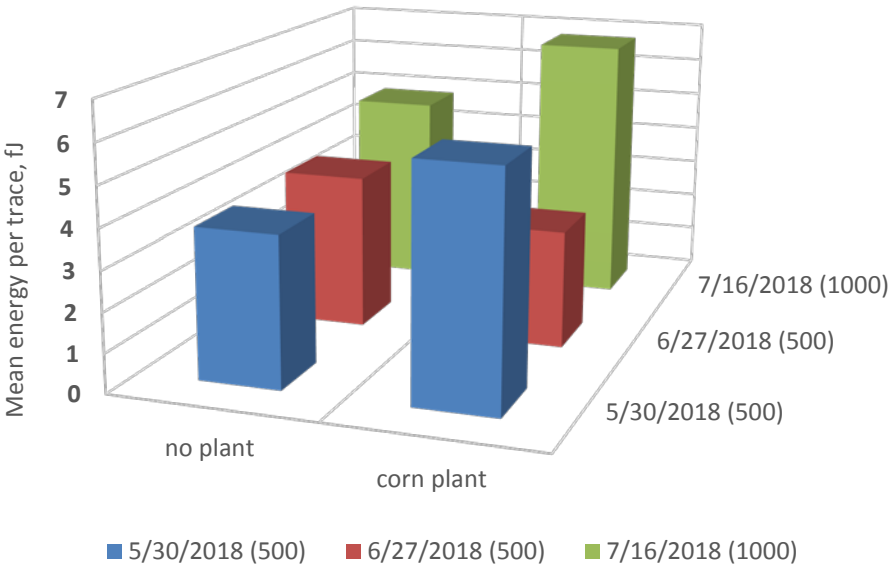

A

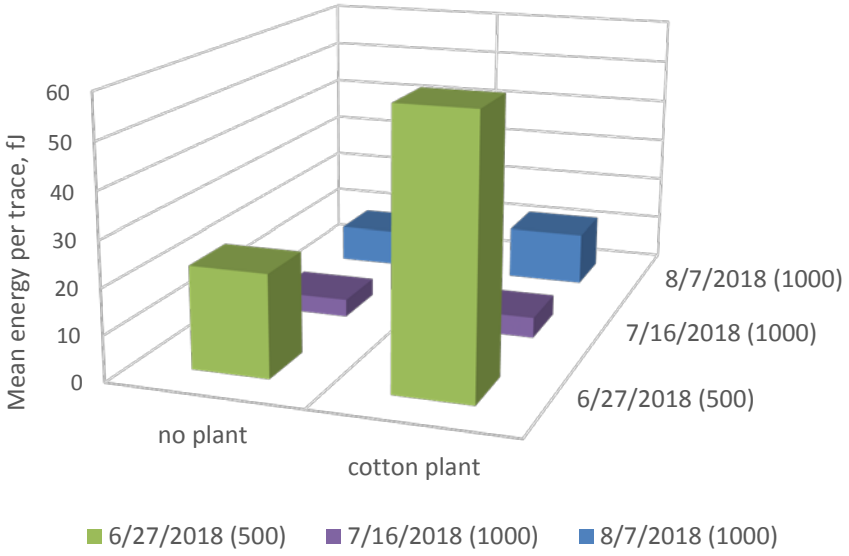

B

Figure 30: Energy analysis for field data. (A) Mean energy per trace for corn in Weswood. (B) Mean energy per trace for cotton in Weswood.

Table 6: P-values for MEPT of plant and non-plant locations in Weswood field data.

P-values Weswood Field			
	Corn	**Cotton**	**Combined**
5/30/2018	0.3616		
6/27/2018	0.7872	0.01494	0.05576
7/16/2018	0.1928	0.2476	0.1301
8/7/2018		0.1361	

The results for Yahola soil are summarized in Figures 31Aand 31B and Table 7. Figures 31A and 31B show the MEPT for corn and cotton compared to the MEPT at non-plant locations, where the MEPT for corn was greater for only one date, while MEPT for cotton was greater for two of the three dates. The resulting p-values in Table 7 demonstrate that only one result for cotton was significant, while no results were significant for corn. These results for Yahola when compared with the prior results for Weswood tend to indicate that GPR performed better in the Weswood soil as shown in Table 8. In fact, the p-value for cotton in Weswood was significant. The reason that GPR performs better in Weswood compared to Yahola was due to the lower signal attenuation associated with the Weswood soil. The latter was confirmed from the EM38 conductivity measurements for the two soils, where the average values captured by the 0.5 m spacing Rx coil for Weswood are all lower than those for Yahola as shown in Figure 32A for corn and Figure 32B for cotton. Recall that the attenuation coefficient, alpha for this application was nearly linear with conductivity. Also, of note was that "better" results were obtained for tap-root cotton as opposed to fibrous-root corn, which is the opposite of what was seen in the boxes, where fibrous-root sorghum provided better results than tap-root cotton. However, this latter

result was consistent with the conductivity values associated with the cotton plants in the field being lower than those for the corn plants in the field in all but one condition as shown by comparing the values in Figures 32A and 32B.

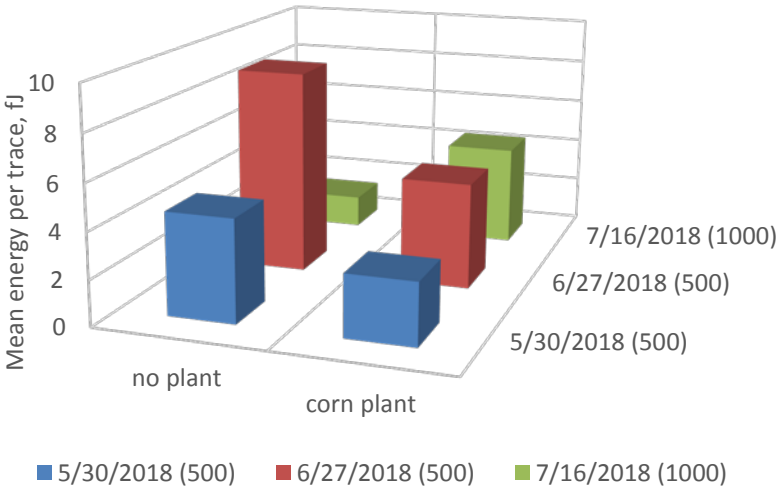

A

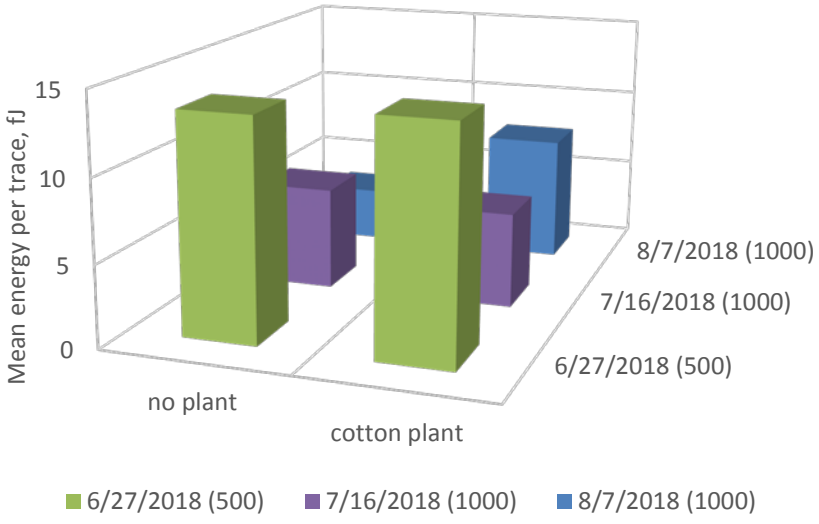

B

Figure 31: Energy analysis for field data. (A) Mean energy per trace for corn in Yahola. (B) Mean energy per trace for cotton in Yahola.

Table 7: P-values for MEPT of plant and non-plant locations in Yahola field data.

P-values Yahola Field			
	Corn	**Cotton**	**Combined**
5/30/2018	0.7371		
6/27/2018	0.8884	0.477	0.7192
7/16/2018	0.08523	0.5846	0.1562
8/7/2018		0.01765	

Table 8: P-value comparison of MEPT between Yahola and Weswood.

P-value Comparison Yahola and Weswood			
	Corn	**Cotton**	**Combined**
Yahola, all dates	0.7216	0.3154	0.487
Weswood, all dates	0.3234	0.0333	3.59E-02

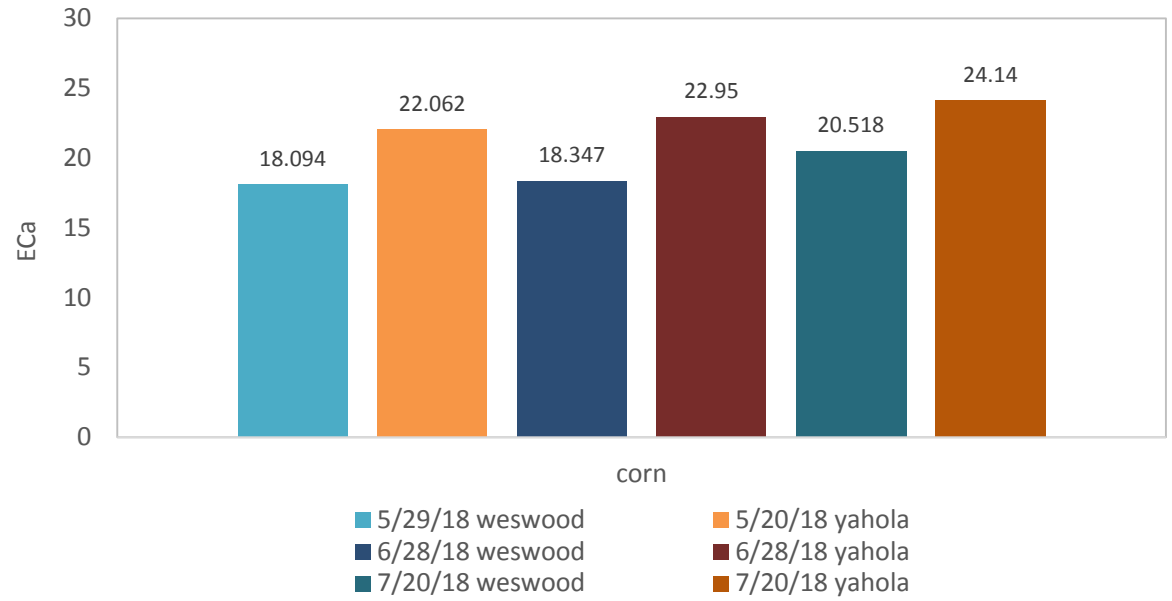

A

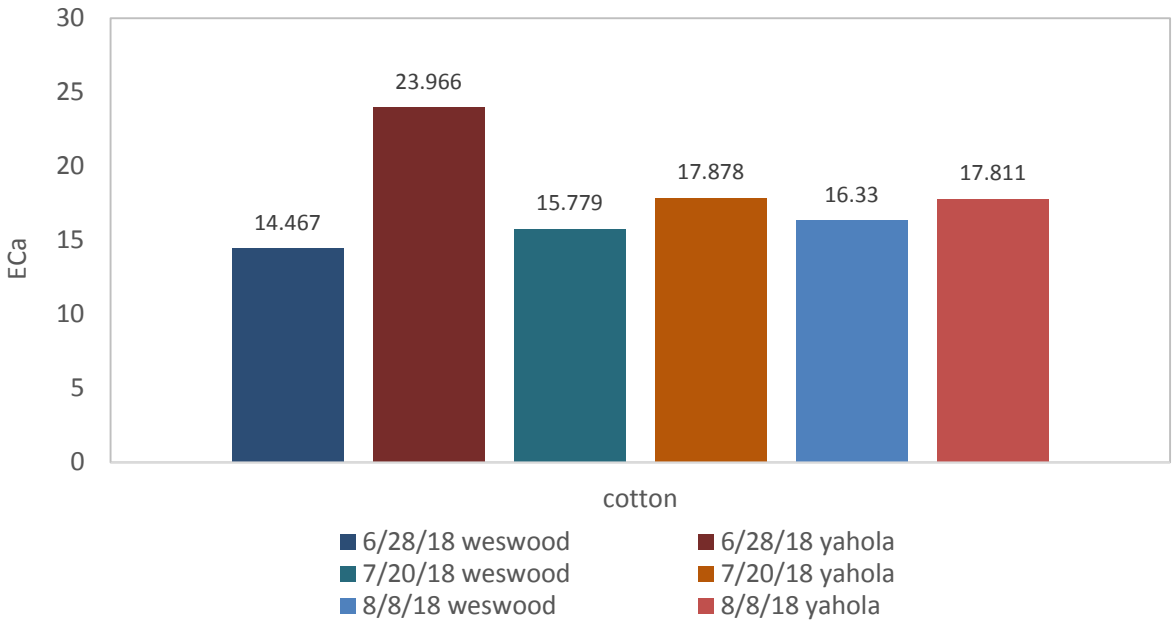

B

Figure 32: Soil conductivity comparison in mS/m. (A) Corn plants. (B) Cotton plants.

Overall, the field results for the energy analysis are not quite as conclusive as the box results, which may be due to several factors. One potential issue dealt with the GPR unit itself, since during data collection it was difficult to keep the separation between the two GPR antennas constant, so some variation in separation length existed. In the cotton field, the influence of tillage could have played a part in influencing the results. The act of tilling can create small-scale changes in elevation and cause the GPR antenna to sit at an angle which would alter the GPR signal. Steps were taken to attempt to place the antennas on as level of surface as possible, but it was impossible to remove all variations in surface heterogeneity. Additionally, by the nature of the field experiment parameters, not all environmental factors could be controlled. First, weeds were a problem in the corn plots. Prior to each survey the weeds were removed from the surface soil using a hoe. The act of hoeing disturbed the top portion of the soil and only removed part of the weed roots. Deeper roots could not always be completely removed, and some remained within the soil. Both issues could influence a GPR signal. The plots were a part of an active farm and various farm equipment and irrigation lines ran through the plots which could affect the distribution of water across the GPR transects and influence soil conditions such as bulk density from compaction.

4.3.2 Spatial Spectral Content Analysis

The spatial spectral content analysis was used to determine if the SBW of tap roots was greater than the SBW of fibrous roots based upon data collected in a number of field experiments. This analysis which determines the SBW at the 90% and 95% power points was initially discussed in sections 1.3.2 and 2.4, with results for the box experiments described in

section 3.3.2. In the case of the field experiments, corn was representative of the fibrous root structure, while cotton was representative of the tap root structure.

The first set of field results is shown in Figure 33, where we see the SBW at the 90% and 95% points for corn and cotton across both soil types, Weswood and Yahola, as a function of the measurement dates. Figure 34 show that the corn with the fibrous rooting system consistently has a lower SBW at both 90% and 95% points than the tap roots of cotton, although the difference is rather small at the 7/16/18 measurement date. The signal processing parameters used to generate Figure 33 and the succeeding figures in this section were set as follows: gain type = alpha; conductivity or sigma type = EM38, background type = localized with a spatial filter width = 0.35 m; and Stolt migration employed three soil layers.

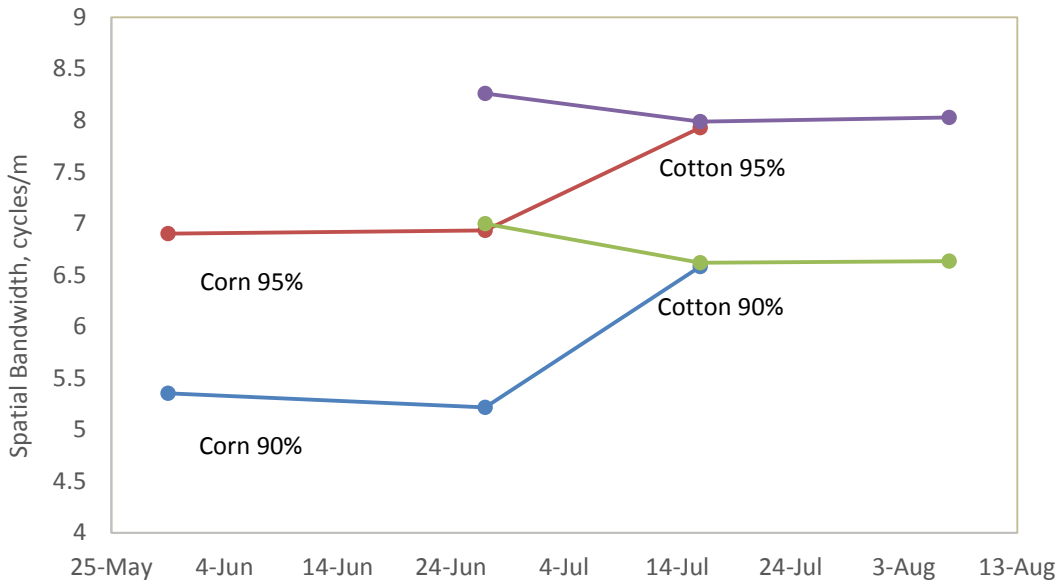

Figure 33: Spatial comparison of corn and cotton from Yahola and Weswood combined.

The dates of comparison and the associated p-value calculated for the comparison between cotton and corn across both soils are shown in Table 9 under the heading "Yahola & Weswood, Combined". The highlighted values indicated where the difference in SBW was statistically significant. In Table 9 we see a majority of the comparisons yielded significant results for both the 90 and 95% points. The comparisons that did not result in statistically significant p-values were all associated with the corn survey date of July 16th. Figures 34A and 34B, compare the SBW for the 90 and 95% points across the same set of measurement dates, but now the data is separated based on soil type, Yahola only and Weswood only. In the Yahola only comparison shown in Figure 34A we see the expected result that the mean SBW of the cotton plots is consistently greater than that of the corn plants. In addition, Table 9 under the heading "Yahola only" shows that the associated p-values are all statistically significant expect for the comparisons made with the values collected on July 16th in the corn field. However, in the Weswood only comparison shown in Figure 34B a visual difference exists between cotton and corn at the first two survey dates (for each plant), but at the third date the corn's SBW value is greater. Looking at Table 9 under the heading "Weswood only" we see that none of the comparisons had statistically significant results. A possible reason for the Weswood soil producing no significant results was due to its texture classification. Weswood soil's higher perceived clay content, though this is not backed with laboratory data, could give rise to higher signal attenuation, but that was not shown to be the case in the energy analysis results section 4.3.1, where Weswood's attenuation coefficient was estimated to be lower than that of Yahola.

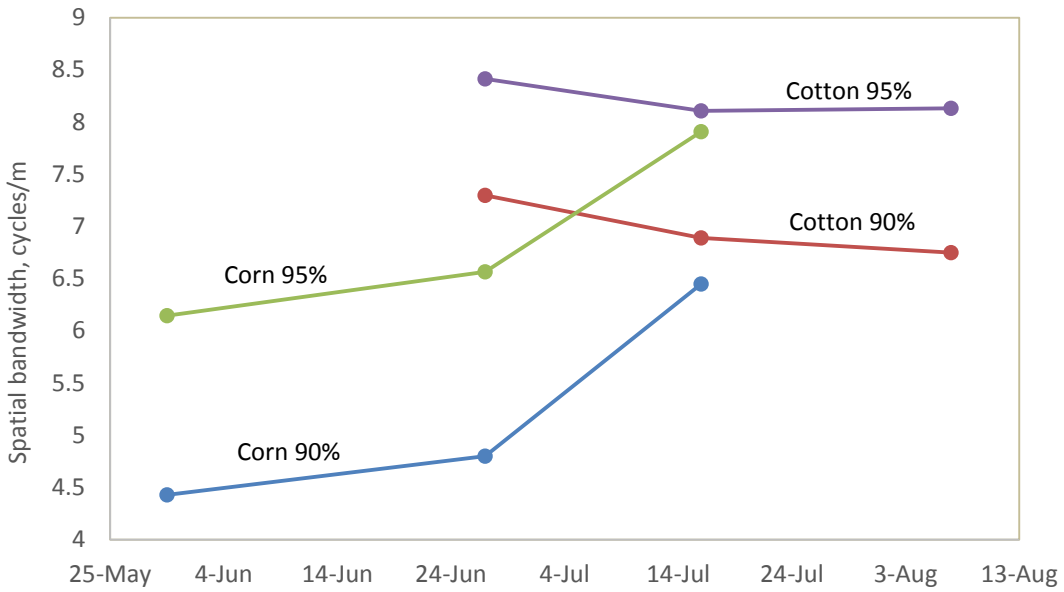

A

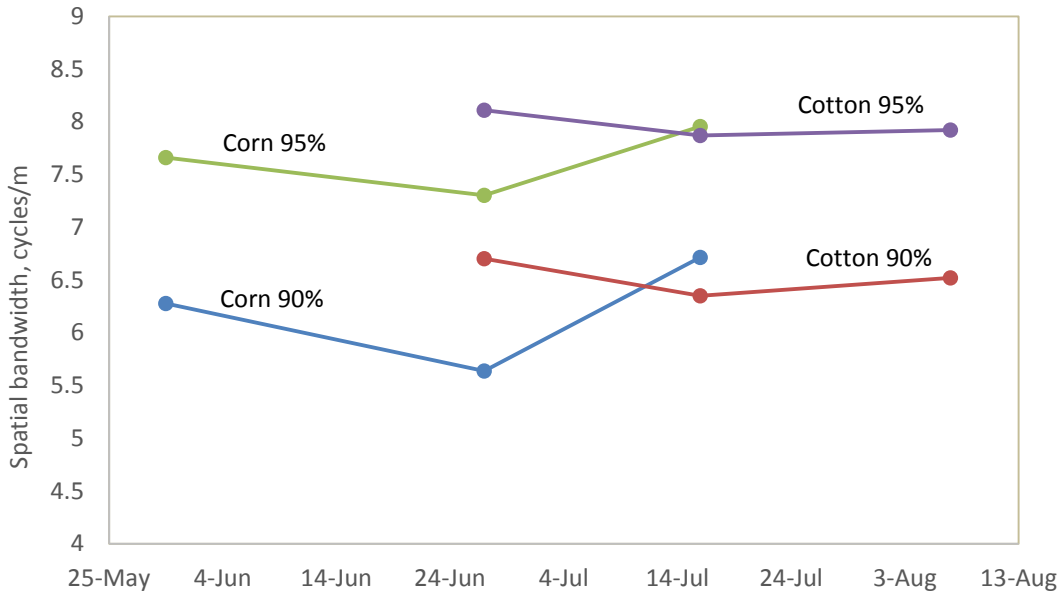

B

Figure 34: Spatial comparison of corn and cotton. (A) Yahola data only. (B) Weswood data only.

Table 9: P-values for field data comparisons between mean SBW of corn and cotton.

Yahola & Weswood Combined			
Corn Survey Date(s)	**Cotton Survey Date(s)**	**p-value 90%**	**p-value 95%**
30-May	27-Jun	0.006	0.005
30-May	16-Jul	0.018	0.014
30-May	7-Aug	0.017	0.012
27-Jun	27-Jun	0.001	0.003
27-Jun	16-Jul	0.002	0.008
27-Jun	7-Aug	0.002	0.007
16-Jul	27-Jun	0.092	0.034
16-Jul	16-Jul	0.422	0.293
16-Jul	7-Aug	0.388	0.200
30-May, 27-Jun	27-Jun, 16-Jul	0.000	0.000
30-May, 27-Jun	16-July, 7-Aug	0.000	0.000
30-May, 27-Jun	27-June, 7-Aug	0.000	0.000
27-Jun, 16-July	27-June, 16-July	0.002	0.003
27-Jun, 16-July	16-July, 7-Aug	0.006	0.008
27-Jun, 16-July	27-June, 7-Aug	0.002	0.003
30-May, 16-July	27-June, 16-July	0.009	0.005
30-May, 16-July	16-July, 7-Aug	0.022	0.013
30-May, 16-July	27-June, 7-Aug	0.008	0.005
30-May, 27-Jun, 16-July	27-June, 16-July, 7-Aug	0.000	0.000

Yahola Only			
30-May	27-Jun	0.002	0.004
30-May	16-Jul	0.003	0.005
30-May	7-Aug	0.003	0.004
27-Jun	27-Jun	0.008	0.022
27-Jun	16-Jul	0.011	0.034
27-Jun	7-Aug	0.012	0.031
16-Jul	27-Jun	0.016	0.019
16-Jul	16-Jul	0.088	0.148
16-Jul	7-Aug	0.194	0.151

Table 9: Continued.

Weswood Only			
Corn Survey Date(s)	**Cotton Survey Date(s)**	**p-value 90%**	**p-value 95%**
30-May	27-Jun	0.304	0.221
30-May	16-Jul	0.457	0.342
30-May	7-Aug	0.352	0.305
27-Jun	27-Jun	0.073	0.065
27-Jun	16-Jul	0.081	0.107
27-Jun	7-Aug	0.052	0.091
16-Jul	27-Jun	0.508	0.312
16-Jul	16-Jul	0.937	0.777
16-Jul	7-Aug	0.838	0.612

4.4 Summary

In summary, this chapter described the results for the field experiments conducted in 2018. The field data was analyzed in the same manner as the box data by examining changes in energy between non-plant and plant locations and comparing the SBW between fibrous and tap roots. Two plants types were investigated in each of the two soil types across three measurement dates: corn (fibrous) and cotton (tap-root) in Weswood and Yahola soils. The results of the energy analysis indicate that in Weswood soil that the corn MEPT for plant locations was greater than non-plant locations for two of the three measurement dates, while the cotton MEPT was greater for all of the dates. The resulting p-values for corn and cotton taken individually indicate that none of the corn results were significant, while one of the cotton results was found to be significant. The results for Yahola soil show that the MEPT for corn was greater than non-plant locations for only one of the measurement dates, while for cotton the MEPT was greater for two

of the three dates. The resulting p-values show that only one result for cotton was significant, while no results were significant for corn. The Yahola results when compared with the Weswood results tend to indicate that GPR performed better in the Weswood soil. This was confirmed by the fact that the p-values for corn and cotton in Weswood soil are lower than the p-values for Yahola soil when both sets of results are taken across all measurement dates. In fact, the p-value for cotton in Weswood was significant. Overall the GPR performed better in the Weswood plots. The main reason for this may be due to the lower amount of attenuation occurring in the Weswood as shown in the conductivity values collected from each plot. This is due to the near linear relationship between conductivity and the attenuation coefficient. Also, of note is that "better" results were obtained for tap-root cotton as opposed to fibrous-root corn, which is the opposite of what was seen in the boxes, where fibrous-root sorghum provided better results than tap-root cotton. However, this latter result was consistent with the conductivity values associated with the cotton plants in the field being lower than those for the corn plants in the field in all but one condition.

The results of the SBW analysis indicate that in Weswood soil across all dates that the SBW values at both the 90% and 95% points for corn were as predicted less than that for cotton except for the July measurement date. Recall that the field measurement dates are staggered with regards to plant type, where for corn, measurements were conducted in May, June and July, but for cotton measurements were conducted in June, July and August. It is not clear why the July measurement date was out of line. The results for Yahola soil indicate that the SBW values at both the 90% and 95% points for corn were less than that for cotton across all measurement dates. The associated p-values were found to be significant when the May and June corn values were compared with all of the cotton values on a date-by date basis, and when the July corn date

value was compared with the June cotton date value. The only two combinations that weren't significant were the July corn date compared with the July and August cotton dates. Thus, with regards to the SBW analysis, Yahola soil was found to provide results that were "better" than those obtained in Weswood soil, which is opposite to what was found for the energy analysis.

The mixed results of both types of analysis reinforce the complexity of the problem at hand. Attempting to infer the electrical properties of sub-surface reflections via external GPR measurements is a classical inverse-scattering problem that is known to be ill-posed and therefore difficult to solve. As stated in the box experiment discussions, this application for GPR is relatively new and no specific guidelines exist as to what GPR parameters should be utilized, and on what signal processing techniques would produce the best results. Instead, at this point in development it is a trial and error approach to find the right type, amount and combination of parameters that need to be used. Uncontrollable environmental conditions most likely also played a role in disrupting the results. Weed overgrowth, weather events and plant density all have the potential to influence the GPR signal.

CHAPTER V

SOIL ORGANIC CARBON

5.1 Introduction

Soil organic carbon (SOC), distinct from atmospheric or vegetative carbon, comprises the largest reservoir of terrestrial carbon (Jobbágy et al., 2000). The carbon in the global soil reservoir acts as both source and sink for atmospheric carbon and plays a major part in maintaining the equilibrium of gains and losses in the global carbon scale (Stockmann et al., 2013). Soil acts as a sink by carbon sequestration. This process can help to balance fossil fuel emissions and increase agricultural productivity (Lal, 2004). Additionally, soil acts as a source by releasing carbon into the atmosphere, such as methane from melting permafrost in the Arctic Circle (Tarnocai et al., 2009). Development of means to measure SOC rapidly and nondestructively can provide information on sequestration potential, soil health, and help maintain long-term, viable agricultural practices. Advances have been made in recent years to digitally map SOC on the global scale, however, at the field scale, tools are lacking to ground truth large-scale SOC estimates rapidly and nondestructively. Current technologies typically consist of collecting a soil core to send back to the lab for combustion analysis which results in the destruction of the sample.

Similar to the technique of phenotyping roots, GPR has the potential to detect and differentiate between different amounts of SOC. The amount of soil organic carbon strongly influences the amount of water contained within a soil. As previously discussed, this change in water content leads to changes in relative permittivity. Changes in relative permittivity is one of

the main drivers influencing the propagation of a GPR signal. These changes in the GPR signal can be quantified and related back to a water content. It is this relationship between soil moisture and a GPR signal that can be exploited to indirectly detect the changes in SOC. The objective of this chapter was to quantify the impact of SOC on GPR signal.

5.2 Methods

Three sites were selected in three different states to represent different SOC levels; Texas, Arkansas, and Wisconsin. The first site selected was in Arlington, WI at the Arlington Agricultural Research Station run by the University of Wisconsin-Madison. This site was on a Plano silt loam (fine-silty, mixed, superactive, mesic Typic Argiudolls). The Wisconsin site represented the highest carbon levels of the three sites with an average soil organic carbon content of 2.5%. The second site selected was in Mariana, AR at the Lon Mann Cotton Research Station run by the University of Arkansas. This site was on a Calloway silt loam (Fine-silty, mixed, active, thermic Aquic Fraglossudalfs). The Arkansas location was selected as a mid-range soil organic carbon content with an average soil organic carbon content of 1.2%. The final site selected was Lamesa, TX run by Texas A&M Agrilife Research and Extension. This site was on an Amarillo fine sandy loam (fine-loamy, mixed, superactive, thermic Aridic Paleustalfs). The Texas location represented the lowest SOC content with average content of 0.2%. In addition to attempting to capture the greatest range of SOC possible, these three locations were selected because they have similar soil textures and mineralogical backgrounds. Having similar characteristics and backgrounds between sites can help rule out other potential factors that could be altering the GPR signal between locations. GPR transects were run across multiple plots with different historical uses at each location. The length of each transect varied at each location but

each was at least 4-meters. At the time of each survey no plants were present on any of the plots. In Wisconsin two different fields sites with multiple sub-plots at each location were scanned for a total of 39 plots. At Arkansas 48 plots were scanned and in Texas 9 different plots were scanned. The GPR selected was the IDS Hi-Mod operating at two frequencies, 400 and 900MHz. Figure 1A is a picture of the GPR unit used. Unlike the Sensor's and Software unit, the IDS GPR transmitting and receiving antenna are housed within the same enclosure with a fixed separation and cannot be moved independently. The IDS GPR had a spatial sampling frequency of approximately one per 3.5 cm and 1.75 cm for 400 MHz and 900 MHz, respectively, both of which were controlled by a calibrated odometer attached to the wheel. This means that at every 1.75 cm centimeter increment the 900 MHz transmitting antenna automatically emitted a pulse, while at every 3.5 cm the 400 MHz transmitting antenna automatically emitted a pulse. Several issues were encountered using the IDS Hi-Mod GPR. First, several of the plots, mainly in Arkansas, had a large amount of crop residue left after harvesting. This excess ground cover has the potential to interfere with the portion of the GPR signal under investigation. Similarly, at the Wisconsin location the terrain was very uneven, and caused the GPR to bounce as it was pushed along the transect. This unwanted movement could also be detrimental to GPR data and needs to be taken into consideration. The uneven terrain at these sites coupled with the increased mobility of the wheeled assembly made it impossible to employ the stacking signal option, which we were able to use with the Sensor's and Software unit to increase signal to noise ratio, see section 1.3. Figure 35 shows pictures of example plots from all three locations. In the pictures you can see the different types of ground conditions and cover encountered. Lubbock had the conditions most conducive for GPR data collection, however, even there the minimal amount of cotton residue could impact the signal. Since there were no intervening plants in all of these sites, the

conventional common offset configuration could be used where the Tx and Rx antennas are offset in the direction of travel.

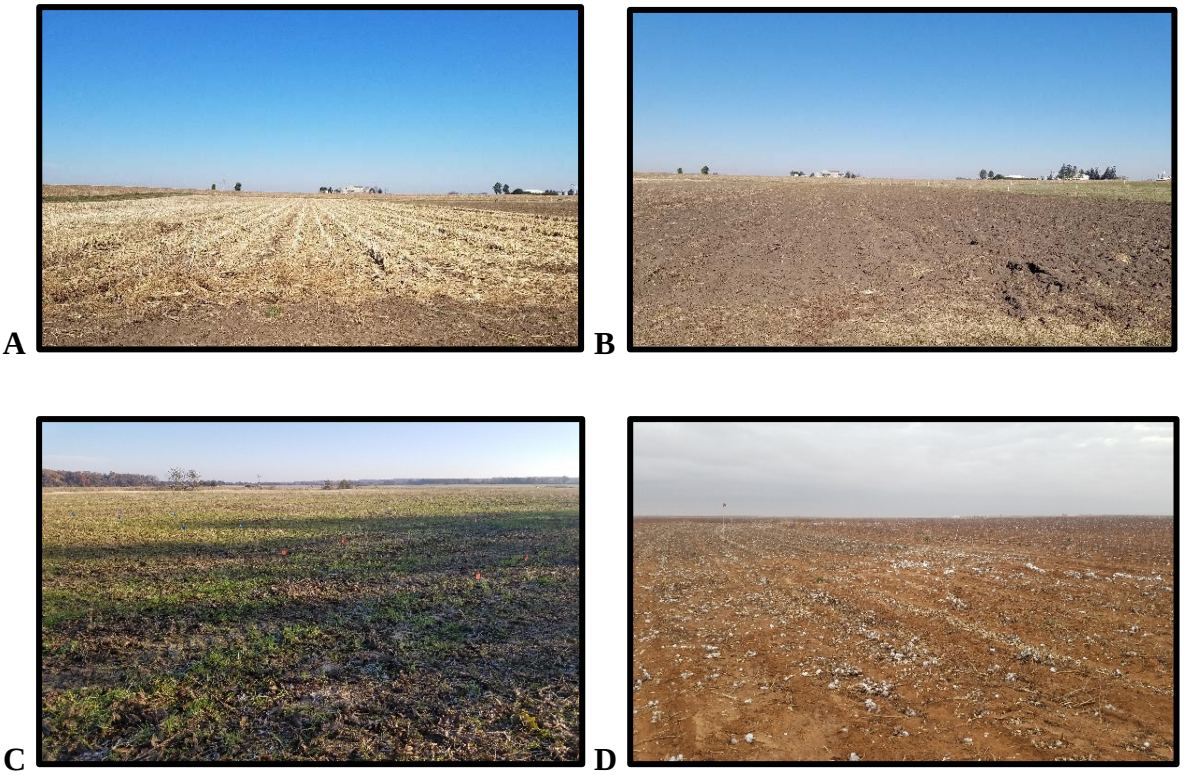

Figure 35: Different field conditions. (A) Arlington, Wisconsin. (B) Arlington, Wisconsin. (C) Mariana, Arkansas. (D) Lamesa, Texas.

In addition to collecting GPR data, at the time of each survey surface soil moisture measurements were taken using the Dynamax TH20 soil moisture probe. Surface soil moisture measurements were taken at the Arkansas and Texas locations; however, the device was not available at the Wisconsin site and soil moisture measurements had to be estimated. This was

done using the data collected by using a statistic known as the average envelope amplitude (AEA). AEA is a measure of the early time signal (ETS) portion of a GPR signal trace and was calculated by determining the average of the signal envelope over a specified time window.

The AEA was utilized for calculating an estimate of the water content in Wisconsin because it has been shown by Comite et al., 2014 and Pettinelli et al., 2007 to be related to changes in relative permittivity and conductivity. In order to generate the Wisconsin water content data, the AEA of the first positive half cycle of every GPR trace collected in Wisconsin was calculated. From those AEA values the relative permittivity could then be estimated using Equation 17.

$$\varepsilon_r = 1 + 1/(c\overline{AEA}2\pi\varepsilon_0\Delta x^2) \tag{17}$$

The overbar in Equation 17 implies taking the mean of all of the AEA measurements. Since Δx varied with the frequency, two estimates of ε_r were developed, one for 400 MHz and one for 900 MHz. The relationship between AEA and relative permittivity was calibrated using the data collected from Arkansas where the soil volumetric water content measurements were taken with the theta probe. This calibration was taken into account by multiplying Equation 17 by a calibration factor, where a different factor was developed for each frequency. The volumetric water content could then be calculated via Topp's Equation (Equation 5).

After data collection, two different statistics were used to determine if there was a relationship between changes in SOC content and changes in the GPR signal. These statistics were: integrated pixel magnitude (IPM) and energy per trace spatial mean (EPTSM). These types of statistics are desirable in this situation because these forms of analysis do not require the presence of subsurface reflectors (Pettinelli et al., 2007). Additionally, the specific calculation of

each of these statistics focuses on the beginning of the GPR signal which corresponds to the shallow depths where SOC is most likely to accumulate and where changes will be most noticeable. The integrated pixel magnitude was calculated after the raw B-scan was processed and run through the Stolt migration algorithm. Formally, the IPM was the summation of the pixel magnitude, i.e. the absolute value of pixel values over the transect length (4 m) and depth of interest (0-15 cm) multiplied by the step size in the x and z directions. The step size in the x direction is the space between traces along the transect and is a set parameter in the GPR equipment, and as noted above varies with the Tx frequency for the IDS unit used in these measurements. The step size in the z direction was artificially generated within the Stolt migration algorithm and is proportional to the velocity of the EM wave in the soil divided by the bandwidth of the Tx pulse. A graphical representation of IPM can be seen in Figure 36A where the pixels shown in red are assumed to extend the length of the transect. The second test statistic was energy per trace spatial mean (EPTSM), which is developed by first calculating the energy per trace over the time period corresponding to the depth of interest for each trace, and then taking the average of these values over all traces along the transect. Figure 36B shows the selection of the samples of interest (red dots) used to calculate the energy per trace for a given trace. Both statistics were compared to carbon data collected within different plots at each location and between average carbon percentages between different locations.

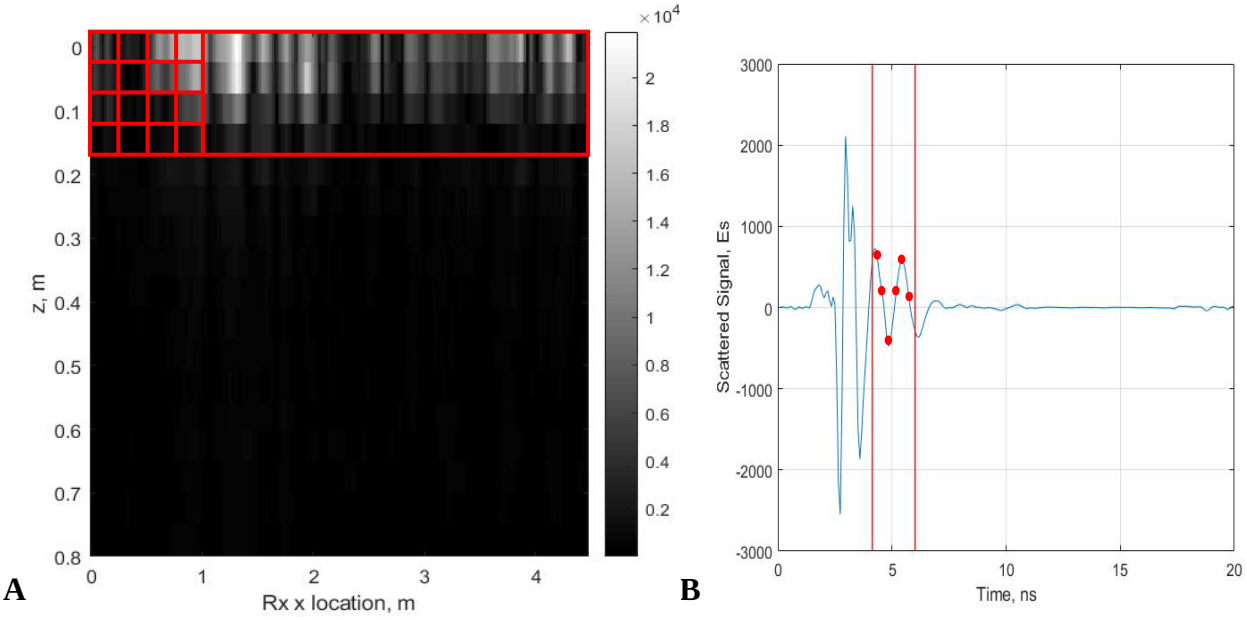

Figure 36: Different analysis types. (A) Integrated pixel magnitude. (B) Energy per trace spatial mean.

5.3 Results

The hypothesis was that there should be a positive relationship between SOC level and both of the measured statistics at both frequencies. GPR has previously been tested as tool for measuring soil moisture content and different methods exist that relate various calculations derived from a GPR signal back to soil moisture content with a positive correlation (Huisman et al., 2003). This relationship can be indirectly extended to the measurement of SOC content due to the fact that as SOC increases in the top portion of the soil, the water holding capacity of that section also increases, and therefore, a higher signal return would be expected resulting in an indirect measure of SOC. IPM and EPTSM are tools to measure the intensity of the first portion of the returned signal. The first set of results compare the calculated IPM and EPTSM of each individual plot with their respective SOC content within a single state location. Figures 37A, B

and C show a comparison of the IPM at 900 MHz with the percentage SOC level for each of the three sites. Figure 37A is for data collected from the 9 plots located in Texas which had the lowest SOC values (0.13-.0.31% SOC). In this figure we see the opposite of the expected trend with an R^2 value of 0.43, and a statistically insignificant p-value of 0.055. Figure 37B is for the data collected from the Arkansas location which had the mid-range of soil organic carbon values (0.831-1.82% SOC). In this figure we see a small positive relationship between the IPM and SOC percentages with a R^2 of 0.009 and corresponding p-value of 0.507, which does not indicate a statistically significant relationship between the two. Finally, Figure 37C is for the data collected from Wisconsin which had the highest values of SOC (1.907-3.178% SOC). In this figure, the data has a slightly larger positive relationship with an R^2 of 0.02. However, like the Arkansas data this relationship is not statistically significant with a p-value of 0.357, and no conclusions can be confidently drawn from it.

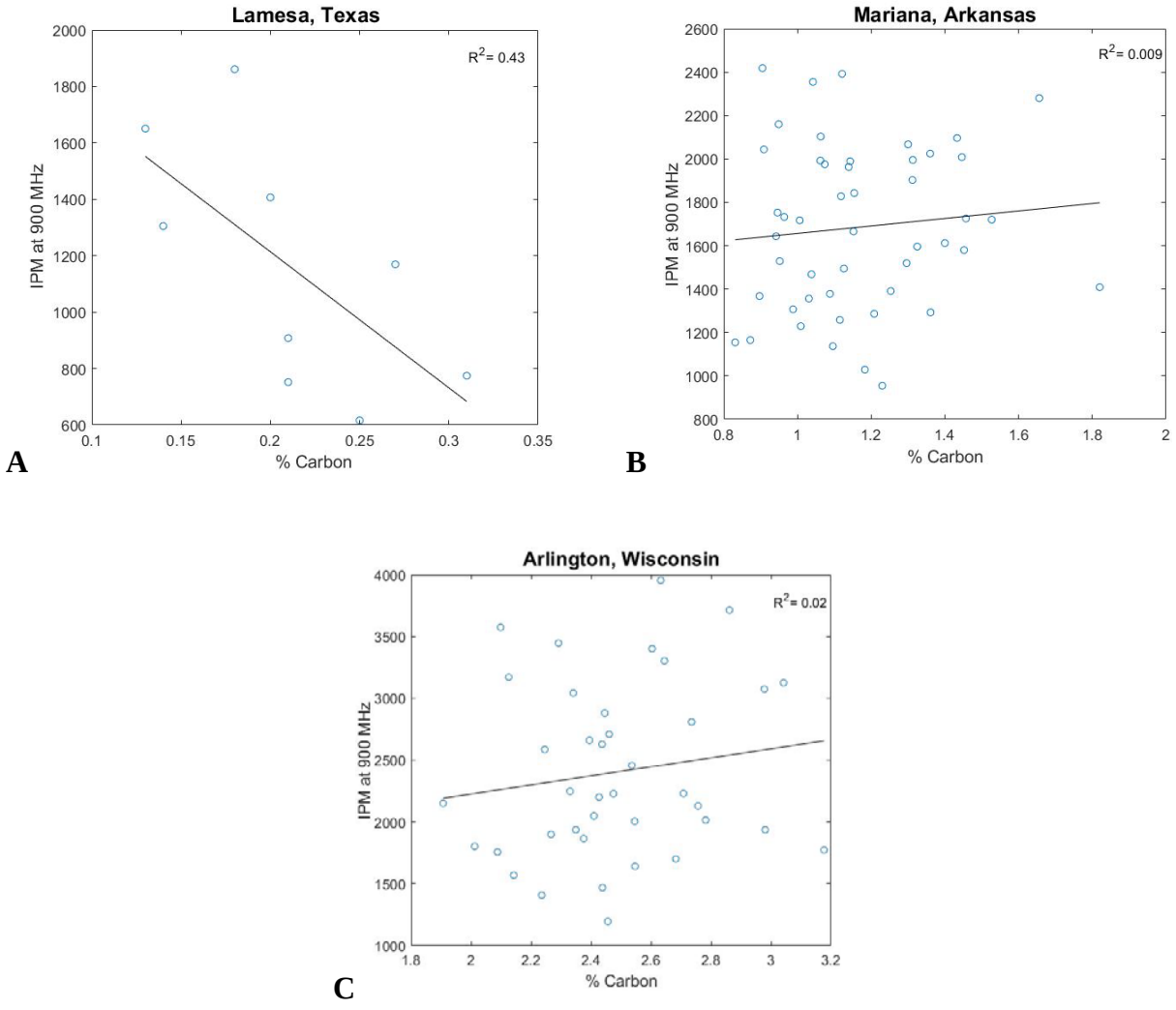

Figure 37: Comparison of percent carbon and IPM at 900 MHz at the three different locations. (A) Lamesa, TX. (B) Mariana, AR. (C) Arlington, WI.

Additionally, the comparison between EPTSM and SOC percentage yielded even less conclusive results than the comparison with the IPM. In these specific conditions, the GPR does not appear to be able to detect the small-scale, plot to plot differences in SOC. This may be due to the spatial heterogeneity of ground cover and topography. Another point is that all the graphs show only the 900 MHz results. The 400 MHz data was also less conclusive with smaller relationships between the values. As the frequency of the GPR signal decreases, the greater the depth penetration but at the cost of image resolution. This is desirable in situations where the goal is to observe larger objects buried at greater depths. In the scenario of trying to observe small-scale near surface changes in soil organic carbon, the 400 MHz signal may miss any potential changes at shallow depths.

To summarize, Table 10 shows the R values and associated p-values for the different comparisons between SOC and EPTSM and IPM at the two different frequencies for the plot to plot comparisons within each location. Table 10 also lists the "partial" correlation coefficients and associated p-values. The partial correlation coefficient was determined by comparing two variables, in this case SOC and either IPM or EPTSM, while holding a third variable, in this scenario, soil moisture content, constant. The soil water content is not solely controlled by SOC, instead it is influenced by a variety of other soil characteristics and environmental conditions. By holding the soil moisture content constant, we can take into consideration changes in soil moisture content that are not a result of changes in SOC but instead by other confounding variables. We can then test if changes in the GPR signal can be related back to the small-scale variations in the SOC or if the signal is controlled by another factor's influence on soil moisture content. The partial correlation had the greatest impact on the Wisconsin data and resulted in

statistically significant correlations for both the IPM and EPTSM at 900 MHz. Additionally, the relationship between IPM at 900 MHz and SOC in Lubbock also yielded a statistically significant result, however this relationship was still negative which was the opposite of the expected results.

Table 10: Different correlation coefficients with associated p-values and partial correlation coefficients and p-values for three different locations.

	IPM @ 400 MHz	IPM @ 900 MHz	EPTSM @ 400 MHz	EPTSM @ 900 MHz
	Wisconsin			
R	0.1361	0.1514	0.0593	0.2519
p	0.4088	0.3575	0.72	0.1218
Partial R	0.2123	0.3469	0.0366	0.3853
p for partial R	0.2006	0.0329	0.8272	0.0169
	Arkansas			
R	0.0389	0.0981	0.0375	-0.0421
p	0.7929	0.5071	0.8003	0.7764
Partial R	0.0154	0.1268	0	-0.0574
p for partial R	0.9181	0.3958	0.9999	0.7014
	Texas			
R	-0.2172	-0.6557	-0.35	-0.4486
p	0.5745	0.0552	0.3558	0.2258
Partial R	-0.1345	-0.7169	-0.299	-0.4309
p for partial R	0.7508	0.0454	0.4719	0.2866

The next step in the analysis was to compare average data between states to test if the GPR signal was influenced by larger scale changes in SOC. This was done by first calculating the average IPM and EPSTM across all plots within a given state location for the both the 400 and 900 MHz. Next, the average SOC for each state was calculated and found to be 0.2%, 1.2%, and 2.5% in Texas, Arkansas, and Wisconsin, respectively. Figure 38A and 38B compare the mean energy per trace spatial mean (MEPTSM) for each state to the mean carbon percentage for 400 and 900 MHz respectively. The expected result in this scenario would also be a positive linear relationship between the two statistics and SOC, with the lowest value being from Texas, middle from Arkansas and highest from Wisconsin with increasing soil organic carbon. In Figure 38A with the 400 MHz Tx, the expected results were not observed. Instead, the middle Arkansas value has the highest MEPTSM instead of Wisconsin with an overall $R^2 = 0.376$. As mentioned earlier, 400 MHz may not be the ideal frequency since its associated wavelength may not provide the image resolution needed to detect small scale changes at the near surface level. However, in Figure 38B which compares the data collected at 900 MHz we see the expected positive relationship between MEPTSM and the SOC with an $R^2 = 0.987$. The next set of Figures in 38C and 38D continue to compare the average SOC of each state but now with the mean integrated pixel value or MIPM. In this case we see a positive relationship at both the 400 and 900 MHz frequencies with R^2 values of 0.893 and nearly 1 (0.999998), respectively. Again the 900 MHz has a stronger relationship as opposed to the 400 MHz. The 900 MHz comparison nearly has a straight-line linear relationship between the average SOC content and the MIPM.

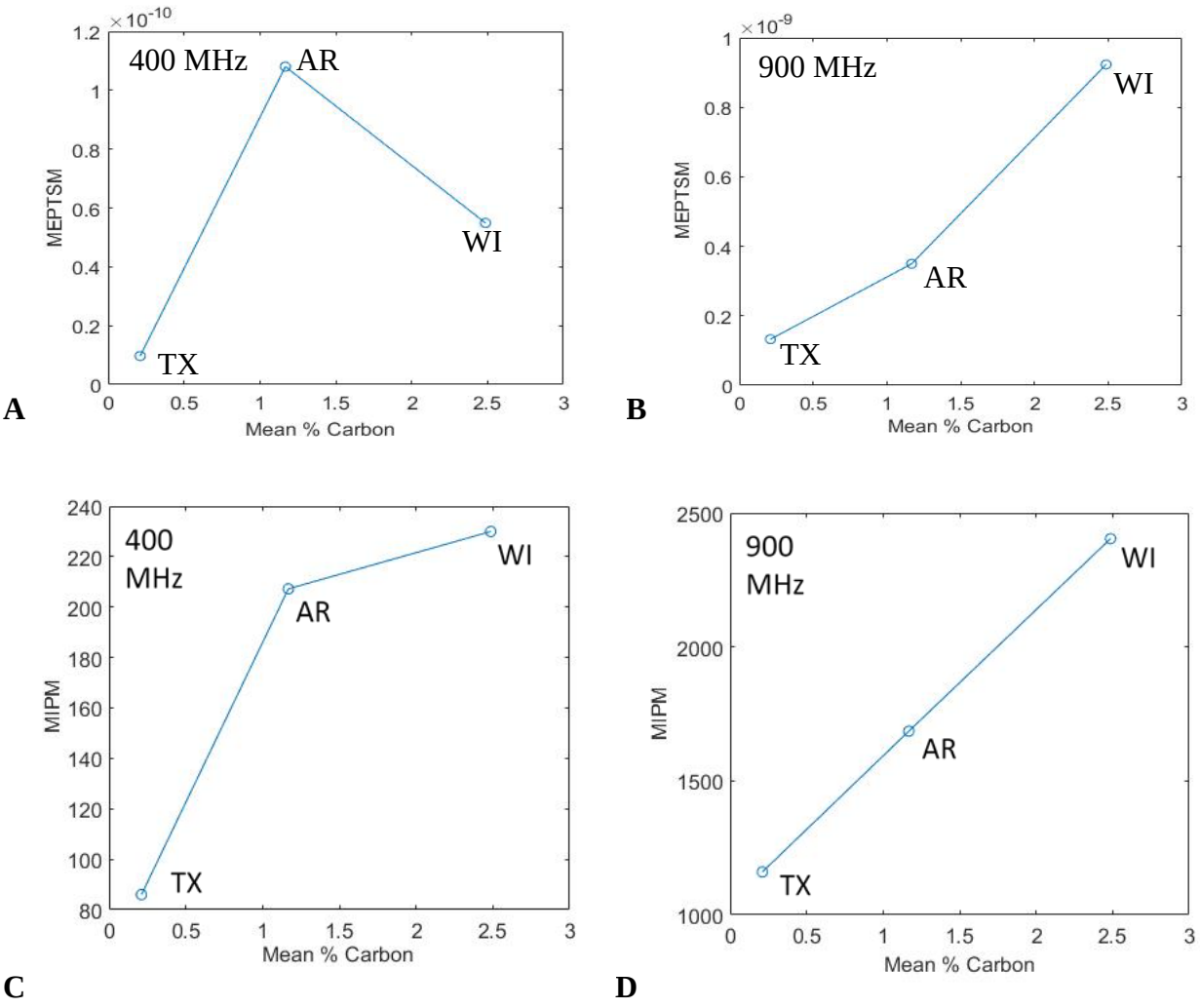

Figure 38: Comparison of average carbon percentage and mean integrated pixel magnitude and mean energy per trace spatial mean. (A) Mean % carbon and MEPTSM at 400MHz. (B) Mean % carbon and MEPTSM at 900 MHz. (C) Mean % carbon and MIPM at 400 MHz. (D) Mean % carbon and MIPM at 900 MHz.

A critical parameter in these comparisons is the spatial filter width associated with the localized background calculation, see discussion on background removal in section 1.3.1. By changing the spatial filter width the significance of the relationships between SOC and MEPTSM and MIPM can be shifted. Figure 39 shows the sensitivity to spatial filter width for

both statistics at 900MHz. For MEPTSM the p-value tends to decrease with increasing values of spatial filter width, but at no value is it ever statistically significant. However, for the MIPM, there is a clear optimum value at a spatial filter width of 1.5 m, with significant p-values over a fairly wide range of values. Thus, 1.5m was the value used for the spatial filter width in the analysis described above comparing the average statistics across sites.

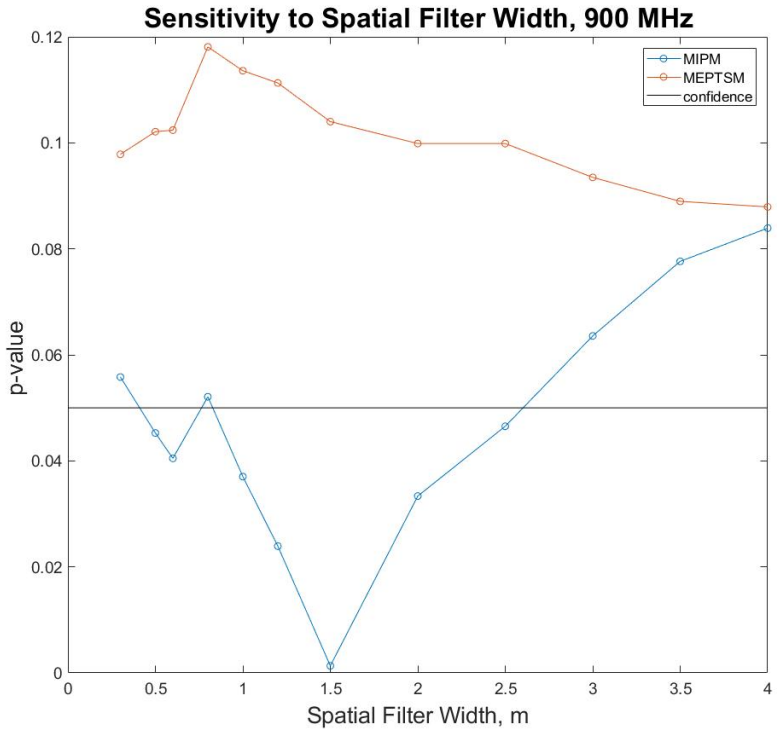

Figure 39: Sensitivity of p-value to spatial filter width for MIPM and MEPTSM at 900 MHz.

5.4 Summary

GPR's ability to detect variations in soil moisture content made it a viable tool to be explored as a means to indirectly measure SOC in the field. A majority of the current technologies utilized to measure SOC are time-consuming and destructive. GPR could provide a means to quickly and non-destructively measure SOC indirectly in the field. A change in SOC levels results in changes in the soil moisture content of the soil, most notably in the top portion of the soil profile. GPR could potentially indirectly measure SOC by detecting the small-scale differences in soil moisture content induced by changes in SOC. At the Arkansas and Wisconsin locations no relationship was observed between SOC with IPM collected at 900 MHz. At the Texas location only a weak negative linear relationship was observed with the 900 MHz IPM. The results from 400 MHz IPM and from both frequencies of the EPTSM resulted in even less conclusive results at all three locations. A partial correlation analysis was also run between the SOC levels and the two statistics. This type of analysis allows us to hold a third variable constant, in this case soil moisture content, and test the relationship without its influence. The results of this analysis yielded significant results for the IPM and EPTSM at 900 MHz for the Wisconsin data, whereas the results for the conventional correlation analysis did not. In addition, the analysis yielded a significant result for the IPM at 900 MHz for the Texas data, whereas the conventional analysis did not. In summary, the above results indicate the GPR could not detect the small-scale differences noted between plots which is likely due to the spatial heterogeneity of ground cover and terrain between plots which caused uneven signal disruption across the GPR transects at these locations.

The next analysis step was to compare the average results between states. The comparison of the mean EPTSM and mean IPM at 900 MHz generated graphs with strong positive linear relationships. The comparisons at 400 MHz were not as meaningful, although the mean IPM was consistent with the expected trend, but not in a linear fashion. The results for 900 MHz indicate that GPR can potentially detect larger scale differences in SOC. As noted, the frequency of the GPR unit plays an important role in its ability to detect differences in SOC. Specifically, the higher 900 MHz frequency generated more conclusive results than the lower 400MHz. This is likely due to the fact that at lower frequencies the depth of signal penetration was greater, but the resolution of a generated image was lower. The 900 MHz, with its high image resolution capabilities, is more likely to capture SOC variations in the top portion of the soil.

As in the case of using GPR as a tool for root phenotyping, it cannot be conclusively said that GPR can be used as a tool for measuring SOC in the field. This experiment was one of the first of its kind to explore this potential application of GPR, and more work needs to be done to test its feasibility. Data across a wider range of SOC levels with consistent measurements of soil electromagnetic properties (relative permittivity and conductivity) under a range of soil types and conditions would aide in determining GPR's usefulness as a tool for measuring SOC. Finally, as with root phenotyping at finer scales, there are no standard procedures set as to what post processing and analysis techniques would be best suited in this application. Other types of signal processing, amounts and with different parameters may yield more definitive results in future studies.

CHAPTER VI

CONCLUSIONS

The ability to phenotype roots rapidly and nondestructively can provide valuable information to plant breeders. It can help increase plant productivity, enhance the potential for C sequestration through the incorporation of root biomass into the soil, and improve water use strategies. Ground penetrating radar with its ability to detect small scale differences in relative permittivity as controlled by soil moisture content and conductivity, could be a potential tool to supplement current phenotyping technologies. The goal of this project was to link GPR data with soil electromagnetic properties to enhance GPR performance while conducting preliminary tests to assess the ability of GPR to be utilized as a tool for root phenotyping at the fine root scale. The results in this thesis can help lay a groundwork for future experimental models and can be expounded upon in greater detail.

In Chapter II of this thesis, three GPR modeling exercises were described, two of which were based upon the use of an open source EM wave simulator specifically developed for GPR applications, gprMax. The different modelling applications indicated that it is feasible, in highly controlled, idealized environments for GPR to be used as a root phenotyping tool. Additionally, the simulations showed the importance and viability of using certain processing techniques. One of the main issues often confronted in novel techniques using GPR is the selection of which post-processing techniques to use. In this thesis, Stolt migration algorithm was examined and later shown to be a viable tool to aide in root detection and visualization. Two types of analysis were also tested, energy and SBW, to examine GPR's root detection and differentiation abilities.

Overall, each of these applications showed the importance of different aspects of GPR processing and the significance of taking into consideration how the parameters of the anomaly, i.e. roots, being visualized and the surrounding soil electromagnetic parameters effect GPR's ability to be used as an effective tool.

In Chapters III and IV the controlled and field experiments that were set up to test the feasibility of GPR in close to ideal and in situ conditions were described. In the controlled experiment multiple tests were run to test methodologies that could aide in using GPR as a potential tool for root phenotyping. Of note was the use of a GPR configuration, which we refer to as perpendicular common offset. In this configuration, the offset between the transmitting and receiving antenna is perpendicular to the direction of travel of the GPR unit, whereas in the conventional common offset configuration the separation is in the same direction. In the conventional common offset technique, the receiving and transmitting antenna must remain on the same side of a plant being scanned, while in the perpendicular common offset configuration it is possible to place the two antennas on opposite sides of a plant which could potentially enhance root detection.

In the controlled experiments, cotton and sorghum plants and objects were placed in bags (boxes) filled with either sand or Yahola soil. The boxes were used to test the validity of the results obtained in Chapter II from the GPR modelling and analysis scenarios. Specifically, looking at changes in energy and SBW to indicate the presence or absence of roots and whether or not a difference in a tap or fibrous root could be identified. Results were often mixed depending on the analysis and the soil type under investigation. This reinforces the idea that even in controlled, ideal conditions it is important to account for changes in soil type and its varying

conditions (e.g. relative permittivity and conductivity) in the observed study area. Typically, GPR is known to work best in dry, sandy conditions, which in most cases of the controlled experiment held true. However, even in the ideal conditions of the boxes, GPR was not always be successful at detecting and visualizing differences in roots. Inherent and environmental limitations exist that cannot always be overcome and must be taken into consideration. The box experiments also demonstrated that it was important to take into consideration not just the large-scale difference in soil properties seen in between different soil series but the small-scale variations in soil properties that are observed with depth. It is important to integrate these changes into the post processing schemes to obtain a more accurate representation of the soil subsurface and how it impacts the propagation of the GPR signal.

In Chapter IV the results for the field experiments conducted in 2018 were described. The field experiments conducted in 2017 in Thrall and Lubbock did not yield reliable results, most likely due to the soil conditions at both locations. This reinforces the theory that soil conditions must be taken into consideration when using GPR in this type of application. However, they did lay the groundwork for the test methodology that was improved upon in 2018. The 2018 field data was analyzed in the same manner as the box data by examining changes in energy between non-plant and plant locations and comparing the SBW between fibrous and tap roots. Similar to the box results, the results were often inconclusive and depended on soil characteristics and other environmental parameters. For example, it was found that in the energy analysis, the Weswood soil yielded ‘better’ results as opposed to the Yahola soil. One potential reason that GPR performs better in Weswood compared to Yahola is due to the lower signal attenuation associated with the Weswood soil which is mainly controlled by the conductivity of a given soil. However, in the SBW analysis ‘better’ results were obtained in the Yahola soil giving mixed

results overall. As is in the box experiments, the mixed results demonstrate the importance and influence of the soil properties on GPR's ability to detect and differentiate roots. Additionally, it shows the various limitations associated with GPR and how a variety of factors can confound GPR's ability to detect and distinguish roots.

In addition to the importance of the soil properties, there are a number of potential reasons for the observed mixed results encountered throughout this project. First and foremost is just how difficult and complex a problem it is to use GPR in this fashion. In the context of image recovery, the electrical characteristics (relative permittivity and conductivity) of objects within the soil are inferred from externally gathered GPR measurements aided by EM-38MK2, NMM, and theta probe measurements. This is a classical inverse scattering problem, which is typically ill-posed, which implies that any error made in the assumptions, e.g. background removal in the development of the scattered signal, will tend to induce a large amount of error in the image recovery process. In addition, there is a need for further refinement of the post processing techniques used. As a still maturing technology, there are no standard operating procedures on how to post process the GPR data. Finding the right processes, which combination of processes, what values to set parameters within the processes, and in what order to use them all impact the overall effectiveness and can alter results. Having too little post processing can cause the desired results to be masked and lost in the data. However, using too much post processing can alter the data too far and move towards the manipulation of information to generate the desired results. As well, inherent limitations exist within the current signal processing. For example, the w-k_z conversion that is integral to Stolt w-k migration is such that low spatial frequencies in the z dimension are not recoverable. This leads to image distortion along the z-axis where in the end

the processing is only able to detect the edges of an object corresponding to the higher spatial frequencies.

Additionally, there are a number of other parameters that can be altered within the GPR hardware and software that could potentially enhance GPR's functionality in this application. These include but are not limited to: changing the antenna type, increasing or decreasing the operating frequency, and altering the specific survey parameters such as antenna separation or step size. Also, only two types of analysis were examined in this thesis. Other means of comparison, such as examining ground root biomass, could be explored as a means to measure changes in root characteristics. Finally, certain environmental conditions encountered in the controlled and field experiments hindered results. For example, the overgrowth of weeds and uncontrolled rain events made ground truthing impossible.

Overall, it cannot be said one way or another if GPR can be used a tool for fine root phenotyping from this research. This research instead shows the importance of incorporating the electromagnetic properties of the soil into the processing of GPR data and that more research needs to be conducted. The above experiments could provide a groundwork and act as a stepping stone to help determine the feasibility of GPR as a phenotyping tool.

Finally, this thesis also looked at the ability of GPR to be used as a tool for detecting and quantifying soil organic carbon with results presented in Chapter V. SOC data can provide information to help increase plant productivity, maximize carbon sequestration potential and improve water use strategies. However, similar to root phenotyping, the agriculture discipline lacks a tool to rapidly and nondestructively quantify SOC in the field. Increased SOC is known to cause a subsequent increase in water infiltration and retention in the surface soil and thus,

GPR could act as a potential tool for indirectly detecting small scale changes in SOC by detecting the changes in soil moisture content caused by changes in SOC levels. To provide a reasonable range of SOC levels, three sites were selected across the United States at which GPR measurements were taken at 400 and 900 MHz. Two statistics, integrated pixel magnitude and energy per trace spatial mean, were developed specifically for this application to compare with the SOC levels. The first comparison made was between plots within the same locations. In this scenario the relationships varied greatly from state to state. This was likely due to the spatial heterogeneity of the ground cover and terrain between plots that influenced the GPR signal. In the comparison between states a strong positive linear relationship was observed between the average value of the two statistics across all of the plots at a given site and the average SOC. As in the root phenotyping portion of this thesis, the results for SOC quantification were mixed. In certain scenarios, i.e. where contrast in SOC were larger, GPR appeared to have the potential to detect differences in SOC levels, however at the smaller scale between plots, GPR failed to detect any differences in SOC. As a novel technique for GPR, the ability to quantify SOC is still unclear. Additional experiments across a variety of soil types and SOC levels are required to be able to state if GPR could be used as a SOC quantification tool. As in root phenotyping, the type of and amount of post-processing required is still under-development and changing soil parameters across a landscape and within a soil profile must be taken into consideration in order confidently state whether GPR can successfully quantify SOC.

REFERENCES

Adamchuk, V.I., J.W. Hummel, M.T. Morgan and S.K. Upadhyaya. 2004. On-the-go soil sensors for precision agriculture. Comput. Electron. Agric. 44:71-91

Algeo, J., R.L. Van Dam and L. Slater. 2016. Early-time GPR: A method to monitor spatial variations in soil water content during irrigation in clay soils. Vadose Zone Journal 15.

Algeo, J., L. Slater, A. Binley, R.L. Van Dam and C. Watts. 2018. A comparison of ground-penetrating radar early-time signal approaches for mapping changes in shallow soil water content. Vadose Zone Journal 17.

Annan, A.P. 2002. GPR—History, trends, and future developments. Subsurface Sensing Technologies and Applications 3:253-270.

Annan, A.P. 2005. Ground-penetrating radar. p. 357-438. *In* Near-surface geophysics. Society of Exploration Geophysicists,

Annan, A.P. 2009. Chapter 1 - electromagnetic principles of ground penetrating radar. p. 1-40. *In* H.M. Jol (ed.) Ground penetrating radar theory and applications. Elsevier, Amsterdam.

Arjwech, R., M.E. Everett, J. Briaud, S. Hurlebaus, Z. Medina-Cetina, S. Tucker and N. Yousefpour. 2013. Electrical resistivity imaging of unknown bridge foundations. Near Surface Geophysics 11:591-598.

Atkinson, J.A., A. Rasmussen, R. Traini, U. Voß, C.J. Sturrock, S.J. Mooney, D.M. Wells and M.J. Bennett. 2014. Branching out in roots: Uncovering form, function and regulation. Plant Physiol.pp. 114.245423.

Barton, C.V. and K.D. Montagu. 2004. Detection of tree roots and determination of root diameters by ground penetrating radar under optimal conditions. Tree Physiol. 24:1323-1331.

Benedetto, A., F. Tosti, L.B. Ciampoli and F. D'Amico. 2017. An overview of ground-penetrating radar signal processing techniques for road inspections. Signal Process 132:201-209.

Butnor, J.R., J.A. Doolittle, L. Kress, S. Cohen and K.H. Johnsen. 2001. Use of ground-penetrating radar to study tree roots in the southeastern united states. Tree Physiol. 21:1269-1278.

Butnor, J.R., J.A. Doolittle, K.H. Johnsen, L. Samuelson, T. Stokes and L. Kress. 2003. Utility of ground-penetrating radar as a root biomass survey tool in forest systems. Soil Sci. Soc. Am. J. 67:1607-1615.

Cassidy, N.J. 2009. Ground penetrating radar data processing, modelling and analysis. Ground Penetrating Radar: Theory and Applications141-176.

Chanasyk, D.S. and M.A. Naeth. 1996. Field measurement of soil moisture using neutron probes. Can. J. Soil Sci. 76:317-323.

Clark, R., R. MacCurdy, J. Jung, J. Shaff, S.R. McCouch, D. Aneshansley and L. Kochian. 2011. 3-dimensional root phenotyping with a novel imaging and software platform. Plant Physiol.pp. 110.169102.

Comas, L., S. Becker, V.M.V. Cruz, P.F. Byrne and D.A. Dierig. 2013. Root traits contributing to plant productivity under drought. Frontiers in Plant Science 4:442.

Daniels, D.J., D.J. Gunton and H.F. Scott. 1988. Introduction to subsurface radar. p. 278-320. *In* Introduction to subsurface radar. IEE proceedings F (communications, radar and signal processing), 1988. IET.

Daniels, D. J., Daniels, D. J.,Institute of Electrical Engineers, 2004. Ground penetrating radar. Institution of Electrical Engineers, London.

Davis, J.L. and A.P. Annan. 1989. Ground-penetrating radar for high- resolution mapping of soil and rock stratigraphy 1. Geophys. Prospect. 37:531-551.

Doolittle, J., M. Petersen and T. Wheeler. 2001. Comparison of two electromagnetic induction tools in salinity appraisals. J. Soil Water Conserv. 56:257-262.

Doolittle, J.A. 1982. Characterizing soil map units with the ground-penetrating radar. Soil Horizons 23:3-10.

Doolittle, J.A. and M.E. Collins. 1995. Use of soil information to determine application of ground penetrating radar. J. Appl. Geophys. 33:101-108.

Doolittle, J.A., F.E. Minzenmayer, S.W. Waltman, E.C. Benham, J.W. Tuttle and S.D. Peaslee. 2007. Ground-penetrating radar soil suitability map of the conterminous United States. Geoderma 141:416-421.

Doolittle, J.A. and E.C. Brevik. 2014. The use of electromagnetic induction techniques in soils studies. Geoderma 223:33-45.

Everett, M.E. 2013. Ground-penetrating radar. p. 239-278. *In* Near-surface applied geophysics. Cambridge University Press, Cambridge.

Evett, S. 2008. Chapter 3 neutron moisture meters. International Atomic Energy Agency (IAEA).

Fomel, S. 2003. Time-migration velocity analysis by velocity continuation. Geophysics 68:1662-1672.

Freeland, R.S., R.E. Yoder and J.T. Ammons. 1998. Mapping shallow underground features that influence site-specific agricultural production. J. Appl. Geophys. 40:19-27.

Gaskin, G.J. and J.D. Miller. 1996. Measurement of soil water content using a simplified impedance measuring technique. Journal of Agricultural Engineering Research 63:153-159.

Grant, D.R. 1975. Measurement of soil moisture near the surface using a neutron moisture meter. J. Soil Sci. 26:124-129.

Guo, L., H. Lin, B. Fan, X. Cui and J. Chen. 2013. Forward simulation of root's ground penetrating radar signal: Simulator development and validation. Plant Soil 372:487-505.

Hammon III, W.S., G.A. McMechan and X. Zeng. 2000. Forensic GPR: Finite-difference simulations of responses from buried human remains. J. Appl. Geophys. 45:171-186.

Hayt, W.H. and J.A. Buck. 2001. Engineering electromagnetics. McGraw-Hill New York.

Hruska, J., J. Čermák and S. Šustek. 1999. Mapping tree root systems with ground-penetrating radar. Tree Physiol. 19:125-130.

Hubbard, S., K. Grote and Y. Rubin. 2002. Mapping the volumetric soil water content of a California vineyard using high-frequency GPR ground wave data. The Leading Edge 21:552-559.

Huck, M.G. and H.M. Taylor. 1982. The rhizotron as a tool for root research. p. 1-35. *In* Advances in agronomy. Elsevier.

Iyer-Pascuzzi, A.S., O. Symonova, Y. Mileyko, Y. Hao, H. Belcher, J. Harer, J.S. Weitz and P.N. Benfey. 2010. Imaging and analysis platform for automatic phenotyping and trait ranking of plant root systems. Plant Physiol. 152:1148-1157.

Jobbágy, E.G. and R.B. Jackson. 2000. The vertical distribution of soil organic carbon and its relation to climate and vegetation. Ecol. Appl. 10:423-436.

Johnson, M.G., D.T. Tingey, D.L. Phillips and M.J. Storm. 2001. Advancing fine root research with minirhizotrons. Environ. Exp. Bot. 45:263-289.

Johnson, R.W., R. Glasscum and R. Wojtasinski. 1982. Application of ground penetrating radar to soil survey 1. Soil Horizons 23:17-25.

Jol, H.M. 1993. Ground penetrating radar (GPR): A new geophysical methodology used to investigate the internal structure of sedimentary deposits (field experiments on lacustrine deltas).

Jol, H.M. 2008. Ground penetrating radar theory and applications. Elsevier.

Lal, R. 2004. Soil carbon sequestration impacts on global climate change and food security. Science 304:1623-1627.

Lynch, J. 1995. Root architecture and plant productivity. Plant Physiol. 109:7.

Lynch, J.P. 2011. Root phenes for enhanced soil exploration and phosphorus acquisition: Tools for future crops. Plant Physiol. 156:1041-1049.

Maxwell, J.C. 1861. Xxv. on physical lines of force: Part i.–the theory of molecular vortices applied to magnetic phenomena. The London, Edinburgh, and Dublin Philosophical Magazine and Journal of Science 21:161-175.

Maxwell, J.C. 1864. On faraday's lines of force. Transactions of the Cambridge Philosophical Society 10:27.

Maxwell, J.C. 1865. VIII. A dynamical theory of the electromagnetic field. Philosophical Transactions of the Royal Society of London 155:459-512.

McCutcheon, M.C., H.J. Farahani, J.D. Stednick, G.W. Buchleiter and T.R. Green. 2006. Effect of soil water on apparent soil electrical conductivity and texture relationships in a dryland field. Biosystems Engineering 94:19-32.

McNeill, J.D. 1980. Electromagnetic terrain conductivity measurement at low induction numbers. Technical note TN-6. Geonics Limited, Ontario Canada L5T 1CS.

Neal, A. 2004. Ground-penetrating radar and its use in sedimentology: Principles, problems and progress. Earth-Sci. Rev. 66:261-330.

Noborio, K. 2001. Measurement of soil water content and electrical conductivity by time domain reflectometry: A review. Comput. Electron. Agric. 31:213-237.

Ozdemir, C., S. Lim and H. Ling. 2004. A synthetic-aperture algorithm for ground-penetrating radar imaging. Microwave Opt Technol Lett 42:412-414.

Paine, J.G. 2003. Determining salinization extent, identifying salinity sources, and estimating chloride mass using surface, borehole, and airborne electromagnetic induction methods. Water Resour. Res. 39.

Persico, R. 2014. Introduction to ground penetrating radar: Inverse scattering and data processing. John Wiley & Sons.

Pettinelli, E., G. Vannaroni, B. Di Pasquo, E. Mattei, A. Di Matteo, A. De Santis and P.A. Annan. 2007. Correlation between near-surface electromagnetic soil parameters and early-time GPR signals: An experimental study. Geophysics 72: A28.

Richards, R.A., G.J. Rebetzke, M. Watt, A.T. Condon, W. Spielmeyer and R. Dolferus. 2010. Breeding for improved water productivity in temperate cereals: Phenotyping, quantitative trait loci, markers and the selection environment. Functional Plant Biology 37:85-97.

Robinson, D.A., C. Gardner and J.D. Cooper. 1999a. Measurement of relative permittivity in sandy soils using TDR, capacitance and theta probes: Comparison, including the effects of bulk soil electrical conductivity. Journal of Hydrology 223:198-211.

Robinson, M., C. Bristow, J. McKinley and A. Ruffell. 2013. Ground penetrating radar. Handbook of Geophysical Techniques for Geomorphic and Environmental Research, Gilbert, B.Editor, Open File 3731:69-102.

Robinson, M., C. Bristow, J. McKinley and A. Ruffell. 1.5. 5. ground penetrating radar.

Saarenketo, T. 1998. Electrical properties of water in clay and silty soils. J. Appl. Geophys. 40:73-88.

Schmugge, T.J., T.J. Jackson and H.L. McKim. 1980. Survey of methods for soil moisture determination. Water Resour. Res. 16:961-979.

Schön, J.H. 2011. Chapter 8 - electrical properties. Handbook of Petroleum Exploration and Production 8:273-336.

Schultz, J.J. 2007. Using ground-penetrating radar to locate clandestine graves of homicide victims: Forming forensic archaeology partnerships with law enforcement. Homicide Stud. 11:15-29.

Sebastian, M.T. 2010. Dielectric materials for wireless communication. Elsevier.

Skjelvareid, M.H. 2012. Synthetic aperture ultrasound imaging with application to interior pipe inspection.

Skjelvaried, M.H., 2016, SYNAPTUS - a Matlab/Octave toolbox for synthetic aperture ultrasound imaging, https://github.com/mh-skjelvareid/synaptus

Smitha, N., D.U. Bharadwaj, S. Abilash, S.N. Sridhara and V. Singh. 2016. Kirchhoff and FK migration to focus ground penetrating radar images. International Journal of Geo-Engineering 7:4.

Stockmann, U., M.A. Adams, J.W. Crawford, D.J. Field, N. Henakaarchchi, M. Jenkins, B. Minasny, A.B. McBratney, De Courcelles, Vivien de Remy and K. Singh. 2013. The knowns, known unknowns and unknowns of sequestration of soil organic carbon. Agric. , Ecosyst. Environ. 164:80-99.

Stolt, R.H. 1978. Migration by Fourier transform. Geophysics 43:23-48.

Stone, J.F., D. Kirkham and A.A. Read. 1955. Soil moisture determination by a portable neutron scattering moisture meter 1. Soil Sci. Soc. Am. J. 19:419-423.

Tarnocai, C., J.G. Canadell, E. Schuur, P. Kuhry, G. Mazhitova and S. Zimov. 2009. Soil organic carbon pools in the northern circumpolar permafrost region. Global Biogeochem. Cycles 23.

Topp, C.N. and P.N. Benfey. 2012. 24 - growth control of root architecture. p. 373-386. *In* A. Altman and P.M. Hasegawa (eds.) Plant biotechnology and agriculture. Academic Press, San Diego.

Topp, G.C., J.L. Davis and A.P. Annan. 1980. Electromagnetic determination of soil water content: Measurements in coaxial transmission lines. Water Resour. Res. 16:574-582.

Tosti, F., C. Patriarca, E. Slob, A. Benedetto and S. Lambot. 2013. Clay content evaluation in soils through GPR signal processing. J. Appl. Geophys. 97:69-80.

Udphuay, S., T. Günther, M.E. Everett, R.R. Warden and J. Briaud. 2011. Three-dimensional resistivity tomography in extreme coastal terrain amidst dense cultural signals: Application to cliff stability assessment at the historic D-day site. Geophysical Journal International 185:201-220.

Wang, J.R. and T.J. Schmugge. 1980. An empirical model for the complex dielectric permittivity of soils as a function of water content. IEEE Trans. Geosci. Remote Sens.288-295.

Warren, C., A. Giannopoulos and I. Giannakis. 2016. gprMax: Open source software to simulate electromagnetic wave propagation for ground penetrating radar. Comput. Phys. Commun. 209:163-170.

Zhu, J., P.A. Ingram, P.N. Benfey and T. Elich. 2011. From lab to field, new approaches to phenotyping root system architecture. Curr. Opin. Plant Biol. 14:310-31. %